DISSERTATION

submitted to the

Combined Faculty of Natural Sciences and Mathematics

of Heidelberg University, Germany

for the degree of

Doctor of Natural Sciences

Put forward by

MSc. Philipp Linke

Born in Langenhagen, Germany

Oral examination: 11.11.2020

New stimuli-responsive substrates for the dynamic control of spatiotemporal patterns and fate of cells by physical cues

Referees: Prof. Motomu Tanaka

Priv-Doz. Dr. Falko Ziebert

Zusammenfassung

Biologische Zellen nehmen nicht nur biochemische, sondern auch physikalische Reize aus ihrer Mikroumgebung wahr. Zahlreiche Anhaltspunkte weisen darauf hin, dass Veränderungen der physikalischen Mikroumgebung von Zellen eine kritische Rolle in Prozessen wie Wachstum, Alterung und Erkrankung spielen. Bisher ist das Verständnis der dynamischen Reaktion von Zellen auf spontane Änderungen der physikalischen Mikroumgebung weitgehend unzureichend, da Substrate fehlen, welche klar definierte physikalische Signale erzeugen können. Der Hauptbestandteil dieser Arbeit beschäftigt sich mit der Entwicklung zweier Arten von Substraten, deren elastische und topographische Eigenschaften dynamisch verändert werden können, um die dynamische Reaktion der Zellen weit außerhalb eines physikalischen Gleichgewichts zu verstehen.

In Kapitel 4 wird das Design eines Substrats mit periodischen Falten von regulierbarer Wellenlänge vorgestellt, welches ermöglicht das Erscheinungsbild und die kollektive Orientierung von Mausmyoblasten zu kontrollieren. Dieses Substrat wurde durch die Ablagerung von hartem Polyimid auf weichem Polydimethylsiloxan unter axialer Stauchung hergestellt. Im Gegensatz zu allgemein üblichen Herangehensweisen zur statischen, topographischen Manipulation von Zellen (*statische Kontaktführung*), bietet das in dieser Studie vorgestellten Substrat die Möglichkeit, die Orientierung der Falten innerhalb von 60 Sekunden durch axiale Stauchung reversibel um 90° zu drehen. Des Weiteren wird in dieser Arbeit die *dynamische Kontaktführung* eingeführt, welche zur Untersuchung der Reaktion von Zellen auf spontane Änderung der Faltenausrichtung sowohl die Kinetik der Formanpassung und der kollektiven Orientierung der Zellen betrachtet, als auch die Existenz einer kritischen Wellenlänge nachweist, bei der die Neuanordnung der fokalen Adhäsionen und des Zytoskeletts stattfindet.

Kapitel 5 behandelt die Etablierung eines Hydrogel-Substrats, dessen Elastizität zur Regulierung von Erscheinungsbild, aktiver Kraftausübung und Differenzierung menschlicher mesenchymaler Stammzellen aus dem Knochenmark reversibel verändert werden kann. Einzigartig an dieser Studie ist die Verwendung eines Hydrogels mit reversiblen Wirt-Gast-Interaktionen, dessen Elastizität durch die Konzentration freier Wirt- oder Gastmoleküle gesteuert werden kann. Im Gegensatz zu häufig verwendeten chemisch vernetzten Hydrogelsubstraten mit fester Elastizität erlaubt dieses die Feineinstellung der Substratelastizität sowie deren spontane Änderung zu einem beliebigen Zeitpunkt. Die mechanische Kraft der Zelladhäsion wurde mit einem selbst entwickelten Messsystem bestimmt, das durch den Einsatz von laserinduzierten Schockwellen eine hohe Durchsatzrate erlaubt. Die so ermittelte Adhäsionsstärke und totale Energiedissipation durch zelluläre Traktionskräfte deuteten auf eine kritische Substratelastizität hin, welche das mechanosensorische System der Zelle aktiviert. Bemerkenswert ist, dass eine spontane Reduktion der Elastizität über diese Grenze zu einer sofortigen Verringerung der totalen Verzerrungsenergie führte. Des Weiteren führte der wiederholte Wechsel der Substratelastizität zu einer Reduktion der Proliferation, ohne die Multipotenz der Stammzellen zu beeinflussen.

Die dynamische Mikroumgebung für Zellen, welche in dieser Studie eingeführt wurde, ermöglicht neue Einblicke in die physikalischen Mechanismen von beispielsweise Zellentwicklung, Alterung und Erkrankung, welche die Plastizität des Lebens untermauern.

Summary

Biological cells sense not only biochemical cues but also physical cues from the surrounding microenvironment, and adapt their function and fate. Ample evidence suggests that changes in physical microenvironments of cells play critical roles in development, aging and diseases. However, the understanding of the dynamic response of cells to abrupt changes in physical microenvironments is still incomplete due to a lack of substrates that can provide well defined physical commands. The main thrust of this thesis is the design of two new types of substrates, which dynamically change elasticity or topography in order to unravel dynamic cellular response far out of equilibrium.

Chapter 4 presents the design of substrates with periodic wrinkles of adjustable wavelength for the switching of morphology and orientational order of mouse myoblasts. The substrates used in this study were fabricated by the deposition of hard polyimide on soft polydimethylsiloxane under axial strain. In stark contrast to commonly used approaches in topographic control of cells under static conditions (*static contact guidance*), the wrinkled substrates designed in this study are able to reversibly switch the wrinkle direction by 90° within 60 s simply by axial compression and relaxation. *Dynamic contact guidance* introduced in this study unraveled the kinetics of shape adaptation and orientational orders of cells as well as the existence of a critical wavelength for rearrangement of the focal adhesions and remodeling of cytoskeletons in response to the abrupt change in wrinkle direction.

Chapter 5 deals with the establishment of hydrogel substrates that can reversibly change the bulk elastic modulus for regulation of the morphology, active force generation and the fate decision of human mesenchymal stem cells derived from the bone marrow. The uniqueness of this study is to use hydrogels with reversible host-guest interactions, whose elasticity can be adjusted by the concentration of free host or guest molecules. In contrast to commonly used, chemically crosslinked hydrogel substrates with fixed elastic moduli, this enables to fine-adjust the substrate elasticity as well as to abruptly switch the substrate elasticity at any given time point. The mechanical strength of cell adhesion determined from a self-developed, high-throughput assay utilizing shock waves as well as the total energy dissipation by cellular traction forces indicated the presence of a critical substrate elasticity which triggers the mechanosensory system. Remarkably, an abrupt softening of substrate stiffness across this threshold instantaneously led to a decreasing total strain energy. Furthermore, frequent exchange of the substrate elasticity resulted in decreased proliferation without interfering with the multipotency of stem cells.

The dynamic cellular microenvironments established in this study open the new possibility to gain insight into the physical mechanism underpinning the plasticity of life, such as development, aging, and diseases.

Acknowledgements

I would like to thank

Prof. Dr. Motomu Tanaka for the great support and guidance throughout my PhD and deep scientific discussions. I am especially grateful for the chance to spend an extended time in Kyoto to broaden my scientific horizon,

Priv.-Doz. Dr. Falko Ziebert for kindly acting as a second referee in this thesis and my disputation,

Prof. Dr. Akira Harada and **Dr. Masaki Nakahata** for sharing their knowledge on supramolecular complexes and self-healing materials, which made this thesis possible,

Dr. Takuya Ohzono for teaching me on-site and expanding my scientific background regarding stimuli-responsive materials,

Prof. Dr. Anthony D. Ho, Prof. Dr. Carsten Müller-Tidow and **Priv.-Doz. Dr. med. Sascha Dietrich** for kindly providing stem cell samples from human donors and providing support with their experience and expertise,

Prof. Martin Bastmeyer and **Dr. Marc Hippler** for the fruitful collaboration with the Karlsruhe Institute of Technology (KIT),

The German Science Foundation (SFB 873 B07) for supporting my research financially and creating the framework for a stem cell research community,

The Cluster of Excellence 3DMM2O and HeKKSaGOn for creating interdisciplinary networks sparking novel research collaborations,

Dr. Akihisa Yamamoto and **Dr. Ryo Suzuki** for sharing their ample knowledge and discussing my experiment planning and scientific results in great detail,

Dr. Viktoria Frank for the introduction and advice at the beginning of my PhD,

Dr. Wasim Abuillan for inspiring scientific discussions during coffee breaks,

Dr. Stefan Kaufmann for countless lessons in cell biology and Bavarian culture,

Julian Czajor for recreational activities and being a very good friend,

Dr. Federico Amadei for culinary arts and being a great skiing companion,

Dr. Sven Mehlhose, Dr. Benjamin Fröhlich, Esther Kimmle, Judith Thoma for random encounters, excursions in musicality and being exceptionally great people,

Dr. Salomé Mielke, Dr. Theresa Bentele, Dr. Kentaro Hayashi, Dr. Maryam Eshrati, Dr. Mariam Veschgini, Bahareh Ibrahimi, Felix Weissenfels, Natalie Munding und **Danny Egic** for the enjoyable time in science and beyond,

Gabriele Fabry and **Mieko Yoshida** for the highly reliable organization and administration in Heidelberg and Kyoto,

and all other current and former **members of AK Tanaka in Heidelberg and Kyoto** for your continuous support, happy memories and friendly atmosphere.

Finally, I would like to thank my family for their continuous spiritual support.

身を浅く思い、世を深く思う。

Think lightly of yourself and deeply of the world.

Miyamoto Musashi 1584 – 1645

Contents

1 Introduction

Biological cells receive a variety of stimuli from their microenvironment, including biochemical and physical cues. During the past two decades, physical interactions between cells and their environment have been drawing increasing attentions, and "mechanobiology" is an emerging new discipline connecting biologists, engineers, material scientists, and physicists.[1,2] Mounting evidence has suggested that physical cues trigger or regulate a large range of cell functions such as migration,[3,4] proliferation,[5,6] adhesion,[4,7] orientation,[8,9] differentiation[6,10] and apoptosis.[11,12] In order to "feel" the environment, integrin receptors bind to the extracellular matrix (ECM) and serve as *mechanosensors*. They activate signaling molecules[13,14] and adhesion domains (focal adhesions) which crosslink the ECM and cytoskeletons inside of the cell. Once mechanosensing machineries are activated, cells actively generate traction forces by molecular motors and adapt their shape, motion, and functions.[15]

Mechanical interactions between cells and the extracellular matrix do not only influence single cells but also determine the functionality of tissues. Within a tissue, cells are able to migrate and change their shape and orientation to sustain their structural and functional integrity in a robust manner.[19] Here, the establishment of orientational order is one of the prerequisites for connecting single-cellular functions and tissue functions. For example, smooth muscle cells in heart muscle tissue are aligned in the direction parallel to collagen fibers (Figure 1.1a). In the 1940s, Weiss and co-workers reported the response of cell functions to a topographical environment.[17] As shown in Figure 1.1b, they scratched geometric shapes into the surface of mica and plated spinal ganglia at the intersections of scratches. After a few days, the initial cell clusters grew preferably into the direction of the scratches,

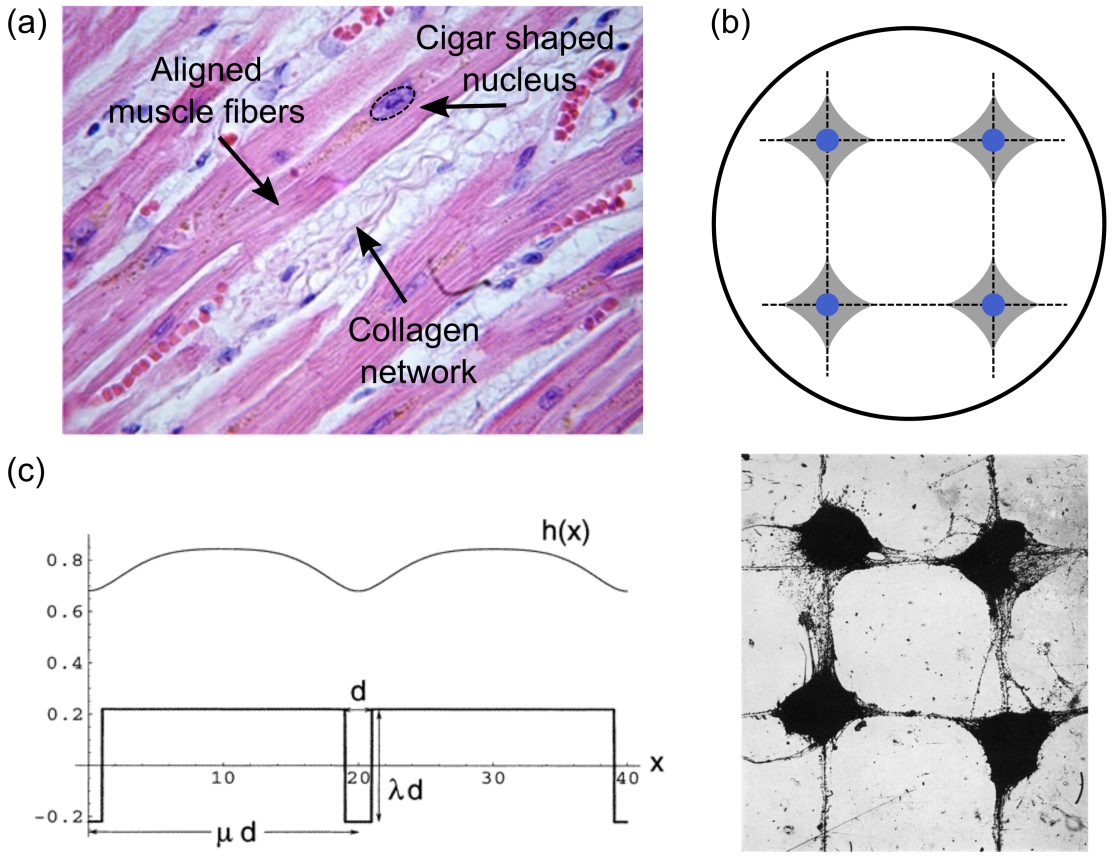

Figure 1.1: Examples of contact guidance. (a) Hematoxylin and Eosin staining of histological smooth muscle sample. Cells are guided by the collagen fibers and elongate in the same direction as the fibers.[16] (b) Upper image: Scheme of grooved mica structure. The dashed lines indicate scratches in the surface. Blue areas represent the explanted ganglia and the gray areas are newly formed tissue after several days of cultivation. (Adapted from P. Weiss).[17] (c) Mathematical model of membrane adhesion. The profile of a membrane $h(x)$ is supported above a periodically structured substrate with ridges. Due to the effects of rigidity and tension, the membrane shape follows the substrate profile with a much reduced amplitude. (Adapted from Swain *et al.*)[18]

demonstrating the principle of *contact guidance*. Afterwards, contact guidance has been reported as a universal principle guiding many cell types, including fibroblasts, myoblasts, neuroblasts, dendrocytes, and endothelial cells.[8,20–22] For example, myoblasts develop into muscle tissue, where the cell alignment is essential to optimize their contractile functions and stability.[23] Seeding muscle cells on ridges with sub-micrometer features significantly enhanced the expression of dystrophin, a muscle-connecting protein, and the myogenesis of cardiac cell patches from mice, compared to flat substrates.[24] Recently, a mechanosensitive Ca^{2+} ion channel was identified, called PIEZO1, which controls the aligned fusion of myoblasts into myotubes. PIEZO1 knock-out cells lack the ability to form myotubes and instead fuse uncontrollably into large, isotropic syncytia.[25]

From the viewpoint of physics, the interaction of cells with topographic patterns can be treated as a subtle problem of wetting.[26] Different from simple Newtonian fluids,[27] viscoelastic cells deform both plastically and elastically. Antelmann *et al.* analytically calculated the deformation of membranes in response to a variety of geometries, such as a rectangular ridge (Figure 1.1.c).[18] To date, the principle of contact guidance has been studied by using a variety of topographically structured substrates. Most studies rely either on a topography with periodic ridges and grooves, which are created by lithography[20,28] or on wrinkle patterns with no singularity. The latter can be fabricated by the deposition of a stiff layer such as metal,[29,30] hard plastic,[31] or graphene[32] on top of soft polymers such as polydimethylsiloxane (PDMS). More recently, a so-called *direct laser writing* method is used to make such topographic patterns.[33]

Despite of the accumulating understanding of contact guidance, most studies have been limited to look at the cell response under static environments. However, the microenvironment of biological cells and tissue is permanently evolving and hence never uniform or static.[34,35] The lack of understanding how cells follow the guidance of topography in a dynamic environment has sparked a search for substrates with switchable topography on-demand. Previously, substrates which switch from flat to wrinkled topography were created by thin polyelectrolyte mul-

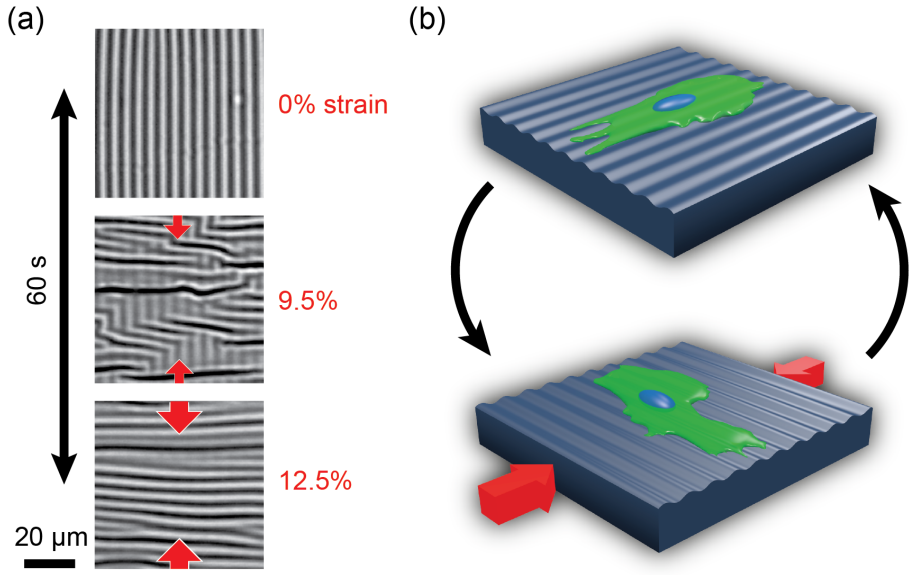

Figure 1.2: (a) Phase contrast images of the wrinkle pattern at different levels of axial strain indicated by red arrows. The process of wrinkle realignment is achieved within 60 s. (b) Scheme of cell alignment on the wrinkle substrates. The cytosol of the cell is sketched in green and the nucleus in blue. Reversible realignment of the cell to the wrinkle direction was shown in this thesis.

tilayer coating on shape-memory material. Upon heating to physiological temperature, wrinkles were formed with a wavelength of half a micrometer. Cardiomyocytes derived from human induced pluripotent stem cells exhibited a distinct alignment on the wrinkles compared to the flat substrate.[36] Several other studies have also reported the writing or erasing of wrinkles by thermal[36,37] or optical cues[21], but these substrates irreversibly write or erase their topography only once. Lam *et al.* reported a reversible writing/erasing of cells on a plasma oxidized PDMS substrate.[38] However, since the writing/erasing of wrinkles always returns to the flat substrate, it can only activate or deactivate contact guidance. So far the complete rearrangement of the topography, for example by changing the angle of the surface pattern, has proved to be elusive.

In Chapter 4 a new strategy for dynamic contact guidance of cells is presented. Specifically, a substrate with wrinkled topography was designed in collaboration with Dr. T. Ohzono of the National Institute of Advanced Industrial Science and Technology (AIST, Japan). The substrate was fabricated from PDMS which was

coated with polyimide[31] and cured under strain to create periodic wrinkles with micrometer-scale wavelength. The main advantage of these materials over the previous approaches is not only the ability to "write/erase" wrinkles but also to switch the wrinkle direction by 90° by applying an axial strain.[30,39] In the first step, the preparation and surface functionalization were systematically optimized to control the adhesion, morphology, and orientational order of mouse myoblast cells. Figure 1.2a presents the switching of wrinkle directions by axial strain. Section 4.2f reveals how the cells adapt their morphology and orientational orders, which is considered in this study as *static contact guidance*. In order to analyze the alignment of cells and the actin cytoskeleton, the *nematic order parameter*[40,41] was introduced by approximating cells as ellipses. Furthermore, the localization of focal adhesions is analyzed with respect to the peaks and troughs of the wrinkle topography. This strategy was further extended to investigate dynamic contact guidance (Section 4.4f). The dynamic response of C2C12 cells before and after the change of wrinkle direction by 90° was monitored by live cell imaging. First, the aspect ratio and cell angle are analyzed to characterize the orchestration of cell morphology and the actin cytoskeleton. Additionally, the transfection with LifeAct-GFP[42] further enabled the *in situ* imaging of the transitions of their nematic order.

Since cells detect the elasticity of their environment and control functions and fate, another strategy for the dynamic control of cells is to change the substrate elasticity. Depending on the elasticity of ECM and neighboring cells, they adjust the active traction force powered by the actin-myosin network.[45] In 1980s, Harris *et al.* reported that the active traction force generated by chicken heart fibroblasts created wrinkles of silicon rubber (Figure 1.3a).[43] As shown in Figure 1.3b, traction forces can be visualized by embedded beads or micropatterning of ligand molecules, called *traction force microscopy*. As many studies demonstrated that cellular functions are optimized on substrates that possess a similar elasticity to the elasticity of extracellular matrix (ECM),[46–49] substrates with corresponding elasticity have been developed. During the past 20 years, a number of synthetic

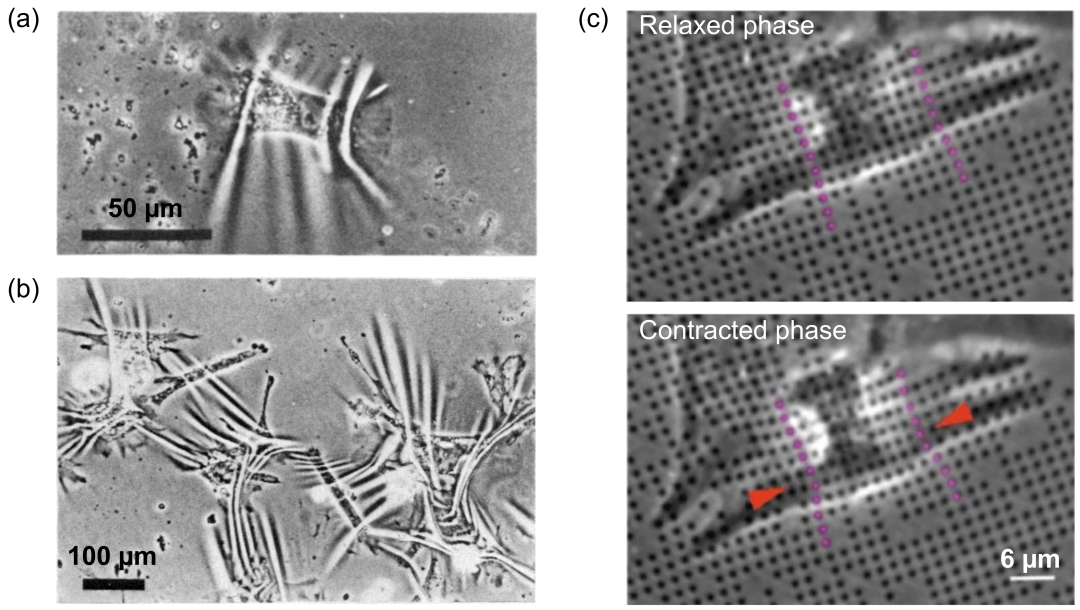

Figure 1.3: Examples of force generation in cells. (a) A chick heart fibroblast pulls on a thin sheet of silicone rubber, resulting in wrinkling of the substrate.[43] (b) Lower magnification image of ca. twelve chick heart fibroblasts. The cell traction generates a complex pattern of distortion in the rubber sheet. (Adapted from Harris *et al.*)[43] (c) Phase contrast image of a cardiac myocyte plated on a compliant substrate ($E = 19\,\mathrm{kPa}$) with an embedded pattern of dots. The upper image shows the relaxed phase and the lower image the contracted phase. Magenta colored dots highlight the displacement during contraction in direction of the red arrows. (Adapted from Balaban *et al.*)[44]

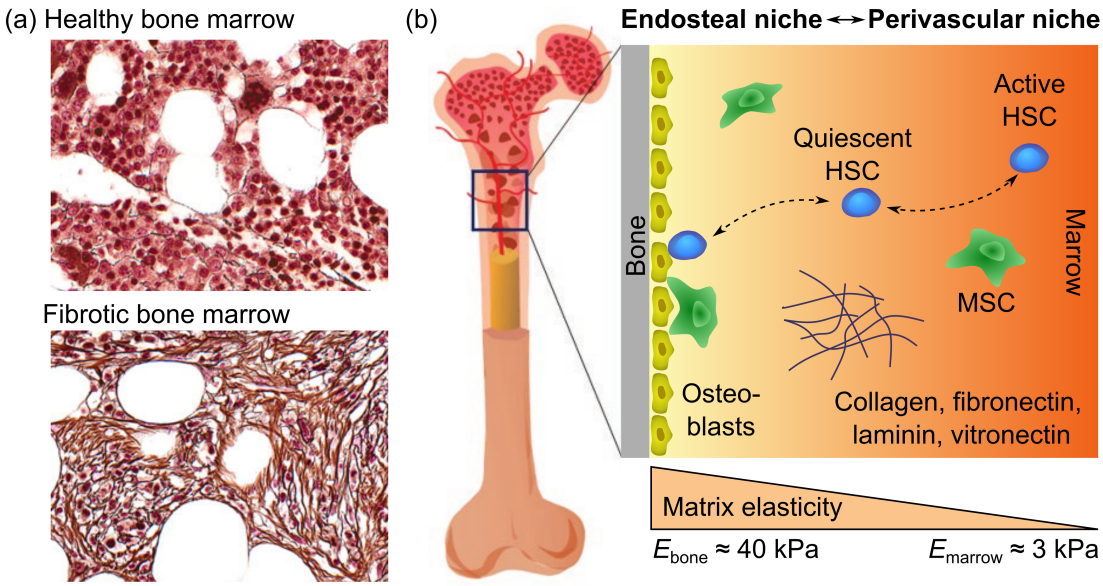

Figure 1.4: (a) Histology samples from healthy (above) and fibrotic (below) bone marrow, stained by Gomori's staining.[53] Healthy tissue shows no intersections while the diseased tissue contains coarse bundles of thick fibers, leading to an increase in elastic modulus by roughly an order of magnitude.[54] (b) The bone marrow niche consists of multiple cells of hematopoietic and mesenchymal lineages. This unique environment is governed by a large range of elasticity from 40 kPa close to the bone region to 3 kPa in the bone marrow.[55] Mesenchymal stem cells (MSC) are self-renewing and maintain the bone marrow niche by differentiation into various lineages that are native to the environment. Additionally, they play an important role in the activation and self-renewal of hematopoietic stem cells (HSC).[56] (Adapted from Choi *et al.*)[46]

and natural polymers have been tested as substrate materials, such as hyaloronic acid,[50] polyacrylamide,[4] PDMS[51] and collagen.[52] Nevertheless, it should be noted that the majority of ECM models based on polymers are chemically crosslinked by covalent bonds, which can merely offer prefixed elastic conditions to cells.

In is notable that mechanical properties of ECM in biological systems are never static or homogeneous. In fact, abnormal ECM elastcity is often accompanied with severe diseases. For example, hematological diseases like acute myeloid leukemia are characterized by fibrosis in the bone marrow, resulting in ECM stiffening.[57] As a result, the hematopoietic system is strongly impaired, followed by reduced production of red blood cells, called *cytopenia*.[58] Examples of healthy and fibrotic bone marrow samples are shown in Figure 1.4a, highlighting the importance of elas-

ticity in the context of disease research. Human mesenchymal stem cells (hMSC) are a multipotent, somatic stem cell type that is able to differentiate into neurons, muscles and bones. In the bone marrow (Figure 1.4b), hMSCs play instrumental roles in the maintenance of hematopoiesis by harnessing hematopoietic stem cells (HSC).[59,60]

In this thesis, hydrogel substrates that possess comparable elasticity to bone marrow ECM have been developed in order to dynamically regulate the morphology, active force generation and the fate decision of hMSCs. As the elasticity of bone marrow ECM is between 3 kPa and 40 kPa (Figure 1.4a), a substrate that can switch the elasticity within this range was designed. In contrast to widely used hydrogels that can change the elasticity only once and in an *ireversible* manner,[24,61–67] a new class of hydrogels was developed in this study which are crosslinked by *reversible*, supramolecular interactions in collaboration with Dr. Masaki Nakahata and Prof. Akira Harada of the Department of Macromolecular Science, Osaka University (Japan). As schematically shown in Fiure 1.5, hydrogels are crosslinked by host-guest interactions between beta-cyclodextrin (βCD) and adamantane (Ad). One of the unique characteristics of supramolecular hydrogels is that host-guest pairs can be reversibly dissociated/associated by adding/removing competitive host (or guest) molecules to/from the solution.

Section 5.1 presents how hMSCs adapt their morphology and nematic order of actin under static conditions (*static mechanosensing*). As presented in Section 5.2, the strength of cell adhesion was measured using a pressure wave induced by a picosecond laser pulse, yielding the critical pressure for cell detachment. Since the adhesion force of cells is known to influence active force generation in cells, in Section 2.4.4 the strain energy and net contractile moment were calculated by means of *traction force microscopy*. Expanding on this strategy, the response of hMSCs to an abrupt change in substrate elasticity was measured, which is considered *dynamic mechanosensing*. For this purpose, *in situ* traction force microscopy experiments were performed with living cells (Section 5.4). Force-related as well as morphological parameters were extracted and correlated with the morphologi-

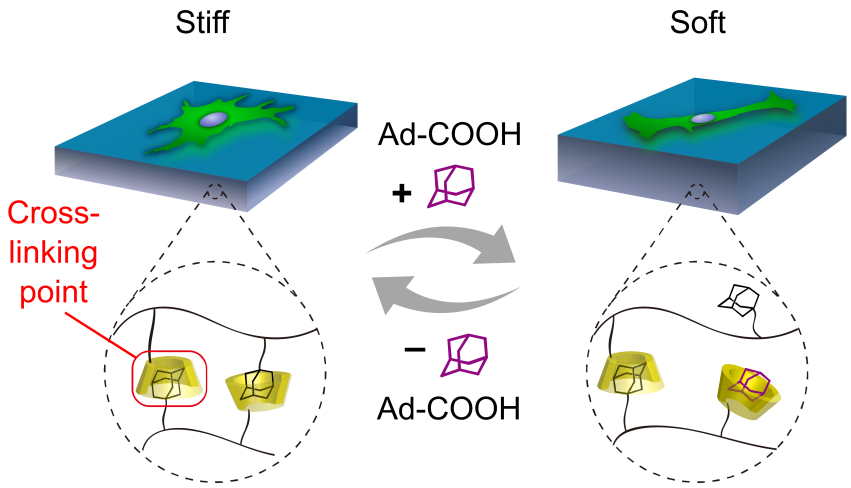

Figure 1.5: Schematic overview of the host-guest hydrogel. Cells (green) are seeded on top of the gel (blue). By adding adamantane-carboxylic acid (Ad-COOH) the gel becomes softer and cells respond, for example, by changing the morphology. Below, the chemical composition of the gel is illustrated, showing the host beta-cyclodextrin (yellow cone) and the guest molecule adamantane (black diamond).

cal dynamics. Finally, in Section 5.5, the influence of the frequency of mechanical stimuli on the fate of hMSCs was investigated. hMSCs were exposed to cyclic changes in elasticity over 20 days. The influence of substrate elasticity under static conditions as well as the influence of stress frequency was evaluated by the maintenance of multipotency and the change in self-renewal (proliferation). The former was estimated by the expression level of the multipotency marker STRO-1,[68,69] while the latter was determined by the change in cell density. The obtained results shed light on the suitability of the stimuli-responsive hydrogel as stem cell niche model and demonstrate the control of stem cell functions and morphology by dynamic mechanical cues.

2 Theoretical background

2.1 Cell mechanics

In order to form biological organisms, cells have to provide a range of physical functions ranging from simple structural integrity to complex neuronal signaling.[70] Many of these functions involve physical properties such as elasticity, bending rigidity, and force generation.[13] Therefore, this section will focus on the basic physical principles which are relevant in the field of cell mechanics.

2.1.1 Cell adhesion

Cells form physical links with their microenvironment by adhesion domains, so called *focal adhesions*. These protein complexes are mechanical links between actin bundles and the extracellular matrix and facilitate various cell functions such as migration, proliferation and differentiation.[4,5,10] The key component is the transmembrane protein *integrin* which interacts with a variety of proteins to enhance stability but also processes the mechanical stimuli that the cell receives from the outside.[13,14] As a response, the mechanosensing machinery is activated and the cell actively exerts forces on the extracellular matrix (ECM).

As shown in Figure 2.1a, focal complexes (red lines) are formed at the cell edge (*lamellipodium*) and mature over time into focal adhesions (red clouds). Internally, focal adhesions are connected to stress fibers of the actin network (blue) and externally to the ECM via ligands, e.g. fibronectin (green squares). Figure 2.1b shows a more detailed view of the focal adhesion, including some prominent examples from the pool of more than 150 proteins involved in the focal adhesion

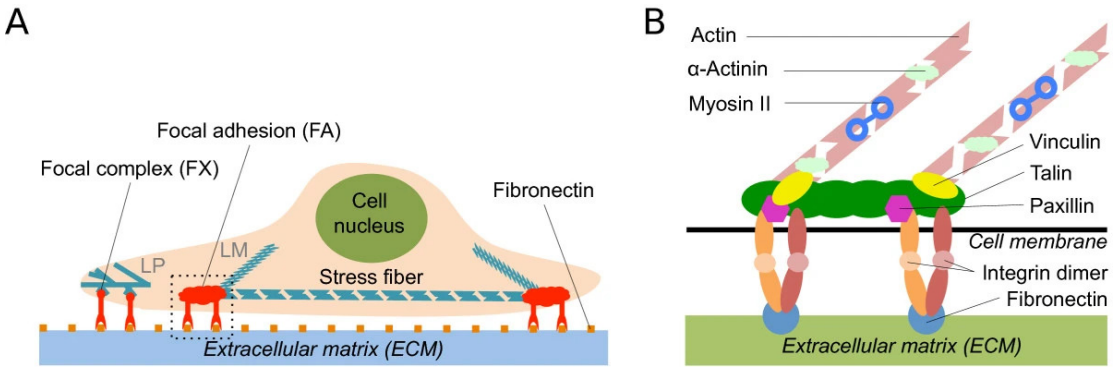

Figure 2.1: Scheme of the focal adhesion. (a) Focal complexes (red lines) are formed in the lamellipodium and mature into focal adhesions (red cloud). These are usually connected to stress fibers of the actin network (blue). Outside of the cell, focal adhesions are connected to the extracellular matrix (ECM) via ligands, e.g. fibronectin (green squares). (b) Detailed view of the focal adhesion. Some prominent proteins included in the focal adhesion are shown. A focus is put on integrin (red/orange) as the only transmembrane protein in this complex. Adapted from Lu *et al.*[71]

complexes,[72] like vinculin (yellow), talin (green) and paxillin (magenta).

Physically, cell adhesion can be understood as a double-well intermembrane potential.[73] Short-ranged attractive forces and medium range repellent forces, as well as elastic stress due to deformation of the cell membrane, lead to the formation of an adhesion area A. This mechanism depends on the type of ligand-receptor pair and intrinsic cell properties like cell tension and elasticity.[73–75] Assuming the cell membrane as a lipid bilayer on a flat surface with the distance to the surface $h(x)$ (*membrane contour*), the total free energy of cell adhesion G can be expressed as follows:[76]

$$G = \int \left[\frac{\kappa}{2}(\nabla^2 h(x))^2 + \frac{\sigma}{2}(\nabla h(x))^2 + V(h(x))\right] d^2x. \tag{2.1}$$

The individual terms can be understood as follows: The first term refers to the Helfrich repulsion,[77] which considers thermal fluctuation and bending undulation with the bending modulus $\kappa \approx 25\ k_B T$. During adhesion, the cell membrane is immobilized, which is entropically unfavorable, so that the membrane forms undulations that increase with thermal energy and form a steric repulsion against

cell adhesion. The steric potential is defined as follows:[76]

$$V_{ster}(h(x)) = \frac{(k_bT)^2}{\kappa h^2}. \tag{2.2}$$

The second term considers the membrane tension σ and depends on the first derivative of the membrane contour.

Finally, the last term describes the intermembrane potential which includes short-range steric repulsion, van der Waals interactions and repeller-induced repulsion:

$$V(h(x)) \approx V_{sr}(h(x)) + V_{vdW}(h(x)) + V_{rep}(h(x)). \tag{2.3}$$

The short-ranged steric repulsion (V_{sr}) has a decay length of $\lambda \approx 1\,\mathrm{nm}$ and a base potential of $V_0 < 30\,\mathrm{mJ/m^2}$. It was empirically determined as:[73]

$$V_{sr}(h(x)) = V_0\, e^{-h/\lambda}. \tag{2.4}$$

Van der Waals (vdW) interactions occur between dipoles, such as water molecules, and are described by the following equation:

$$V_{vdW}(h(x)) = -\frac{H_A}{12\pi}\left(\frac{1}{(h+2\delta)^2} + \frac{1}{h^2} - \frac{1}{(h+\delta)^2}\right), \tag{2.5}$$

with the Hamacker constant $H_A \approx 10^{-21}\,\mathrm{J}$ and the bilayer thickness δ. Additionally, inter-membrane repulsion is induced by extracellular proteins. The potential of repellers is proportional to their lateral density σ_0 and takes two different forms, depending on the relation between the radius of gyration R_{gyr} and the membrane-surface distance h:

$$V_{rep}(h(x)) \approx \begin{cases} \frac{\pi}{6} k_bT\sigma_0 \left(\frac{R_g}{h(x)}\right)^2 e^{-1.5(h/R_g)^2},\ h \gg R_g, \\ k_bT\sigma_0,\ h \ll R_g. \end{cases} \tag{2.6}$$

The superposition of these three potentials has a primary minimum around 35 nm,

which can be approximated by a harmonic potential as follows:[76]

$$V(h(x)) \approx V_0 + \frac{1}{2}\gamma(h - h_0)^2, \tag{2.7}$$

where the parameter γ refers to the membrane curvature and h_0 to the equilibrium position of the membrane.[73,78]

2.1.2 Active force generation in cells

The shape of cells is determined by a diverse network of polymers and helper proteins, called the *cytoskelton*. The following three polymers are most essential for the integrity of the cytoskeleton: actin-filaments, microtubuli and intermediate filaments. This thesis will focus on actin-filaments, since they are the most abundant filaments and crucial in defining the cell shape.

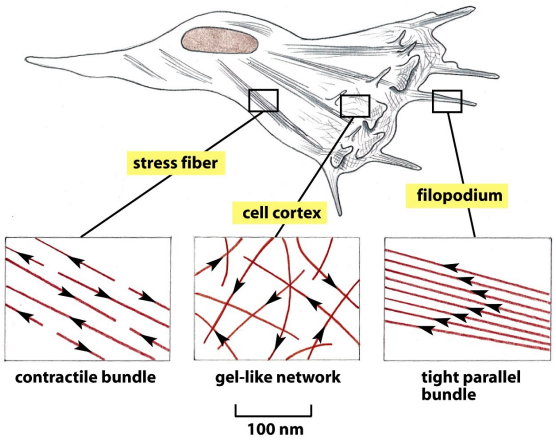

Figure 2.2: Scheme of the actin cytoskeleton during cell locomotion.[79] Red lines in enlarged images represent actin filaments and black arrows indicate the direction of the pointed end. Stress fibers generate tension, cell cortex enhances membrane stability and filopodia allow the cell to probe its environment.

During actin polymerization, filaments (*F-actin*) are assembled from actin monomers (*globular actin, G-actin*). In its filamentous form, actin takes a helical shape with two parallel strings twisted around each other. This polymer possesses a fast growing end, called *barbed end*, and a slow growing end, called *pointed end*.

The association constant of new monomers is ca. six times larger on the barbed

end, resulting in a dynamic growth which is limited by the concentration of G-actin:

$$\frac{dN}{dt} = (k_{on}^{+} + k_{on}^{-})\, c_A - (k_{off}^{+} + k_{off}^{-})\ . \tag{2.8}$$

Here, N is the number of monomers in the filament and c_A is the concentration of free G-actin. As the polymer grows, its length will reach an equilibrium state at

$$c_A^{*} = \frac{k_{off}^{+} + k_{off}^{-}}{k_{on}^{+} + k_{on}^{-}}, \tag{2.9}$$

where the growth rates on the barbed and pointed end are identical. This equilibrium state is commonly described as *threadmilling*.

The arrangement of actin filaments to networks is responsible for a range of morphological features in cells. Figure 2.2 shows three major appearances of actin networks in the magnified sections. The red lines represent actin filaments with black arrows indicating the direction of the pointed end, i.e. the direction of polymerization. Spanning the whole cell body, *stress fibers* generate contractile forces along their orientation. They consist of parallel actin filaments with two directions of polymerization. Below the cell membrane exists a layer of dense filament networks, the *cell cortex*. Here, actin filaments are randomly oriented to form a gel-like network. The main function of the cortical actin is to stabilize the cell membrane. Pointing outward, actin bundles form *filopodia* which enable the cell to probe its environment. Here, the orientation of all actin filaments is identical to maximize the growth speed of filopodia.

2.1.3 Polymer networks and gels

Gels are ubiquitously represented in biological tissues. From intracellular actin- to extracellular collagen-networks, proteins form gels to enhance stability and fine-tune elastic properties of tissues. Physically, the elasticity of a gel is determined by the following quantities:[1]

- the mean mesh size ξ,
- the total number of crosslinks M_c (with length L_c) between nodes which consist of N_c Monomers,
- the density ν_c of connections between nodes with $\nu_c = M_c/V$,
- the concentration of *dangling bonds*, i.e. free polymer ends.

In Figure 2.3 a scheme of the gel structure is shown. The polymers are depicted in black with red dots indicating the nodes. The elasticity of a gel is commonly measured by the shear modulus, which is defined as shear stress devided by shear strain. Accorting to Hill,[80] the shear modulus of gels can be described as follows:

$$G_0' = gM_c \cdot k_BT = g\frac{c}{N_c} \cdot k_BT = g\frac{k_BT}{\xi^3}, \tag{2.10}$$

with the monomer concentration c and a topology dependent factor $g \approx 1$. This

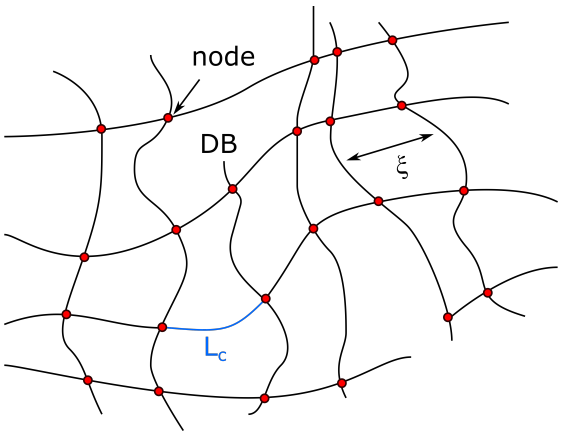

Figure 2.3: Scheme of gel structure. Network of polymers (black lines) connected by nodes (red dots), structure defined by contour length L_c and mesh size ξ. Elastic properties are further influenced by the number of dangling bonds (DB).

means that the shear modulus is proportional to the number of crosslinks M_c or, alternatively, inverse proportional to the volume of a unit cell ξ^3 with the mesh size as edge length. G' can be measured by rotational rheometry, where the gel is sheared by rotation and the applied force as well as the degree of rotation is monitored. An alternative parameter of elasticity is the Young's modulus which will be explained in Section 2.4.1.

2.1.4 Membrane deformations

When observing mechanical effects on cells, membrane deformation cannot be avoided. The essential question in this matter is how the energy of deformation depends on the cell shape. To quantify membrane deformation, four major effects have to be differentiated as shown in Figure 2.4: stretching, bending, thickness change, and shear.[81] Stretching of a membrane is simply a change in the area $\Delta a(x, y)$ with respect to a reference area a_0. Therefore, the free energy $G_{stretch}$ can be calculated as follows:[82]

$$G_{stretch} = \frac{K_a}{2} \int \left(\frac{\Delta a}{a_0} \right)^2 da. \tag{2.11}$$

This takes into account that the area stretch depends on the position. If the area change is constant, the integration can be omitted. The parameter K_a is the area-stretch modulus which lies in the range of $50 - 500\,\mathrm{mN/m}$ for lipid bilayers.[83] Bending of cell membranes is more complex and usually described by a simple height profile $h(x_1, x_2)$. Note that this approach fails, if the membrane forms a cavity or an overlap, which would require more complex approaches. The bending κ_{ij} of the membrane is then defined as the second derivative of $h(x_1, x_2)$:

$$\kappa_{ij} = \frac{\delta^2 h}{\delta x_i \delta x_j}, \tag{2.12}$$

so that the height profile h can be written as the sum of the individual curvatures:

$$h(x_1, x_2) = \sum_{i,j=1}^{2} \kappa_{ij} x_i x_j. \tag{2.13}$$

With this expression the free energy of bending can be described by the Helfrich-Canham-Evans model:[84–86]

$$G_{bend}[h(x, y)] = \frac{K_b}{2} \int [\kappa_1(x, y) + \kappa_2(x, y)]^2 \, da, \tag{2.14}$$

where κ_1 and κ_2 are the principal curvatures of the surface at the point of interest and are obtained by diagonalization of the matrix κ_{ij}. The typical range for the bending rigidity K_b is $0.5 - 1 \times 10^{-19}$ J for lipid membranes[87] and $1 - 10 \times 10^{-19}$ J for biological cells.[88]

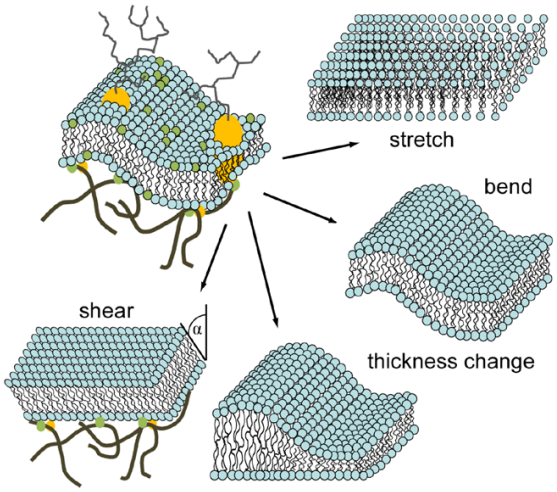

Figure 2.4: The geometry of membrane deformations. The four major deformations are: membrane area stretching, bending, membrane thickness change and shearing. (Adapted from Monzel *et al.*)[81]

The thickness of membrane can be altered locally by hydrophobic parts of membrane proteins. The parameter $w(x, y)$ is usually described as the half thickness of a bilayer and results in an energy penalty when deviating from the equilibrium thickness $2w_0$. The free energy of thickness change is defined as:[82]

$$G_{thickness}[w(x,y)] = \frac{K_t}{2} \int \left[\frac{w(x,y) - w_0}{w_0} \right]^2 da, \tag{2.15}$$

with the area compressibility K_t which is typically around 300 mN/m.[89,90] Finally, the shearing of membranes is also subjected to an energy penalty. However, it rarely occurs in biological membranes and is thus not further explained.

2.2 Cell biology

The response of cells to physical cues strongly depends on the cell type. Some cell functions are specific to certain types such as differentiation in stem cells,[91]

while other functions are more pronounced in other types, such as active force generation in muscle cells.[92] Since this study focuses on two different stimuli-responsive substrates, two different cell types were applied whose functions are especially suited for each substrate. This section will introduce the two cell types and highlight their biological background.

2.2.1 Mouse myoblast cells

C2C12 cells are a type of myoblast cells which were originally isolated by Yaffe and Saxel.[93] They are derived from C3H mouse leg muscle and exhibit rapid proliferation and differentiation capabilities, providing a popular model system for cell cycle and muscle development studies.[94]

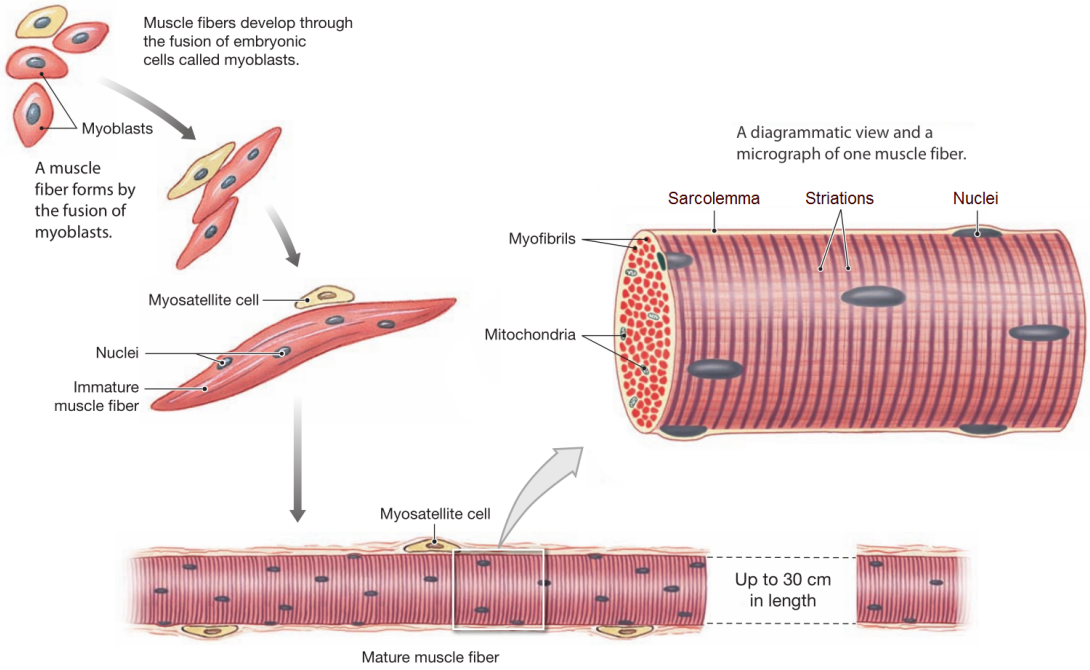

Figure 2.5: Principle of myotube formation. Several myoblasts fuse into multinucleated cells, so-called *myotubes*. Satellite cells reside at the periphery and provide regenerative capabilities in the case of injury. The mature fiber is surrounded by the sarcolemma, a specified cell membrane with nuclei directly below. The center of the fiber is made of myofibrils and mitochondria. (Adapted from Martini *et al.*)[95]

In order to create functional muscle fibers, myoblasts develop into multinucleated structures, so called *myotubes* (Figure 2.5), by cell fusion, which is initiated

in vitro under low serum conditions or starvation.[94] The fusion of cells is a highly complex mechanism, relying on cell-cell adhesion and vesicle trafficking. The vesicles are able to fuse with the cell membrane and, on this way, initiate pore formation and fusion with neighboring cells.[96] Readily fused myotubes can be identified by increased expression of myosin heavy chain,[97] as well as a dense actin wall structure which facilitates further elongation of the plasma membrane.[98]

2.2.2 Mesenchymal stem cells

Stem cells are famous in regenerative medicine for their ability to develop into any type of cell by differentiation. This ability allows applications from tissue regeneration to organogenesis by transplantation or injection of multipotent stem cells.[99,100] Embryos consist predominantly of stem cells, which differentiate with the development of organs and tissues.[101] The more a stem cell specifies into a certain lineage, the more differentiation potential is lost, and since differentiation is irreversible, this leads to relatively low stem cell numbers in adult humans and animals.[95] These adult stem cells usually reside in the so called *stem cell niche* in a quiescent state and are activated during diseases or injuries to repair damaged tissues.

Human mesenchymal stem cells (hMSC) have first been identified by Friedenstein[103] and exist most abundantly in the bone marrow, peripheral blood, adipose tissue, umbilical cord, and cord blood.[91,104] The major differentiation capabilities of hMSCs are fat, cartilage, bone, and connective stromal cells which are all members of the mesoderm lineage (Figure 2.6). Other differentiations into the ectoderm and endoderm lineage have been performed *in vitro* but were not yet confirmed to also occur *in vivo*. Harvesting of hMSCs is performed by bone marrow aspiration and seeding on plastic culture vessels followed by elimination of non-adherent cells.[105] Several antibodies were confirmed to be common among all hMSC cultures, most commonly including CD105, CD45, CD90, HLA class II, CD14, and CD34.[106] A relatively new mesenchymal stem cell marker was discovered, called STRO-1,[68,69,107] which is present in bone-marrow derived hMSCs, but

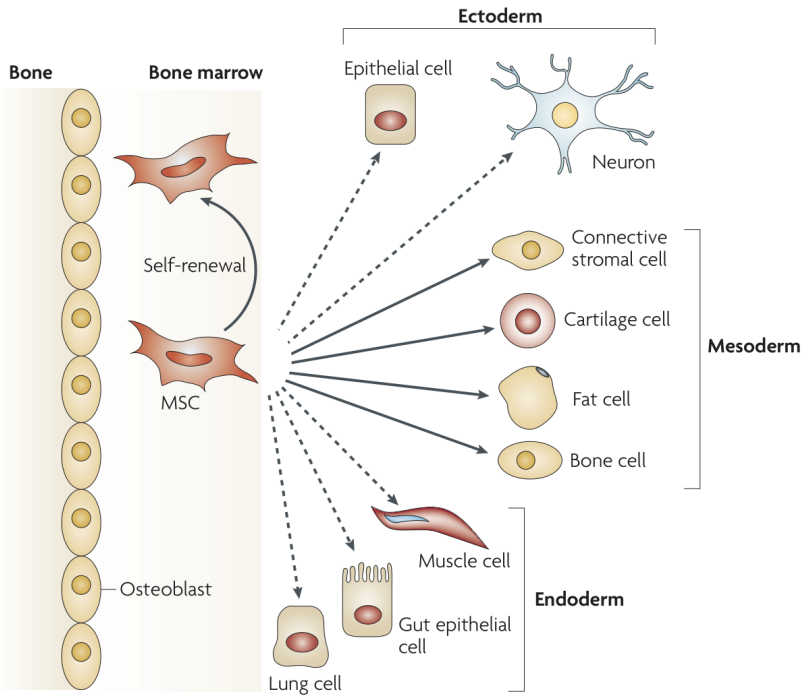

Figure 2.6: Differentiation potential of mesenchymal stem cells. Self renewal (curved arrow), several differentiation potentials towards the mesoderm lineage (solid arrows), and the ectoderm and endoderm lineages (dashed arrows). The latter two are possible *in vitro*, but have not yet been confirmed to occur also *in vivo*.[102]

not in adipose-tissue derived cells, and was correlated with multipotency potential among other cell functions. STRO-1 allows a rather convenient way to prove multilineage capabilities of hMSCs compared to the traditional method, which requires the full differentiation of hMSCs into major lineages.

2.3 Stimuli-responsive substrates

Two new stimuli-responsive substrates are introduced in this thesis. The mechanisms behind the ability to change substrate properties on-demand is based on physical and chemical phenomenons.[30,108] Furthermore, proper characterization of the substrate properties is required to accurately assess the cell response towards these features. Therefore, this chapter will address the theoretical background of the chemical composition and physical properties of the two materials.

2.3.1 Wrinkle formation

Wrinkling is a natural phenomenon, that exists on length scales of meters down to the nanometer scale. It generally occurs, when a flat material is forced to extend or shrink in its plane. This can have unwanted effects, for example the reduced stability in stratified layers.[109] However, when controlled, wrinkling can be used to modify structures or physical properties of nanomaterials. For example, wrinkling can modify optical properties of materials or create channels for microfluidic applications.[110]

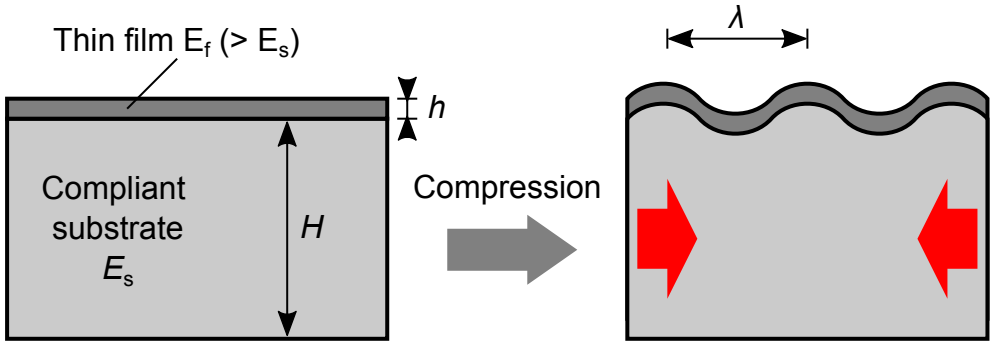

Figure 2.7: Scheme of wrinkle formation. A thin, stiff film is deposited on top of a compliant substrate. When strain is applied by axial compression, wrinkles form on the surface due to local buckling of the thin film. (Adapted from Ohzono *et al.*)[31]

Mathematically, the wrinkling of a thin layer on a soft support can be modeled using Hooke's law in two dimensions:

$$F_{ij} = h\,\overline{E_f}\,[(1-\nu_f)\,\epsilon_{ij} + \nu_f\,\epsilon_{kk}\,\delta_{ij}]. \tag{2.16}$$

Here, ν_f is the Poisson's ratio, h the thickness of the thin film, E is the Young's modulus of the film with $\overline{E}_f = E_f/(1-\nu_f^2)$, and δ_{ij} is the Kronecker delta. The stress tensor ϵ_{ij} includes the initial strains, the gradients of the in-plane displacements, and the rotation caused by the deflection.[111] Under the assumption of an infinitely thick substrate ($H \to \infty$) and after minimizing the total energy in

the system, the following relation is found for the wrinkle wavelength λ:[111]

$$\lambda = 2\pi h \left(\frac{\overline{E}_f}{3\overline{E}_s} \right)^{1/3} \tag{2.17}$$

Using this equation, λ can be predicted from the Young's moduli of the film $\overline{E}_f$ and the substrate $\overline{E}_s$. If these two properties are fixed, λ is proportional to the film thickness h. Additionally, the critical force necessary to induce wrinkles can be calculated by the following equation:[111]

$$F_c = \frac{h\overline{E}_f}{4} \left(\frac{3\overline{E}_s}{\overline{E}_f} \right)^{2/3}. \tag{2.18}$$

The method to determine the substrate elasticity will be addressed later in Section 2.4.1.

2.3.2 Host-guest interactions

One of the fundamental principles in biologic systems is *molecular recognition* which allows the non-covalent, specific binding of biological components among each other, for example receptor-ligand, DNA-RNA, DNA-protein or sugar-protein recognition.[112] Inspired by this principle, host-guest chemistry was developed which is dedicated to the characterization and discovery of new complexes of two molecules that are held together by non-covalent bonding, such as ionic bonding, hydrogen bonding, van der Waals forces and hydrophobic interactions.[79] The extension of host-guest chemistry to build machines on the micrometer scale, resembling molecular motors, was awarded with the Nobel Prize in Chemistry in 2016.[113]

Several studies have created new materials to mimic the dynamic elasticity of tissues *in vitro*. The change in elasticity is usually controlled by external stimuli such as light,[24,115] redox reaction,[116] pH level,[6,117] heat[118] and electric/magnetic fields.[119,120] However, not all materials are applicable for cell culture, since strong light exposure or change of temperature are generally cytotoxic.

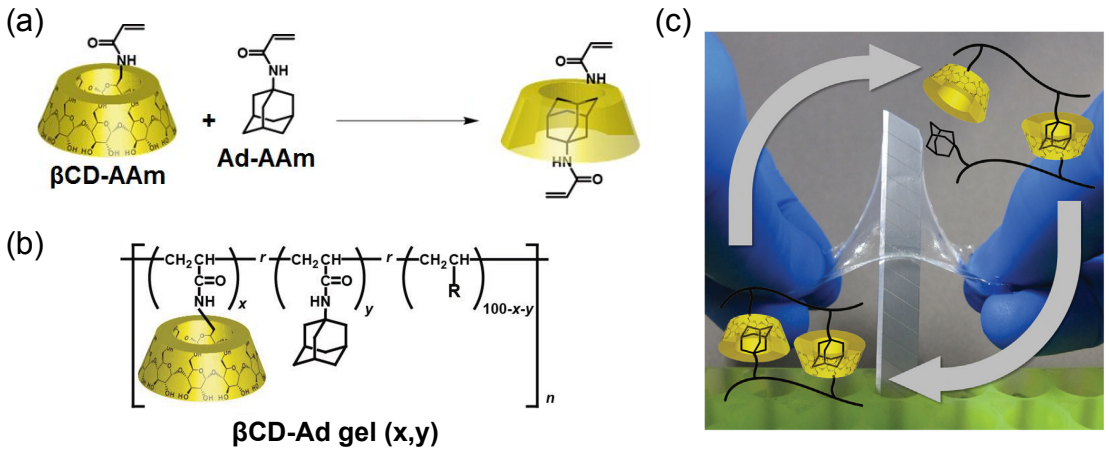

Figure 2.8: Composition of stimuli-responsive host-guest hydrogels. (a) β-cyclodextrin (βCD, yellow cone) and adamantane (Ad) form a highly specific non-covalent connection, called *host-guest interaction*. Both molecules are functionalized with acrylamide (AAm) to be embedded into a polyacrylamide network. (b) Chemical representation of the polymer consisting of the two monomers presented in (a) and pure acrylamide. (c) After radical polymerization a flexible and tear-proof gel is formed. The stability is demonstrated in the image by pulling the gel sheet over a scalpel blade. (Adapted from Nakahata *et al.*)[114]

Originally independent of biological applications, a new hydrogel was developed from polyacrylamide utilizing reversible host-guest connections.[108,114] The core component of this material is acrylamide which forms polymers by radical polymerization. As host-guest moieties beta-cyclodextrin (βCD) and adamantane (Ad) are selected, since they are approved by the Food and Drug Administration (FDA) and therefore considered as biocompatible. By conjugating acrylamide monomers with host-guest monomers, dynamic crosslinks are introduced which form bonds by non-covalent interactions (Figure 2.8a). Mixing these monomers with pure acrylamide and initiating radical polymerization results in polymers with a chemical structure as shown in Figure 2.8b. The concentrations of the monomers (x, y) can be adjusted to fine-tune the elastic properties of the final hydrogel. As demonstrated in Figure 2.8c, the resulting gel is elastic and tear-proof. In previous publications, the self-healing properties were specifically highlighted and applications in material science were discussed.[108,114,121] Following a different approach, this thesis focuses on the ability to change the substrate elasticity on

demand by immersing the gel in a solution with host or guest molecules which block the existing crosslinks and result in a decrease in elastic modulus. Washing the gel with a blank buffer recovers the substrate elasticity to the original properties.[9] These dynamic properties are studied in detail in Chapter 5.

2.4 Experimental background

2.4.1 Indentation of elastic materials

Similar to the shear modulus G', the Young's modulus E is another measurement of elasticity. To measure E, an uniaxial deformation is applied on the sample, i.e. either elongation or indentation, and E is calculated by dividing the applied stress over the resulting strain. In this study, the Young's modulus of a gel is measured by an atomic force microscope (AFM). Figure 2.9a schematically shows the setup of a commercially available AFM. A cantilever is attached to a piezo motor and can be moved freely in x, y and z-direction. The tip of the cantilever is available in a variety of shapes, most commonly applied are cone or sphere shaped tips. A laser is reflected from the cantilever onto a photodiode to register bending of the cantilever. The difference between z-motor position and cantilever bending results in the sample indentation δ as shown in Figure 2.9b. From the force F, which is applied by the bending of the cantilever, and δ, the Young's modulus of the sample can be calculated as explained in the next paragraph.

With increasing indentation, the contact area between probe and sample increases, so that the applied stress is not linear. This problem is solved by the Hertz-model which describes the deformation of elastic bodies in contact.[122,123] In the case of a hard sphere indenting a soft material with a plane surface, the pressure $p(x, y)$ at the contact area is distributed as follows:

$$p(x,y) = p_0 \left(1 - \left(\frac{r}{a}\right)^2\right)^{1/2} \tag{2.19}$$

where a is the radius of the contact area, r is the distance from its center, and p_0 is

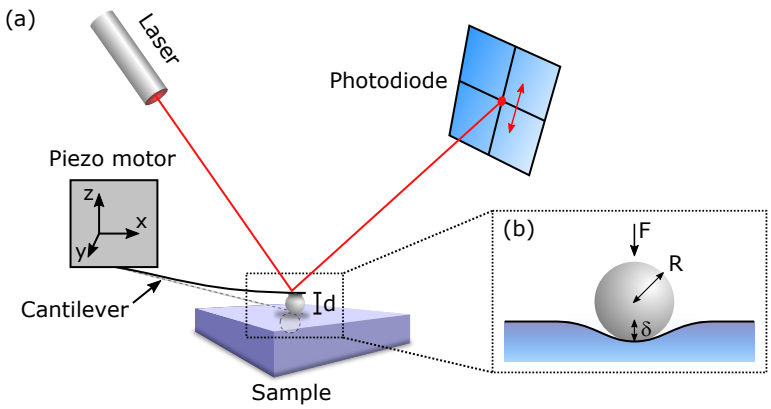

Figure 2.9: Principle of the atomic force microscope. (a) A cantilever with spherical tip is connected to a piezo motor and pressed against the sample surface. A laser beam is reflected on the cantilever and centered on a photodiode to register the cantilever deflection d. (b) The magnified side view of the spherical probe with radius R and the soft sample which is indented by the distance δ.

the pressure at the center of indentation. Consequently, the vertical deformation u_z of the surface also depends on r and is assumed to be of parabolic shape:

$$u_z = \delta - \frac{r^2}{2R}, \tag{2.20}$$

where R is the radius of the sphere. Since the pressure exerted on the surface also acts on the sphere, the effective Young's modulus E^* depends on the individual elasticity of the two bodies E_1 and E_2. However, since the sphere is assumed to be rigid, this relation is simplified as follows:

$$\frac{1}{E^*} = \frac{1-\nu_1^2}{E_1} + \frac{1-\nu_2^2}{E_2} \approx \frac{1-\nu_1^2}{E_1}, \tag{2.21}$$

where ν is the Poisson's ratio. Alternatively, the vertical deformation u_z can be derived by integration of the strain over a circular area $s\ ds\ d\varphi$:

$$u_z = \frac{1-\nu^2}{\pi E}\ p \int_S \int d\varphi\ ds. \tag{2.22}$$

Inserting equation 2.19 into 2.22, shows that a direct relation between the pressure

p_0 and the Young's modulus E exist:

$$p_0 = \frac{2E}{\pi\sqrt{R}}\,\delta\,, \tag{2.23}$$

which can be converted to the force resulting in the equation commonly used for spherical probe indentation with the AFM:[124]

$$F = \frac{4\sqrt{R}}{3}\,\frac{E}{1-\nu^2}\,\delta^{3/2}. \tag{2.24}$$

With this equation the Young's modulus of a sample measured by AFM can be calculated.

2.4.2 Confocal microscopy

Normal light microscopy is only practicable for observation of thin samples, since there is no way to extract 3D-information out of the images. Trying to observe thick samples results in distorted images due to the superposition of diffuse images from out-of-focus objects. To overcome these downsides, confocal microscopy was developed in 1955 by Marvin Minsky. The core of this technique is a set of confocal pinholes which filter the light of a laser beam focused on the sample (Figure 2.10). Out-of-plane signals emitted from the sample are removed by the pinholes by effectively blocking the higher order maxima and minima of the point spread function (PSF). In contrast to conventional microscopes, the image is not observed directly by a camera, but the light intensity is measured by a photomultiplier. To acquire a full 2D-image, the sample is scanned by moving the focal point within the focal plane until each position in the region of interest has been illuminated. This scanning motion is commonly performed by two mirrors in the beam path which are tilted by galvanometer motors (not shown) to achieve fast imaging speed. Consequently, there are three parameters which influence the image brightness: the laser intensity, image resolution, and the scanning speed. Compared to normal wide-field microscopy the lateral resolution limit according to Rayleigh is improved

by a factor of $\sqrt{2}$:[125]

$$r = \frac{0.61\lambda}{\sqrt{2}\,NA}. \tag{2.25}$$

Here, r is the minimum resolvable distance, defined by the overlap of the principal diffraction maximum of the first point with the minimum of the PSF of the second point. λ is the wavelength of the light and $NA = n \sin\theta$ the numerical aperture.

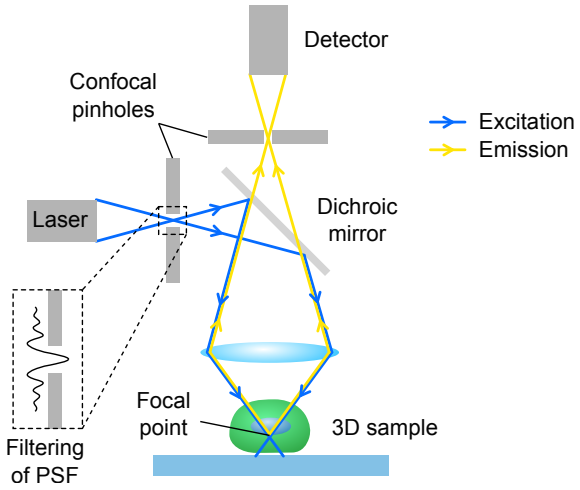

Figure 2.10: Schematic view of a confocal microscope. The excitation light path is indicated in blue and the emission in yellow. A laser is used as light source and focused in one single point withing the 3D sample. Pinholes in the conjugate focal plane filter the point spread function (PSF) and block out emissions from out-of-focus illumination. The light intensity is measured at the detector. In order to create images, the focal point is moved by motorized mirrors (not shown) and the sample is scanned pixel-by-pixel.

Since the focus point is confined in all three dimensions, reconstructions of 3D samples can be acquired by scanning of multiple slices. The resolution in axial direction according to Rayleigh's diffraction limit is calculated as follows:[126]

$$r = \frac{2n\lambda}{NA^2}. \tag{2.26}$$

Thus, the axial resolution is stronger influenced by the numerical aperture compared to the lateral resolution.

Usually the acquired image is decreased in quality by noise, scattering, and blur. This is mainly due to the fact that a single sharp point is always imaged

as a PSF with diffraction patterns around the center. To increase the image contrast and resolution, deconvolution can be applied which aims to reduce the artifacts created by the PSF. There are two categories of algorithms available to deconvolute an image: linear filtering and recursive restoration.[127] A linear filter calculates the Fourier transform of the acquired image, applies a single calculation in the frequency domain, and reverse transforms the image into real space. One of these filters is the Wiener filter, which reduces image blur without any information about the real object:[128]

$$G = \frac{H \cdot S_u}{|H|^2 S_u + S_n}, \tag{2.27}$$

where H is the Fourier transform of the PSF, S_u is the spectral density, obtained by the Fourier transform of the signal autocorrelation, and S_n is the spectral noise, obtained by the Fourier transform of the noise autocorrelation.

Since the improvements of linear filtering are relatively limited, more sophisticated algorithms have been developed that are recursively applied until a certain threshold is reached. The basic idea behind the recursive filters is to estimate the real object, create a blurred version using the PSF, and then compare it with the observed data.[127] Some examples of recursive filters are the Tikhonov-Miller inverse filter,[129] the Carrington algorithm,[129] and the Richardson-Lucy[130,131] algorithm. Since the latter has proved to be most popular, it will be explained shortly. The probability to acquire image i by observation of an object o would be written as $p(o \mid i)$. According to Bayes' theorem, one can predict the probability of two simultaneous events, if the probabilities of the individual events are known:

$$p(o \mid i) = p(i \mid o)\frac{p(o)}{p(i)}. \tag{2.28}$$

Since each pixel in confocal microscopy is acquired successively, the image can be

described as a Poisson process with the following likelihood to acquire an image:[132]

$$p(i \mid o) = \prod_x \left(\frac{(h * o)(x)^{i(x)} e^{(-h*o)(x)}}{i(x)!} \right). \tag{2.29}$$

Here, h refers to the PSF and x to a position in the image.

In this iterative process, each step adds noise to the final result, so that a compromise between noise and sharpness has to be made. In the Richardson-Lucy algorithm this is accomplished by minimization of the following function:[133]

$$f(o) = \sum_x (-i(x) log[(h * o)(x)] + (h * o)(x)). \tag{2.30}$$

While this recursive algorithm has a higher potential to improve the image quality compared to linear filtering, it also requires more computational power. Deconvolution has proven to be most effective in the reconstruction of 3D fluorescence data from high-resolution imaging techniques, such as confocal microscopy, but can theoretically be applied to any image data.[127]

2.4.3 Quantitative analysis of cell adhesion

The cell adhesion can be measured in different ways which all have their own advantages and disadvantages. One of the first methods that were developed is micropipette aspiration, where a part of the cell is sucked into the pipette and pulled until the cell detaches.[134–136] Even though this method was originally developed to measure the viscoelasticity of cells, the adhesion measurement is possible for small cells and relatively cheap as it can be performed with common lab equipment. The disadvantage is, that the applied force is relatively small (0.1 pN – 1 nN) and inverse proportional to the pipette diameter so that with increasing cell sizes the detachment becomes difficult. Furthermore, the direct contact with cells can induce mechanical damage and it is a very slow method when multiple cells are measured for reliable statistics. Another method is the application of atomic force microscopy (AFM) to either scratch the cells off the

surface[137] or to pull cells with a cantilever and measure the force by cantilever deflection[138]. In the latter case, the cell is first adhered to the cantilever, then the cantilever approaches the surface and waits for cell adhesion. Finally, the cell is slowly pulled away from the surface until it detaches.[139] The maximum force with this method is 100 times larger compared to micropipette aspiration (10 pN – 100 nN) and the resolution of the force measurement is relatively high. On the downside, the method is limited to single-cell measurements. Higher cell numbers can be measured with flow chambers allowing the measurement of cell adhesion by detachment of cells by shear stress.[140,141] Microfluidic channels allow to control flow speed precisely and the detachment of cells is observed directly under the microscope. While many cells can be measured contact-free and at the same time, the detachment of cells depends on the time interval of shear exposure, inducing elastic deformation of cells, so that the actual adhesion strength is difficult to estimate.

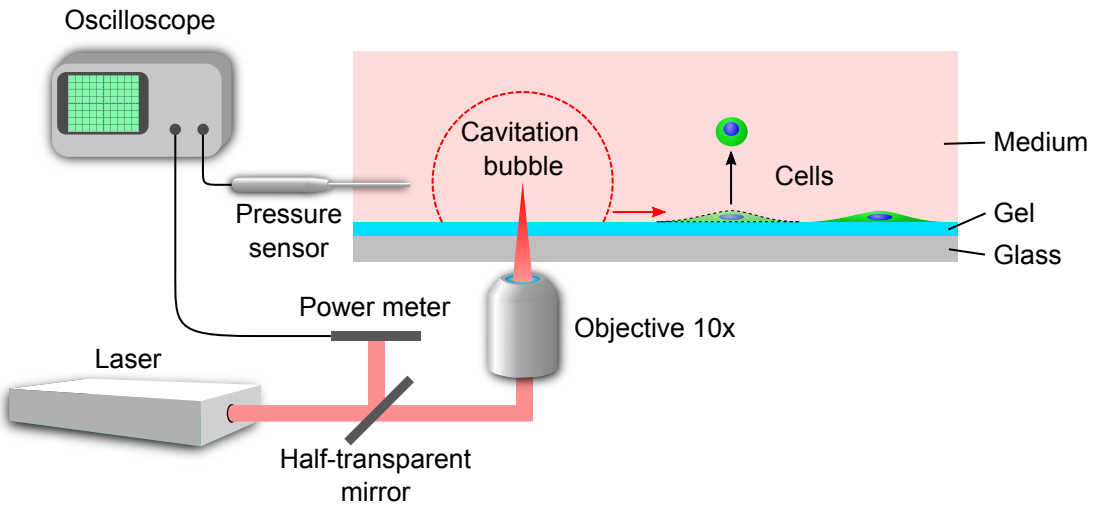

Figure 2.11: Schematic view of the pressure wave assay. A laser is focused close to the substrate surface. Calibration of the setup is performed using a power meter and a pressure sensor. Within the red dashed circle the water is evaporated, creating a cavitation bubble. The pressure decreases with distance to the focal point of the laser, thus cells close to the focus are more likely to be detached.

A new method to quantify adhesion forces was developed by Yoshikawa *et al.* which overcomes the aforementioned downsides.[40,49] The core of this setup is a high-power picosecond laser which is focused close to the surface of the sample

as shown in Figure 2.11. Upon release of a single laser pulse, a cavitation bubble is induced at the focal point by evaporation of the water in the vicinity (red dashed line in Figure 2.11). Formation and collapse of the cavitation bubble creates strong pressure waves which can be tuned by adjusting the laser power. The resulting force is roughly six orders of magnitude larger compared to the previously mentioned methods. Further advantages are the high throughput (>100 cells) with only one measurement and the contact free detachment which does not impact cell viability.[49] The high speed (1640 m/s) and sharp peak (FWHM = 28 ps) of the pressure wave inhibit any inelastic deformation of cells providing accurate measurement of the adhesion force.[49]

Since the cells within the cavitation bubble are likely to be damaged by the water vapor, it is useful to estimate the maximum radius of the bubble. Shock waves induced by cavitation bubbles have been studied before and described by mathematical models.[142,143] If the shock wave velocity $u_s(t)$ is known, the shock wave pressure can be written as a function of distance $r(t)$:[142]

$$p_s(r(t)) = c_1\,\rho_0\,u_s(t)\,(10^{(u_s(t)-c_0)/c_2} - 1) + p_\infty. \tag{2.31}$$

The constant ρ_0 is the density of water before compression by the shock wave, c_0 is the sound velocity in water and p_∞ is the hydrostatic pressure. Rice and Walsh empirically determined the constants $c_1 = 5190\,\mathrm{m/s}$ and $c_2 = 25\,306\,\mathrm{m/s}$.[144] Lauterborn has discovered the highly symmetric rise and collapse of cavitation bubbles in the case of short laser pulse duration and low viscosity of the liquid.[145] Therefore, the duration between the first and second peak in the pressure-time diagram equals two times the collapse time T_c. With this information, the maximum radius of the cavitation bubble can be calculated according to Rayleigh:[146]

$$R_{max} = \frac{T_c}{0.915}\sqrt{\frac{p_\infty - p_\nu}{\rho_0}}. \tag{2.32}$$

Since these calculations assume the bubble expansion in a homogeneous medium, some considerations must be made when the pressure wave is induced close to

an elastic boundary such as a hydrogel. In this case, the cavitation bubble is increasingly deformed the closer the focus is to the elastic surface and can create liquid jets.[143] To accurately determine the strength of the pressure wave as a function of distance, a pressure sensor is recommended which can be used to calibrate the setup.[142]

2.4.4 Traction force microscopy

First developed by Munevar *et al.*[147] traction force microscopy has become a widely popular method to reveal active cellular forces which were introduced in Section 2.1.2. In this method, fluorescent beads are embedded in a compliant substrate, such as a hydrogel (Section 2.1.3). If a cell is exerting contractile forces on the substrate, the displacement of the beads is measured and can be translated to the two-dimensional force field. While the practical details are explained in Section 3.2.4, the mathematical background will be explained in the following paragraphs.

Solution of the inverse problem

In order to calculate the force from the bead displacement analytically, one has to assume the substrate as a two-dimensional half-space, i.e. the thickness of the substrate is infinite. This is applicable, if the real thickness of the substrate is sufficiently large in comparison to the displacement on the surface. Furthermore, forces are considered as two-dimensional, i.e. forces normal to the substrate surface are neglected.

The traction field is considered as the force per unit area, which is exerted by a cell on the substrate surface. In the experiment the local displacements are measured from which the traction field can be calculated which is known as the *inverse problem*. In order to solve it, one has to first consider the *forward problem* which calculates the displacement field $\vec{u}(\vec{x})$ from the traction field $\vec{f}(\vec{x})$ at position

$\vec{x}$ as follows:[148]

$$u_i(\vec{x}) = \int \sum_j G_{ij}(\vec{x} - \vec{x}')\, f_i(\vec{x}')\, d\vec{x}'. \tag{2.33}$$

Translating this integration into matrix notation results in a convolution with the unknown matrix $\mathbf{G}$ and can be written in short:

$$\vec{u} = \mathbf{G} \otimes \vec{f}. \tag{2.34}$$

This problem was solved by Bussinesq using the following Green's function:[148,149]

$$\begin{aligned} G_{ij}(\vec{x}) &= \frac{1+\nu}{\pi E}\left[(1-\nu)\frac{\delta_{ij}}{r} + \nu\frac{x_i x_j}{r^3}\right] \\ &= \frac{1+\nu}{\pi E r^3}\begin{pmatrix} (1-\nu)r^2 + \nu x^2 & \nu xy \\ \nu xy & (1-\nu)r^2 + \nu y^2 \end{pmatrix}. \end{aligned} \tag{2.35}$$

Here, ν is the Poisson's ratio, E is the Young's modulus of the substrate, and $r = |\vec{x}|$.

Attempting to solve the equation for $f(\vec{x})$ raises the problem that the matrix $\mathbf{G}$ is not diagonal in $\vec{x}$ and therefore cannot be inverted easily. This is unavoidable, because the traction at one given point always depends on the surrounding traction of other points, causing the convolution in Equation 2.34. A solution can be found by application of the Fourier transform which transforms convolutions into a simple multiplication. This approach is commonly called the *Fourier transform traction cytometry* (FTTC).[150] With the notation $\mathcal{F}(\mathbf{G}) = \tilde{\mathbf{G}}$ one can write the traction field as follows:

$$\vec{f} = \mathcal{F}_2^{-1}(\tilde{\mathbf{G}}^{-1}\tilde{\vec{u}}), \tag{2.36}$$

where $\mathcal{F}_2^{-1}$ describes the two-dimensional inverse fourier transform. Hence, the

Fourier transform of the Boussinesq equation (2.35) is needed, which yields:

$$\tilde{\mathbf{G}}(\vec{k}) = \frac{2(1+\nu)}{E\,k^3} \begin{pmatrix} (1-\nu)k^2 + \nu k_y^2 & \nu k_x k_y \\ \nu k_x k_y & (1-\nu)k^2 + \nu k_x^2 \end{pmatrix}. \tag{2.37}$$

It should be noted that the components of the wave vector are defined as $k^2 = k_x^2 + k_y^2$. Inserting this function into Equation 2.36 solves the inverse problem and the force field can now be derived from the displacement field.

Dipole and quadrupole analysis

One advantage of the FTTC approach is the additional information from the easily derived moments of the traction field. The zero-order moment is always zero, since the cell is considered to be in a micro-equilibrium state, where all net forces cancel out, i.e. there is no displacement of the center of mass: $\tilde{\vec{f}}(0) = 0$.

Less trivial, the first order moments reveal forces associated with contraction or torque. Each entry of the matrix consist of a traction in x or y-direction weigthted by their x or y coordinate, leading to four possible combinations. For example, a positive traction in y-direction multiplied with the x-coordinate indicated a counter-clockwise rotation while a negative traction in x-direction multiplied with the x-coordinate results in a contraction along the x-axis. Schematically, one can imagine the meaning of each matrix element as follows:[31,150]

$$\begin{bmatrix} xf_x & xf_y \\ yf_x & yf_y \end{bmatrix} \quad \widehat{=} \quad \begin{bmatrix} \rightarrow\leftarrow & \circlearrowleft \\ \circlearrowleft & \downarrow\uparrow \end{bmatrix} \tag{2.38}$$

Accurately, the matrix elements are defined as follows:

$$M_{ij} = \frac{1}{2} \int \left[x_i f_j(\vec{x}) + x_j f_i(\vec{x}) \right] dx_i dx_j. \tag{2.39}$$

Since rotational motion in cells is negligible, $\mathbf{M}$ can be diagonalized to obtain the two eigenvectors and eigenvalues. The eigenvalue with larger absolute value

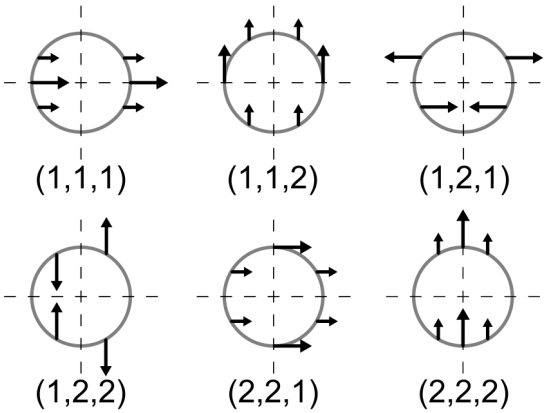

Figure 2.12: Schematic visualization of the quadrupole tensor. Black arrows indicate the direction and strength of the force components. The numbers in parenthesis refer to the three indices of the quadrupole tensor (i,j,k). The two combinations (1,2,1) and (1,2,2) are highly relevant in cell locomotion as they imply a front-rear asymmetry. Adapted from Tanimoto *et al.*[3]

equals the major dipole moment D_{max} and the smaller eigenvalue equals the minor dipole moment D_{min} while the eigenvectors indicate the direction of each dipole moment.[3] The ratio of both dipole moments is considered a measure of the traction polarity of the cell.

Apart from the individual dipole moments, a commonly mentioned quantity is the net contractile moment[150–152] μ which is a measurement of the contractile strength of the cell:

$$\mu = \mathrm{tr}(\mathbf{M}) = M_{xx} + M_{yy}. \tag{2.40}$$

Another important quantity is the total strain energy U, which is the energy transferred from the cell to the substrate by tactile strain. It is calculated as follows:

$$U = \frac{1}{2} \int \vec{f}(\vec{x}) \cdot \vec{u}(\vec{x})\, dx\, dy. \tag{2.41}$$

Note that μ and U are very different in their physical meaning even though they share the same unit *Joule*: U is an energy calculated by *force times displacement* and μ is a moment calculated by *force times distance from origin*.

The moment analysis can be further extended to the second moment, also called *quadrupole*. Here, the calculations become significantly more complicated as the quadrupole tensor has six components which are described as follows:

$$M_{ijk} = \frac{1}{2} \int_S x_i x_j f_k(\vec{x})\, dS. \tag{2.42}$$

Schematically, this can be seen as shown in Figure 2.12. Here, the three indices (i,j,k) of the quadrupole tensor are shown in parenthesis and the direction of the force is indicated by black arrows. Longer arrows correlate with a stronger force. The quardupole is highly relevant for cell locomotion, because at low Reynold's numbers, i.e. with high friction and low inertia, a bipolar motion will always result in zero net movement.[153,154] Therefore, the tensor components with indices (1,1,1), (1,1,2),(2,2,1) and (2,2,2) are usually negligible as they do not result in a a net movement. However, directed motion becomes possible with a break in front-rear symmetry, as indicated by indices (1,2,1) and (1,2,2) (Figure 2.12). In these cases the cell is contracting on one side and relaxing on the other side, which effectively pushes the center of mass in direction of the relaxed side.

3 Materials and methods

3.1 Wrinkled substrates

3.1.1 Materials

Poly(dimethylsiloxane) (PDMS, Sylgard 184) was purchased from Dow Corning (Midland, MI, USA), and fetal bovine serum (FBS), goat anti-mouse Alexa Fluor 488 conjugate, and rhodamine-phalloidin were from Thermo Fisher Scientific (Tokyo, Japan). Penicillin, streptomycin, and phosphate-buffered saline (PBS) were purchased from Nacalai Tesque (Kyoto, Japan), HiLyte 488-labeled fibronectin was purchased from Cytoskeleton Inc. (Denver, CO, USA), and LifeAct-TagGFP2 and Torpedo lipofection reagent were obtained from Ibidi (Munich, Germany). Unless stated otherwise, other chemicals were purchased from Sigma-Aldrich (St. Louis, MO, USA) and used without further purification

3.1.2 Fabrication of Substrates with Periodic Wrinkles

The substrates displaying periodic wrinkles were fabricated by slightly modifying the protocols reported previously[14] (figure 3.1). In brief, PDMS was polymerized on a silicon wafer (Furuuchi Chemicals, Tokyo, Japan) and cut into blocks of $12 \times 12 \times 5\,\mathrm{mm}^3$ size. The PDMS blocks were treated with ambient air plasma for 20 s (PDC-001, Harrick Plasma, USA), followed by spin-coating (MS-A150, Mikasa Corporation, Hokkaido, Japan) with a solution of poly-pyromellitic dianhydride-co-4,4'-oxidianiline (polyamic acid) in N-methylpyrrolidone (NMP) at 5000 rpm for 60 s. The solvent was evaporated by preheating at 90 °C for 5 min, and the samples were axially compressed by 3 % strain and cured at 180 °C for 30 h during

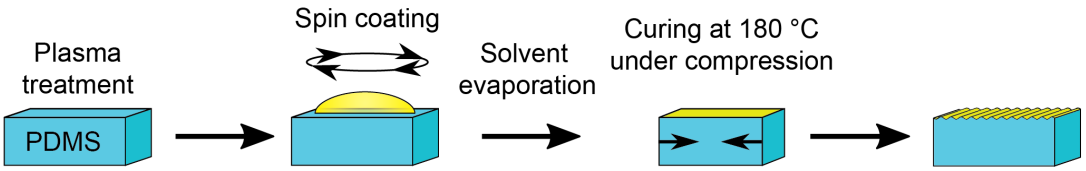

Figure 3.1: Fabrication of Substrates Displaying Periodic Wrinkles. The poly(dimethylsiloxane) (PDMS) block was first treated with ambient air plasma, then polyamic acid dissolved in NMP was spin-coated. A thin polyimide layer was formed by curing the sample at 180° under axial compression. The release of axial strain resulted in the periodic wrinkle structures.

the formation of polyimide. The wrinkles were formed upon release of the external strain. Three-dimensional structures of wrinkles were characterized using an atomic force microscope (NanoWizard, JPK Instruments, Berlin, Germany) with a pyramidal cantilever (MLCT, Bruker, Billerica, USA).

3.1.3 Modulation of Wrinkle Orientation

To dynamically modulate the wrinkle orientation, an external strain was exerted on the substrate in the direction of wrinkle orientation.[39] A strain above 10 % induced reorganization of the wrinkle structure perpendicular to the original wrinkle orientation. To control the strain accurately, a custom-built motorized pusher was used including a cell incubation chamber, which can be mounted on a microscope stage (Strex, Osaka, Japan).

3.1.4 Cell Culture, Immunostaining, and Transfection

C2C12 mouse myoblast cells (<20 passages) purchased from RIKEN BRC Cell Bank (Tsukuba, Japan) were cultured in RPMI-1640 medium supplemented with 10 % (v/v) FBS, 100 U/mL penicillin, and 100 µg/µL streptomycin. Before seeding the cells, wrinkled substrates were incubated with 30 µg/µL human fibronectin for 2 h at room temperature. The cells were detached from the culture flasks using 0.25 % trypsin-EDTA solution, and 2×103 cells/cm^2 were seeded on the wrinkled substrate. For immunostaining, the cells were fixed with 0.02 g/mL paraformaldehyde permeabilized with 0.1 % Tween-20 and blocked with 1 % BSA in PBS. Then

the cells were incubated with mouse antivinculin, goat antimouse Alexa Fluor 488 conjugate, rhodamine-phalloidin, and 4',6-diamidino-2-phenylindole (DAPI), each for 1 h at room temperature. To visualize actin fibers in living cells, C2C12 cells were transfected with LifeAct-TagGFP2 using Torpedo lipofection reagent following the manufacturer's protocol.

3.1.5 Image Acquisition and Analysis

Cells on wrinkled substrates were imaged with an upright laser scanning confocal microscope (FV1000, Olympus, Tokyo, Japan) equipped with a water dipping objective (40×, N.A. 0.8). Morphometric parameters, such as the aspect ratio and circularity, and the orientation of cells with respect to the wrinkle direction were extracted using Fiji software.[155] Each cell was fitted as an ellipse from the calculated first- and second-order moments of the binary image,[156] and then the aspect ratio was defined as the fraction of the major and minor axis of the fitted ellipse. The order parameters of cells and actin filaments were calculated using a self-written routine in MatLab (MathWorks, Natick, USA) as described before.[41,42] In short, the original image was convoluted with a series of elongated Laplacians of Gaussian kernels, which were rotated n times between 0 and $\pi - \pi/n$. The application of an intensity threshold yields the orientation of fibers at each pixel. Finally, the order parameter can be calculated from the histogram of fiber orientations.

3.2 Host-guest gels

3.2.1 Materials

The host-guest monomers beta-cyclodextrin-acrylamide (βCD-AAm) and adamantane-acrylamide (Ad-AAm) were kindly provided by Professor Masaki Nakahata, Osaka University, Japan. Ammonium-peroxidisulfate (APS) and Tetramethylethylenediamine (TEMED) were purchased from Bio-Rad (Hercules, CA, USA). Vinyltrimethoxysilane was obtained from VWR (Wayne, PA, USA). Polydimethyl-

siloxane (PDMS, Sylgard 184) was purchased from Dow Corning (Midland, MI, USA). Mesenchymal Stem Cell Growth Medium MSCGM™ was purchased from Lonza (Basel, Switzerland). Texas Red™-X Phalloidin and STRO-1 antibody were obtained from Thermo Fisher Scientific (Waltham, MA, USA). CellBrite™ green was purchased from Biotium (Fremont, CA, USA). Unless stated otherwise, other chemicals were purchased from Sigma-Aldrich (St. Louis, MO, USA) and used without further purification.

3.2.2 Fabrication of host-guest gels

Host-guest gels were prepared as described previously.[9] In short, the monomer solution was created by dissolving 71.3 mg βCD-AAm and 12.3 mg Ad-AAm in 1 mL distilled water. This solution was stirred at 90° for 3 h. After cooling down to room temperature, 133.6 mg acrylamide (AAm) and 4.6 mg APS were added. This solution was filtered with a pore size of 0.22 µm. Glass slides with a diameter of 25 mm were rinsed with solvents and further processed by *RCA Clean*.[157] Half of the glasses were silanized using vinyltrimethoxysilane. To initiate the polymerization, 0.3 % (v/v) TEMED was added to the monomer solution and 25 µL was pipetted onto the silanized glass. The non-silanized glass was then placed on top so that the monomer solution was spread evenly between both glasses. After 15 min the gel was polymerized and was sticking to the silanized glass. The top glass was removed and the gel was washed in 50 % DMSO for 1 day and in distilled water for 2 days. The gel was then glued into a petri dish using PDMS. Fibronectin was bound covalently to the substrate surface by the cross-linker Sulfo-SANPAH as described previously.[158,159] The elastic modulus of the gel was measured with an atomic force microscope (NanoWizard, JPK Instruments, Berlin, Germany) using a colloidal probe cantilever (CP-PNPL-BSG-B, NanoAndMore, Wetzlar, Germany) with a diameter of 10 µm and a force constant of 0.08 N/m.

3.2.3 Cell culture

hMSCs were isolated and cultured as described before.[160] Bone marrow from healthy donors for allogeneic transplantation was taken after written consent using guidelines approved by the Ethic Committee on the Use of Human Subjects at the University of Heidelberg. The cells were cultured at 37° in a humidified atmosphere. As a cell culture medium MSCGM was used, which was exchanged every second day. In order to reduce the substrate elasticity, adamantanecarboxylic acid (Ad-COOH) was added to the cell culture medium, filtered sterile and added to the samples after removing the previous medium. To return the substrate to the original elasticity, the medium was exchanged 3 times followed by 30 min incubation at 37° between each step. Viability assays were performed by incubating the cells with different concentrations of Ad-COOH for 24 h followed by incubation with water-soluble tetrazolium salt (WST-1) for 4 h. The WST-1 is cleaved to formazan by cellular enzymes which becomes visible by a change in color. Using a photometer (TECAN, Männedorf, Switzerland) the absorbance at the wavelength of 450 nm was measured relative to a control sample without Ad-COOH.

For immunostaining, cells were incubated with Texas Red™-X Phalloidin or mouse anti-STRO-1 antibody followed by goat anti-mouse antibody conjugated with Alexa Fluor 488 for 1 h each. Nuclei were stained with 4',6-diamidino-2-phenylindole (DAPI). Images were acquired with a Nikon C2 Plus confocal microscope equipped with a 60 × water immersion objective. Analysis of the cell morphology was performed in Fiji.[155]

3.2.4 Traction force microscopy

Fluorescent beads with a diameter of 0.2 µm were embedded in the top layer of the host-guest gel as follows. After suspending the beads in distilled water, the suspension was spread on the RCA-cleaned cover glass and dried with nitrogen gas. This glass was then placed upside down onto the monomer solution during the polymerization process. The beads which adhered to the glass remained in a

confined layer below the gel surface after polymerization. Calculation of the force field was performed in MATLAB (MathWorks, Natick, MA, USA) as described previously.[160,161] The MATLAB script was kindly provided by Professor Masaki Sano, Tokyo University, Japan.

3.2.5 Pressure wave assay

Similar to a previous publication,[7] a pulsed Nd:YAG laser system ($\lambda = 1064\,\mathrm{nm}$, $\tau_L = 28 \pm 3\,\mathrm{ps}$, EKSLPLA, Vilnius, Lithuania) was coupled to an inverted microscope (Eclipse TE2000-U, Nikon Europe) with a 10×objective. Before the experiments, the system was calibrated using a piezoelectric pressure sensor (Müller Instruments, Oberursel, Germany). Cells were seeded onto stiff host-guest gels at a density of $500\,\mathrm{cells/cm^2}$. After 4 days of equilibration time, the substrate elasticity was reduced as desired, followed by another 4 days of incubation. The laser was then focused on four different positions with a distance of at least 1 cm and the pressure wave was induced at each position at 700 µm above the substrate surface two times. For the first pressure wave the laser power is reduced to 0.5 mJ, which resulted in a weak pressure wave to remove dead or non-adherent cells. The second laser pulse is initiated at 12.7 mJ (100 %) laser power. Before and after each pulse a bright field image of the size $4 \times 3\,\mathrm{mm}$ was recorded by stitching. Cells which were still adhered after the second laser pulse were marked manually using the software Fiji[155] and their distance to the laser focus was calculated. If a cell has changed its adhesion area significantly, it was considered to be detached.

3.2.6 Cyclic change of substrate elasticity

hMSCs wee seeded on the initially stiff gels ($E = 25\,\mathrm{kPa}$) for 4 days after which the substrate elasticity was switched to soft first ($E = 8\,\mathrm{kPa}$) and then changed every 2, 4, 7, 10 or 20 days. Switching the substrate elasticity from stiff to soft was achieved by exchanging the medium with fresh medium containing 5 mM Ad-COOH. Returning to the stiff substrate required 3 times exchanging to the

unmodified medium followed by 30 min incubation at 37°. After 20 days the cell were fixed and the density was measured by counting the nuclei per area. Cells were stained with mouse anti-STRO-1 to assess the mutipotency.

4 Dynamic contact guidance of myoblast cells

Biological tissues are highly anisotropic in their shape and composition. Many tissues, such as muscle fibers, rely on the anisotropy in order to fulfill their functions. This internal ordering originates from single cells, as several properties such as cell orientation, migration direction and proliferation are influenced by the topography of their environment which is called *contact guidance*.[3,5,8,34] Even in matured tissue, cells are able to sustain the structure and functional integrity reliably.[19] Earlier studies have proven that cells follow geometric cues, like grooves and ridges or periodic wrinkles, by aligning their shape and cytoskeleton in the direction of the topography.[28,162] However, most studies are limited to a static topography in contrast to biological tissues which are changing over time during aging and diseases. Therefore, a new substrate was developed in this study which features a wrinkled surface and is able to switch the angle of the wrinkle direction *in situ*. This enables the immediate observation of cell responses to a radical change in surface topography.

4.1 Characterization of the wrinkled substrate

In this section, the wrinkled substrate is characterized regarding its geometry, surface wettability and protein coating. Figure 4.1a Shows an image acquired by AFM imaging which reveals the height profile of the wrinkled substrate. A line profile was extracted perpendicular to the wrinkle direction and is plotted below. Here, the wavelength $\lambda = 2.5 \pm 0.1\,\mu m$ is measured as the peak-to-peak

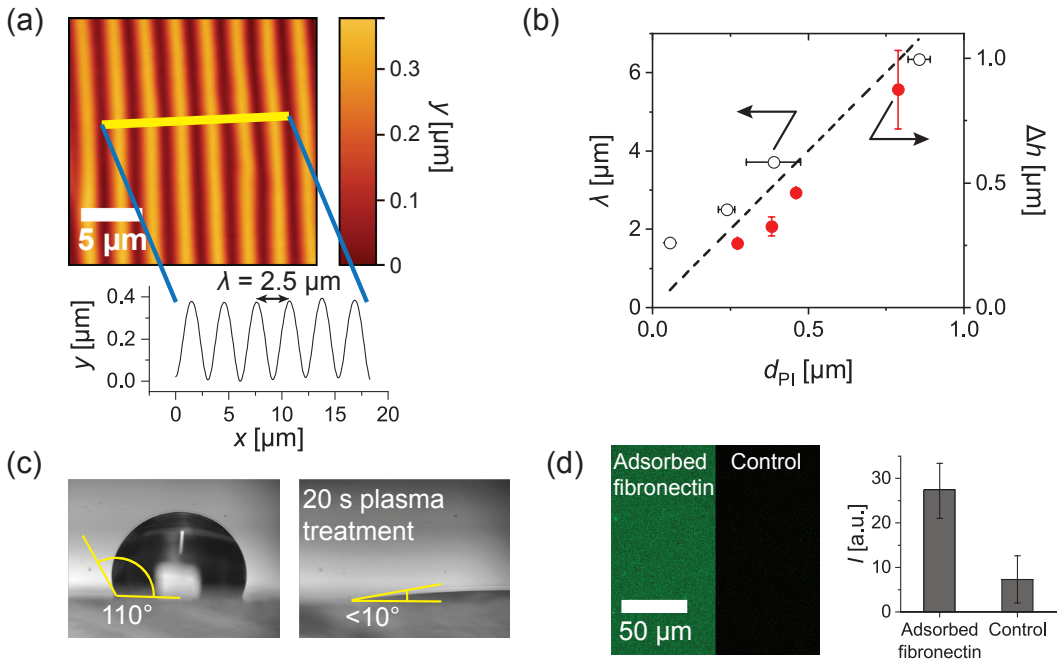

Figure 4.1: (a) AFM height map of a surface with periodic wrinkles. The profile along the yellow line is extracted below and yields a wavelength of $\lambda = 2.5 \pm 0.1\,\mu m$ and an amplitude of $\Delta h = 0.32 \pm 0.01\,\mu m$. (b) The Wavelength λ (open circles) and amplitude Δh (solid circles) of wrinkles are plotted as a function of polyimide thickness d_{PI}. λ was fitted with a linear function as indicated by the broken line. It should be noted that the ratio $\Delta h/\lambda = 0.13$ is almost constant for all samples. (c) Contact angle of a water droplet on PDMS before and after plasma treatment. (d) Fluorescence image of labeled fibronectin adsorbed to polyimide. The bar plot reveals a strong signal of adsorbed fibronectin compared to control.

distance and the height $\Delta h = 0.32 \pm 0.01\,\mu m$ is defined as the difference between peak and trough. In Figure 4.1b the wavelength λ and amplitude Δh are plotted against the polyimide thickness d_{SI}. The exact concentrations of polyamic acid in NMP (v/v) and resulting thickness d_{PI} are listed in Table 4.1. It should be noted that λ also depends on the ratio of Young's modulus E of polyimide and PDMS as shown by Equation 2.17. Both values for E were kept constant in this study. $E_{PDMS} \approx 10\,MPa$ was measured by AFM indentation and $E_{PI} \approx 2.5\,GPa$ is given by the manufacturer. The ratio between λ and Δh is almost constant and relatively low ($\Delta h/\lambda \approx 0.13$), therefore displaying a rather shallow wrinkle profile.

In order to form a stable connection between PDMS and polyimide, the surface of the PDMS is treated by ambient plasma for 20 s. As shown in Figure 4.1c, the

Polyamic acid [% (v/v)]	d_{PI} [µm]
2.3	0.06 ± 0.01
3.0	0.24 ± 0.03
3.6	0.39 ± 0.09
4.8	0.86 ± 0.04

Table 4.1: Polyamic acid concentration and resulting polyimide thickness d_{PI}. A part of the polyimide layer was removed by scratching to measure d_{PI} by atomic force microscopy.

contact angle changes from $\varphi = 110°$ to $\varphi < 10°$. The substrates were incubated with fibronectin labeled with HiLyte 488 to confirm fibronectin adhesion to polyimide. Figure 4.1d shows the fluorescence image after incubation with 30 µg/mL fibronectin for 2 h at room temperature with a control sample on the right. Next to the image the average intensity of the coated sample and a control sample is plotted which shows a significant difference between both samples.

4.2 Directional ordering of cells and cytoskeleton

The ordering of cells and actin was studied separately to determine the individual influence of the wrinkled topography quantitatively. Starting with the cell ordering, Figure 4.2a shows C2C12 cells 4 h after seeding on wrinkles with a wavelength of $\lambda = 1.7$ µm. The image presents an overlay of fluorescence and differential interference contrast (DIC) microscopy. The actin cytoskeleton is shown in green and the nuclei in blue. An ellipse (red) was fitted to the cells to determine its orientation defined by the major axis of the ellipse (red line). The angle between the major axis and the wrinkle direction is defined as α_{cell}, as shown in the inset. Individual distributions of α_{cell} are shown in Figure 4.2b for each wavelength λ. Each distribution was fitted with a Gaussian function (broken lines). The broadest distribution, defined by the full width at half maximum (FWHM), was observed for $\lambda = 1.7$ µm at $FWHM_{cell,1.7\,µm} = 68 \pm 15$ degree. With increasing λ the FWHM decreased, i.e. the distribution was sharper. For quantitative analysis of the collective cell the order parameter was calculated according to the following

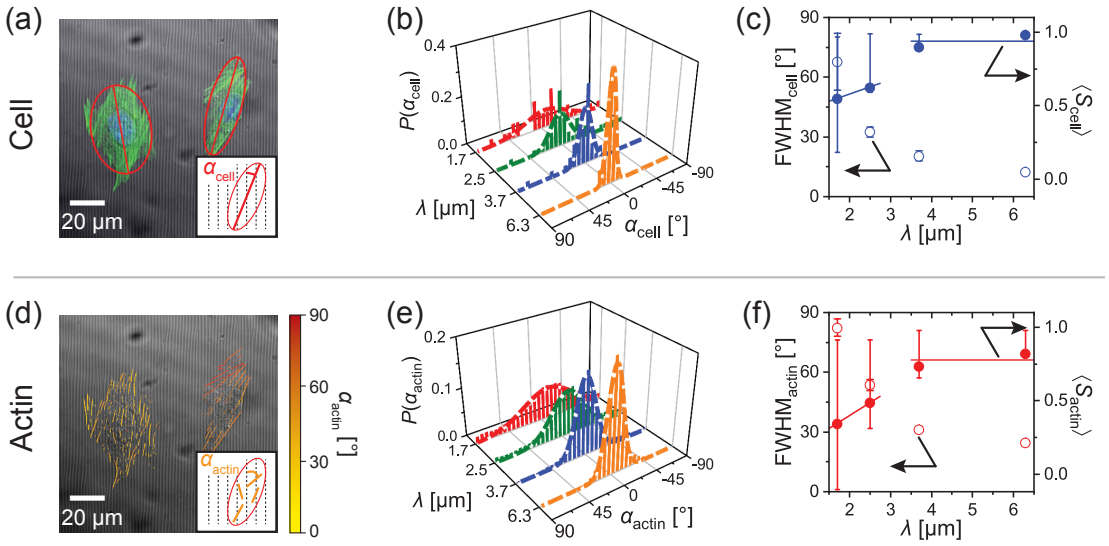

Figure 4.2: (a) C2C12 cells on wrinkles with $\lambda = 1.7\,\mu m$. The image is an overlay of the wrinkles imaged by DIC (grey) and actin (green) and the nucleus (blue), which are imaged by fluorescnece microscopy. The red ellipses are fitted to the cell shape while the red line indicates the major axis. In the inset the definition of α_{cell} is explained which equals the angle between major axis of the ellipse and wrinkle direction. (b) The distribution of α_{cell} is plotted for each wavelength λ and fitted with a Gaussian function (broken lines). (c) Full width at half maximum (FWHM) of the α_{cell}-distributions and order parameter of cells $\langle S_{cell} \rangle$ are plotted against λ. (d) Overlay of the DIC image with the detected actin filaments. The color code represents the angle α_{actin} which is the angle between individual actin filaments and the wrinkle direction as shown in the inset. (e) The distribution of α_{actin} is plotted for each wavelength λ and fitted with a Gaussian function (broken lines). (f) FWHM of the α_{actin}-distributions and order parameter of actin $\langle S_{actin} \rangle$ are plotted against λ.

formula:

$$\langle S_{\text{cell}} \rangle = \frac{\sum_i AR_i \cos(2\alpha_i)}{\sum_i AR_i}. \tag{4.1}$$

This order parameter is weighed by the aspect ratio AR_i which is defined as the fraction of major and minor axis of the ellipse fit. In Figure 4.2c the $\text{FWHM}_{\text{cell}}$ (open circles) and order parameter $\langle S_{\text{cell}} \rangle$ (closed circles) are plotted against λ. $\langle S_{\text{cell}} \rangle$ starts at 0.55, indicating moderate alignment at $\lambda = 1.7\,\mu\text{m}$, and increases to $\langle S_{\text{cell}} \rangle \approx 0.91$ at $\lambda = 3.7\,\mu\text{m}$. For higher λ, $\langle S_{\text{cell}} \rangle$ does not increase any further. On the other hand, the $\text{FWHM}_{\text{cell}}$ decreases continuously with increasing λ, with the most noticeable change from $\lambda = 1.7\,\mu\text{m}$ ($\text{FWHM}_{\text{cell}} \approx 70°$) to $\lambda = 2.5\,\mu\text{m}$ ($\text{FWHM}_{\text{cell}} \approx 35°$). Overall, this indicates that the cells have already reached their maximum alignment at $\lambda = 3.7\,\mu\text{m}$.

The lower images in Figure 4.2 represent the results of actin ordering analysis. In Figure 4.2d an overlay of DIC and the detected actin filaments is shown. The color of each filament indicates the angle α_{actin} which is the angle between each filament and the wrinkle direction as shown in the inset. In Figure 4.2e the distribution of α_{actin} is plotted for each λ and fitted with Gaussian functions (dashed lines). The FWHM decreases monotonically from $\text{FWHM}_{\text{actin},1.7\,\mu\text{m}} = 82 \pm 5°$ to $\text{FWHM}_{\text{actin},6.3\,\mu\text{m}} = 25 \pm 1°$. For the nematic order parameter of actin filaments the following equation was applied:

$$\langle S_{\text{actin}} \rangle = \frac{\sum_i A_i \cos(2\alpha_i)}{\sum_i A_i}, \tag{4.2}$$

where A_i is the area of individual filaments measured by the number of pixels multiplied by the pixel size. In Figure 4.2f the order parameter $\langle S_{\text{actin}} \rangle$ and the $\text{FWHM}_{\text{actin}}$ are plotted against λ. It can be seen that the order parameter is lower compared to $\langle S_{\text{cell}} \rangle$ on the same substrate, e.g. $\langle S_{\text{actin},1.7\,\mu\text{m}} \rangle \approx 0.34$ is smaller compared to $\langle S_{\text{cell},1.7\,\mu\text{m}} \rangle \approx 0.55$. An increase in λ from 1.7 to 3.7 µm also results in an increase of the order parameter to $\langle S_{\text{actin},1.7\,\mu\text{m}} \rangle \approx 0.73 \pm 20$ which indicates an increased alignment of actin filaments towards the wrinkle direction. A further

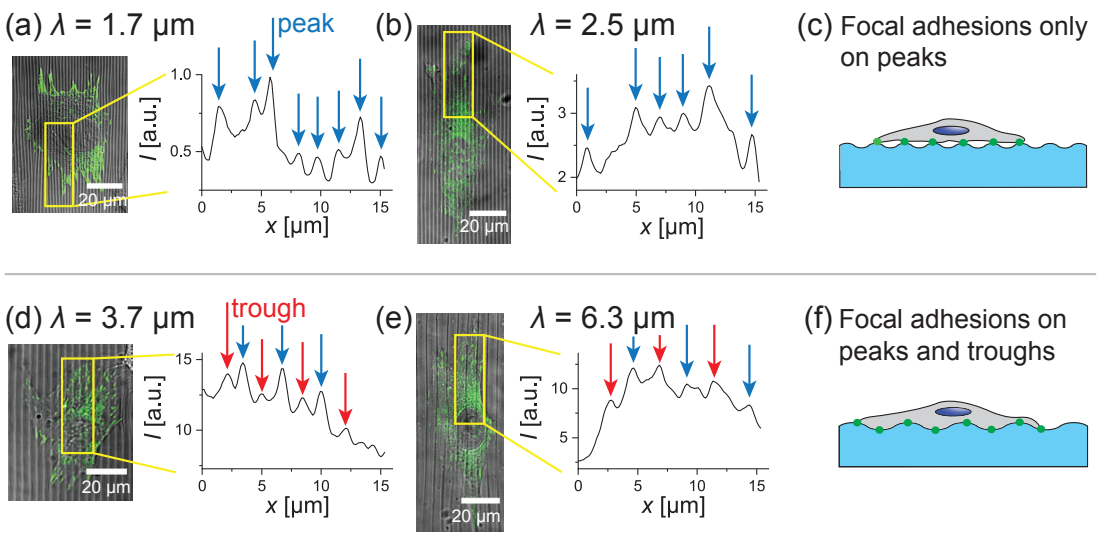

Figure 4.3: Focal adhesion location depending on wrinkle wavelength. (a,b,d,e) On the left side of each panel an overlay of fluorescence signal of vinculin and DIC is shown. The fluorescence signal inside the yellow box is integrated in wrinkle direction and plotted on the right side. Blue arrows indicate locations where vinculin is found on the peak of wrinkles while red arrows point towards vinculin accumulation in the trough. In (a) $\lambda = 1.7\,\mu m$ and (b) $\lambda = 2.5\,\mu m$ vinculin is mostly located at the peaks, suggesting a flat cell membrane as shown in panel (c). In contrast, in (d) $\lambda = 3.7\,\mu m$ and (e) $\lambda = 6.3\,\mu m$ vinculin is found on peaks and troughs so that the cell membrane follows the wrinkle undulation as schematically shown in panel (f).

increase in λ to 6.3 µm did not increase the order parameter significantly.

4.3 Localization of focal adhesions

The asymptotic behavior of both order parameters $\langle S_{\text{cell}} \rangle$ and $\langle S_{\text{actin}} \rangle$ implies the existence of a threshold wavelength λ^* between 2.5 and 3.7 µm which differentiates between the ordered and disordered state of both, the cells and the actin cytoskeleton. To assess this hypothesis, the location of focal adhesions of cells was measured by fluorescence staining of vinculin, a major contributor to the adhesion complex. In Figure 4.3a,b,d,e the left side shows the fluorescence signal of vinculin as an overlay of the DIC image. The fluorescence signal inside the yellow box is integrated in wrinkle direction and plotted on the right side. Blue arrows point towards locations where the vinculin signal correlates with the peaks in the wrinkle profile. Red arrows point towards a vinculin signal inside the wrinkle trough.

It should be noted that the mean distance between blue arrows roughly correlates with the wavelength of the wrinkles.

At a wavelength of $\lambda = 1.7\,\mu m$ (Figure 4.3a) and $\lambda = 2.5\,\mu m$ (Figure 4.3b) all maxima of the vinculin signal were found on the wrinkle peaks. Since a strong vinculin signal is associated with focal adhesions, it means that focal adhesions are mostly found on the peaks of wrinkles. Therefore, the cell membrane is mostly flat and cannot reach the trough of wrinkles (Figure 4.3c). On the other hand, substrates with a wavelength of $\lambda = 3.7\,\mu m$ (Figure 4.3d) and $\lambda = 6.3\,\mu m$ (Figure 4.3e) result in a vinculin signal in troughs and peaks. Consequently, the cell membrane bends to follow the undulation of the substrate as schematically shown in Figure 4.3f. Intriguingly, the fluorescence signal in the troughs seems to be lower compared to the signal on peaks.

4.4 Dynamic cell spreading on wrinkles

Live cell imaging was performed on C2C12 cells right after seeding on the wrinkled substrates. The cells were previously tranfected with LifeAct-GFP to visualize the cell shape and the actin cytoskeleton by fluorescence microscopy. In Figure 4.4a the actin filaments of one cell are shown at different time points after seeding on $\lambda = 1.7\,\mu m$. Right after seeding, the cell displays a circular shape with isotropic actin orientation. Afterwards, the cell elongates for ca. 3 h in wrinkle direction and develops an ordered actin cytoskeleton. After 3 h the cell shape reaches an equilibrium state without significant changes. Figure 4.4b shows the aspect ratio AR of the cell (red triangles) and the nematic order parameter of actin $\langle S_{\mathrm{actin}} \rangle$ (black circles) plotted against time t. Notably, within the first 3 h the change of AR over time is almost linear while $\langle S_{\mathrm{actin}} \rangle$ can be fitted well with an exponential function. From the fit, the characteristic relaxation time was determined to be $\tau \approx 37 \pm 4\,\mathrm{min}$. In Figure 4.4c the relationship between AR and $\langle S_{\mathrm{actin}} \rangle$ is plotted for the whole duration of the experiment. The behavior of this correlation can be roughly separated into three parts: from $t = 0 - 1.5\,\mathrm{h}$ (purple) the AR increases

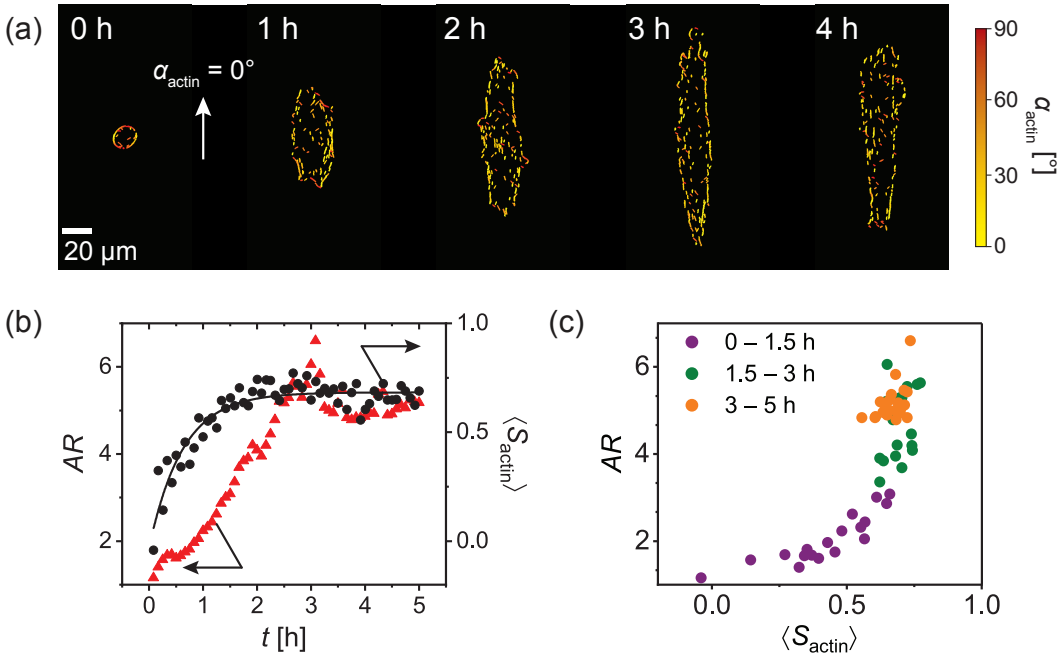

Figure 4.4: Spreading of a cell on wrinkled substrate. (a) The actin filaments of one C2C12 cell are shown at several time points after seeding on $\lambda = 1.7\,\mu m$. The color in the images represents the angle α_{actin} of actin filaments with respect to the wrinkle direction (white arrow). The thickness of actin filaments was increased by 2 pixel to improve visibility. (b) Aspect ratio AR (red triangles) and nematic order parameter of actin $\langle S_{actin} \rangle$ (black circles) are plotted against time t. (c) AR is plotted against $\langle S_{actin} \rangle$. Within the first 1.5 h there is a positive correlation between both values (purple). Afterwards the AR increases ($t = 1.5 - 3\,h$, green) and reaches a saturation after 3 h (orange).

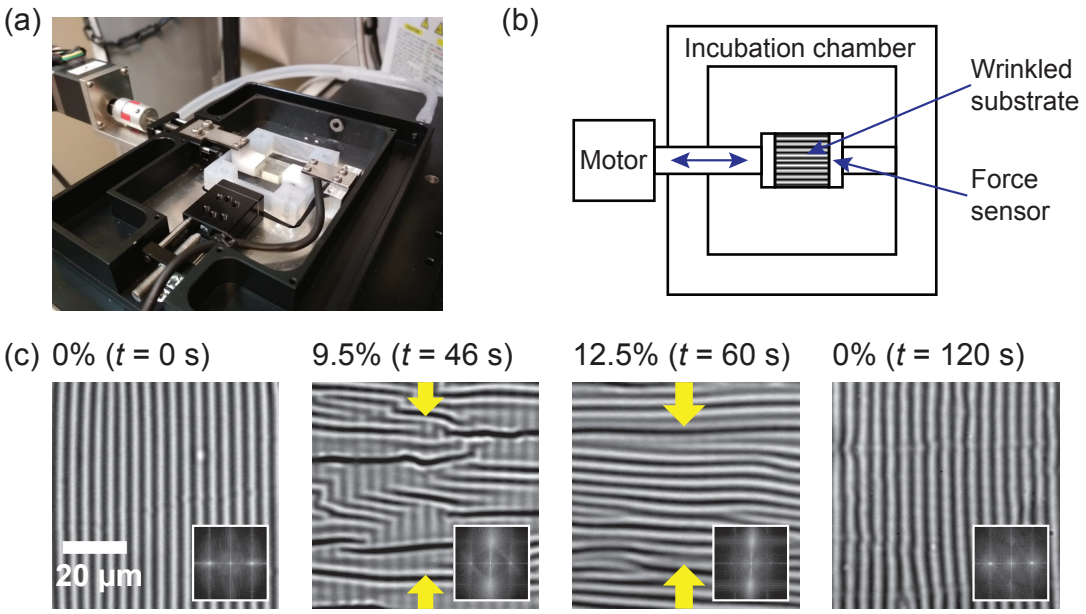

Figure 4.5: (a) Picture of the motorized pusher which was built specifically for live cell imaging. The motor speed and percentage of strain can be controlled. For this study a speed of $v = 25\,\mu m/s$ was applied. (b) Scheme of the experimental setup. (c) DIC images were acquired at different time points and strain levels. Yellow arrows indicate the direction of strain. The inset shows the Fourier transform of the DIC images.

slowly with a fast growing $\langle S_{\text{actin}} \rangle$. Afterwards, $\langle S_{\text{actin}} \rangle$ reaches a saturation at ≈ 0.7 while AR continues to grow (green). Finally, after 3 h (orange) both values reach the saturation without further significant changes.

The same experiment was performed on a smaller wavelength $\lambda = 1.7\,\mu m$ and on flat polyimide. With $\lambda = 1.7\,\mu m$ the correlation between AR and $\langle S_{\text{actin}} \rangle$ was linear throughout the whole experiment and the cell reached an equilibrium state after $t = 3\,h$ (Appendix A.1). On flat polyimide, C2C12 cells spread isotropically with almost constant $AR \approx 1$ and $\langle S_{\text{actin}} \rangle \approx 0$ within over 4 h after seeding (Appendix A.2).

4.5 Cellular response to dynamic change in wrinkle orientation

The goal of the following experiment was to analyze the cell response, especially morphology and nematic order parameter of actin, to a dynamic change of topography. The wrinkled substrates were previously shown to change the orientation of wrinkles by 90° upon compression.[39] For this purpose, a custom motorized pusher was built as shown in Figure 4.5a. The pusher is mounted on the stage of a confocal microscope and can adjust the speed of compression and the level of applied strain in a precise manner. Viewed from the top, Figure 4.5b shows schematically the experimental setup. In Figure 4.5c differential interference contrast (DIC) microscopy images of one wrinkled substrate are displayed at different time points and different strain levels. The motor speed was set constant at $v = 25\,\mu m/s$. In the insets the 2D Fourier transform of each image is shown. Without any axial strain (0 %) the alignment of wrinkles is parallel. The accurate wavelength λ was calculated from the Fourier transform by measuring the distance of the first maximum (bright spot) from the center which results in a real-space characteristic distance of $\lambda = 3.9\,\mu m$. At a strain level of 9.5 percent the periodic topography is broken by locally appearing wrinkles in perpendicular direction. Complete rearrangement of the wrinkles is achieved after 60 s at 12.5 % strain. At this point the orientation of wrinkles and the image in Fourier space are rotated by 90°. The latter yields a characteristic wavelength of 4.0 µm. The strain was then released with the same velocity of $v = 25\,\mu m/s$ which resulted in recovery of the original topography at $\lambda = 4.1\,\mu m$. Optimization of the protocol, especially regarding plasma treatment of PDMS, resulted in increased stability of bonding between polyimide and PDMS. The reversible switching of the topography is applied to examine the dynamic change of cell morphology and nematic order parameter of actin.

Cell were observed over time on the wrinkled substrate with a wavelength of $\lambda = 3.7\,\mu m$ until they reached an equilibrium state. Then, the wrinkle orientation

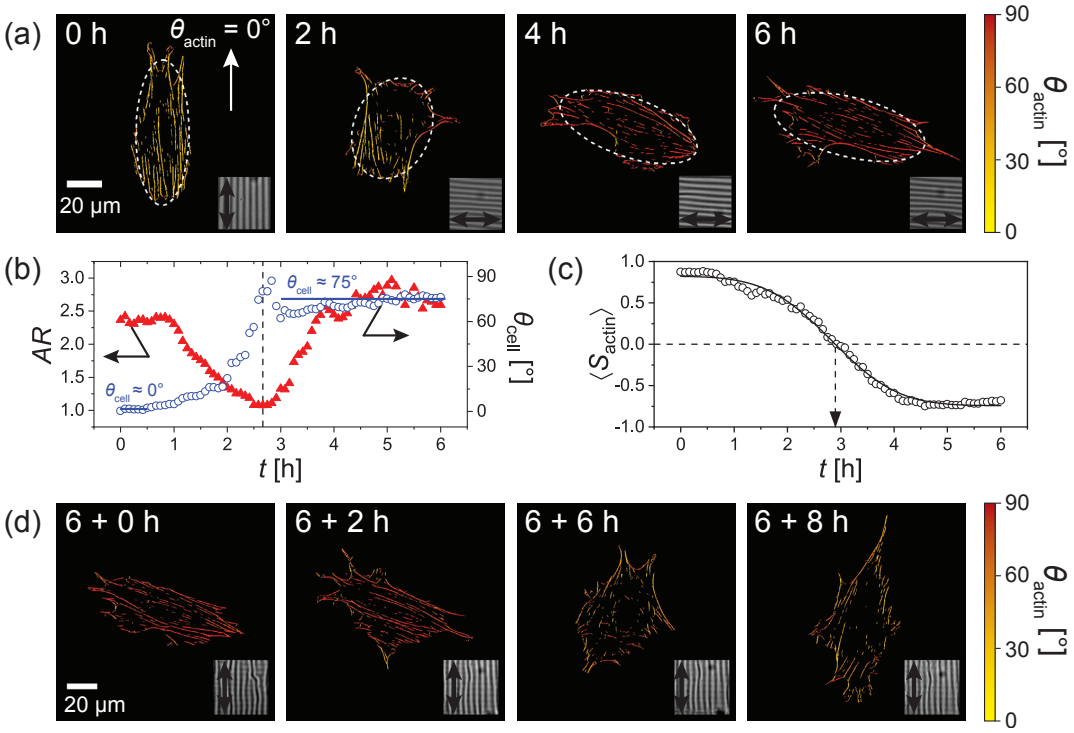

Figure 4.6: (a) Transected C2C12 cell responds to the change in wrinkle direction at a wavelength of $\lambda = 3.7\,\mu m$. The color code refers to the angle α_{actin} between original wrinkle orientation (white arrow) and the actin filaments. The dotted white ellipse was fitted to the cell shape to extract the aspect ratio AR and the angle of cell orientation θ_{cell} with respect to the wrinkle orientation. In the inset the wrinkle pattern is shown with the black arrow pointing in the current wrinkle direction. Strain was applied at $t = 0\,h$ and increased to 12.5 % within 60 s. After 6 h the cell shape and actin ordering reached a steady state. (b) The aspect ratio AR (red triangles) and angle θ_{cell} (blue circles) of the cell are plotted over time t. A transition time point was observed and defined as the minimum of AR at $t^*_{AR,3.7\,\mu m} = 2.8\,h$. Note that θ_{cell} is always calculated with respect to the original wrinkle direction. (c) The neamtic order parameter of actin $\langle S_{actin} \rangle$ is plotted against time t. The data can be fitted well with an error function with the critical time point $t^*_{actin,2.8\,\mu m} = 2.8\,h$ defined by $\langle S_{actin} \rangle = 0$. (d) After 6 h the strain is relaxed and the substrate recovers the original confirmation. The color code is identical to (a). It can be seen that the cell shape and actin ordering are reversible.

was switched by 90° within 60 s as shown in Figure 4.5. The time point at which the compression of the substrate started was defined as $t = 0\,\mathrm{h}$. Figure 4.6a shows the actin filaments of one example cell with the color code indicating the angle α_{actin} between individual filaments and the original wrinkle direction (white arrow). An ellipse was fitted to the cell shape (dotted white line). The cell angle θ_{cell} is measured between the ellipse major axis and the original wrinkle direction. In the inset, the current wrinkle direction is shown. In Figure 4.6b the aspect ratio AR (red triangles) and cell angle θ_{cell} (blue circles) are plotted against time t. The symbol θ is chosen to describe the angle during a dynamic change of topography in contrast to α which is used only for static topography. In this experiment, the initial wrinkle direction is $\theta_{\mathrm{cell}} = 0°$ which changes to $\theta = 90°$ when strain is applied.

With a delay of ca. 1 h after change of wrinkle orientation, the AR decreases sharply from $AR_0 = 2.4$ and reaches a minimum of $AR_{\mathrm{min}} = 1.1$ which is defined as the critical time point $t^*_{\mathrm{AR},3.7\,\mu\mathrm{m}}$. The low AR indicates an almost round shape of the cell. During the decrease of AR the cell angle θ_{cell} increases from $\approx 0°$ to $\approx 75°$ after $t^*_{\theta,3.7\,\mu\mathrm{m}} \approx 3\,\mathrm{h}$ (Figure 4.6b). The apparent synchronization between $t^*_{\mathrm{AR},3.7\,\mu\mathrm{m}}$ and $t^*_{\theta,3.7\,\mu\mathrm{m}}$ was confirmed by observation of other cells by DIC microscopy (Appendix A.3). It should be noted that the change in cell morphology and orientation are induced by the topography and not by the strain of the substrate. While the latter can induce similar changes, it takes much longer for cells to respond. Steward *et al.* observed the change in cell morphology and orientation on flat PDMS in response to a strain of 20 % which resulted in a characteristic response time of 24 h.[163]

Additionally to the external properties like cell morphology and orientation, the internal ordering of the cell was assessed by the nematic order parameter of actin. In Figure 4.6c, the order parameter $\langle S_{\mathrm{actin}} \rangle$ is plotted against time t which is calculated by Equation 4.2. Since the angle of each actin filament is measured with respect to the original wrinkle direction, $\langle S_{\mathrm{actin}} \rangle = 1$ means perfectly parallel alignment and $\langle S_{\mathrm{actin}} \rangle = -1$ means perpendicular alignment with the original

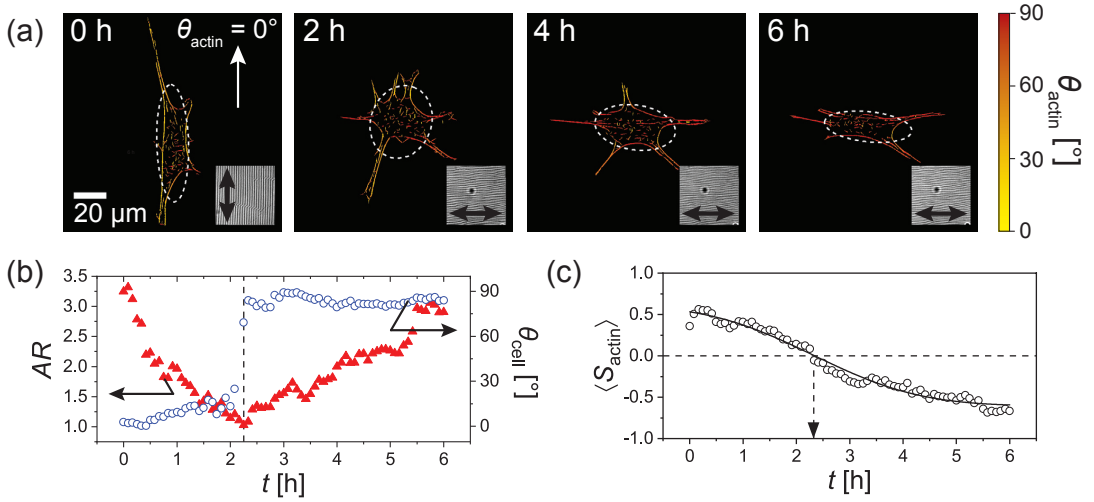

Figure 4.7: (a) Transected C2C12 cell responds to the change in wrinkle direction at a wavelength of $\lambda = 1.7\,\mu m$. (b) The aspect ratio AR (red triangles) and angle θ_{cell} (blue circles) of the cell are plotted over time t. (c) The nematic order parameter of actin $\langle S_{actin} \rangle$ is plotted against time t. The data can be fitted well with an error function (black line).

wrinkle direction. As shown in the plot, $\langle S_{actin} \rangle$ decreased monotonically from 0.9 to -0.7 after the wrinkle direction was changed by 90° and could be fitted well with an error function (black line). The transition time was defined as the time point when $\langle S_{actin,fit} \rangle = 0$ and resulted in $t^*_{actin,3.7\,\mu m} \approx 2.8\,h$. Intriguingly, this transition time was in good agreement with the previously revealed transition times $t^*_{actin,3.7\,\mu m} \approx t^*_{AR,3.7\,\mu m} \approx t^*_{\theta,3.7\,\mu m} \approx 2.8\,h$ indicating that the intrinsic (cytoskeleton) and extrinsic (morphology) orientation in the cell was synchronized. To confirm the reversibility of the cell and actin organization, the stress was released after 6 h so that the wrinkle topography returned to the original confirmation. As a response, the cell also recovered its previous orientation (Figure 4.6d).

4.6 Impact of wrinkle wavelength

Since a different behavior of the cell adhesion was found in Figure 4.2 for small ($\lambda = 1.7 - 2.5\,\mu m$) and large wavelengths ($\lambda = 3.7 - 6.3\,\mu m$), the dynamic adaptation to the change in topography could also behave differently depending on the wavelength. To test this hypothesis, a cell was observed over time on $\lambda = 1.7\,\mu m$

after the change of wrinkle direction (Figure 4.7a). Similar to Figure 4.6a, the cell was first incubated until it reached an equilibrium and the wrinkle orientation was switched by 90° by slowly increasing the strain over 60 s. As shown in Figure 4.7b, the AR decreased immediately from the initial value of $AR_0 = 3.3$ until it reached the minimum at $t^*_{\mathrm{AR},1.7\,\mu\mathrm{m}} \approx 2.3\,\mathrm{h}$. At this time, the cell exhibited a more spiky morphology compared to the cell on $\lambda = 3.7\,\mu\mathrm{m}$ (Figure 4.6a). The angle of the cell θ_{cell} changed rapidly from $\approx 0°$ to $\approx 90°$ at $t^*_{\theta,1.7\,\mu\mathrm{m}} \approx 2.3\,\mathrm{h}$, agreeing well with the transition time of the AR. The general consistency of this behavior was confirmed with DIC images of other cells (Appendix A.4). The plot in Figure 4.7c shows the nematic order parameter $\langle S_{\mathrm{actin}} \rangle$ which decreases monotonically over time from 0.6 to -0.6. The fit with an error function (black line) reveals a transition time of $t^*_{\mathrm{actin},1.7\,\mu\mathrm{m}} \approx 2.2\,\mathrm{h}$ which also agrees well with the previous transition times: $t^*_{\mathrm{actin},1.7\,\mu\mathrm{m}} \approx t^*_{\mathrm{AR},1.7\,\mu\mathrm{m}} \approx t^*_{\theta,1.7\,\mu\mathrm{m}} \approx 2.3\,\mathrm{h}$.

4.7 Discussion

As shown in Figure 4.2, seeding of C2C12 on a topography with different wavelengths λ resulted in different cell and actin ordering as well as cell morphology. The angle α_{cell} was measured between the major axis of cells and the orientation of the wrinkle topography. On small $\lambda = 1.7\,\mu\text{m}$ the distribution of α_{cell} was relatively broad, i.e. it showed a large FWHM, which decreased with increasing λ (Figure 4.2b). Therefore the cells are more aligned on substrates with larger λ. In a previous study[162] using PDMS substrates with periodic waves or grooves, the angle of bovine capillary endothelial cells has been measured. They suggested that the cell angle decreases with an increase in λ: $\theta = 20 \pm 3°$ at $\lambda = 5\,\mu\text{m}$ and $\theta = 14 \pm 4°$ at $\lambda = 10\,\mu\text{m}$.[162] θ was calculated in this case as the average value of all cell-wrinkle angles, where $\theta = 0°$ is defined as optimal alignment and $\theta = 45°$ is defined as random alignment. Another study introduced the cell orientation index (COI) which was used for substrates with submicrometer-scale features.[164] This index is defined as $\text{COI} = 1 - \theta/45$. Since the information about the wrinkle distribution is missing, a direct comparison with the nematic order parameter was not possible. Other studies presented a percentage of aligned versus non-aligned cells and actin cytoskeletons. They found that the alignment on substrates with ridges with $1 - 5\,\mu\text{m}$ wide features was more pronounced compared to substrates with larger features[5,8,165]. However, the threshold of aligned and non-aligned cells, was not clearly defined.

Commonly, cells in anisotropic biological environments not only align, but also elongate along the axis of the anisotropic feature. This behavior is emulated with substrates using the periodic topography. For example, bovine capillary endothelial cells feature an aspect ratio of 2.5 on flat substrates. The aspect ratio increases to 2.9 on periodic waves at $\lambda = 5\,\mu\text{m}$ and became 3.2 at $\lambda = 10\,\mu\text{m}$.[162] While this behavior was most frequently observed, some studies also found a decrease in the alignment with an increase in the lateral dimension of the substrate features, for example in the case of mesenchymal stem cells on ridges and

grooves.[166] The elongation and orientation of cells were both taken into account by the calculation of the nematic order parameter $\langle S_{\text{cell}} \rangle$ and weighing the distribution of $\cos(2\alpha_{\text{cell}})$ with the aspect ratio AR of cells (Equation 4.1. After increasing the wavelength from $\lambda = 2.5$ to 3.7 µm a saturation of the order parameter was found ($\langle S_{\text{cell}} \rangle \approx 0.9$). This indicates that there is a critical wavelength λ^*, which distinguishes the aligned from the non-aligned state. Observation of the actin angle α_{actin} revealed a larger distribution of α_{actin} (Figure 4.2e) compared to the cell orientation (Figure 4.2b). However, when calculating the nematic order parameter $\langle S_{\text{actin}} \rangle$, it was clearly distinct from the isotropic ordering of the actin cytoskeleton on flat substrates (Appendix A.2). Increasing the wavelength from $\lambda = 2.5$ to 3.7 µm resulted in a saturation of $\langle S_{\text{actin}} \rangle \approx 0.7$ (Figure 4.2f). This indicates that there is a common critical wavelength λ^* for the cell orientation and actin ordering, despite the hierarchical differences.

It is well known, that the formation of actin stress fibers is induced by the mechanosensory signals of focal adhesions.[15] Therefore, the location of focal adhesions was determined by immunofluorescence labeling of vinculin (Figure 4.3). It was found, that focal adhesions are elongated in wrinkle direction for all wavelengths. Remarkably, the location of focal adhesions differed significantly depending of the critical wavelength λ^*. At $\lambda < \lambda^*$ (Figure 4.2a,b) focal adhesions are located at the peaks of wrinkles, but not in the troughs. Therefore, the bottom membrane of the cell must be flat and only in contact with wrinkle peaks as well. At $\lambda > \lambda^*$ the focal adhesions are located at peaks and in troughs (Figure 4.3d,e), indicating that the cell membrane bends according to the wrinkle profile.

Physically, the difference in location of the focal adhesions depends on the counterplay of two energies: the adhesion free energy F_{adh} and the bending energy F_{bend}. The height profile of wrinkles is defined as $h(x, y) = \frac{\Delta h}{2} \sin\left(\frac{2\pi}{\lambda} x\right)$, where the x-axis is perpendicular and the y-axis is parallel to the wrinkle direction. Assuming, the cell membrane completely follows the wrinkle undulation (full adhesion, Figure 4.3c), the total free energy is simply the sum of all energies: $F_{\text{full}} = -F_{\text{adh}} + F_{\text{bend}}$. In the case that the focal adhesions are only at the wrin-

kle peaks and the cell membrane is flat (partial adhesion, Figure 4.3c), a factor $0 < \chi < 1$ is introduced which defines the fraction of the contact area between cell and substrate. In this case, the total free energy is calculated as follows: $F_{\text{full}} = -\chi F_{\text{adh}}$. The difference in free adhesion between full and partial adhesion is therefore calculated as follows:

$$\Delta F = -(1-\chi)F_{\text{adh}} + F_{\text{bend}} \, . \tag{4.3}$$

In the literature, the bending energy of a membrane is defined as follows:[15,167]

$$F_{\text{bend}} \cdot A = \int \frac{1}{2}\kappa(C_x + C_y - 2C_0)^2 dA \, . \tag{4.4}$$

Here, κ is the bending modulus of the cell membrane and C is the contact curvature. In case of the wrinkled substrate, C_y and the spontaneous curvature C_0 are zero. Since the wrinkle topography is periodic, it makes sense to calculate the bending energy per unit area $A = L \times 1$ where L is the contour length corresponding to one wavelength and 1 is the unit length along the x-axis. Inserting this into Equation 4.4 results in the following relations:

$$F_{\text{bend}} = f_1(\tfrac{\Delta h}{\lambda})\frac{\kappa}{\lambda L} \tag{4.5}$$

$$L = f_2(\tfrac{\Delta h}{\lambda})\lambda \, . \tag{4.6}$$

f_1 and f_2 are functions depending on the amplitude Δh and wavelength λ of the wrinkles whose complete forms are written in the Appendix A.6. The fraction $\frac{\Delta h}{\lambda}$ was almost constant in this study at $\frac{\Delta h}{\lambda} \approx 0.13$. Using Equation 4.3 results in the following relation for the critical wavelength:

$$\lambda^* = \sqrt{\frac{f_1\left(\frac{\Delta h}{\lambda}\right)\kappa}{(1-\chi)f_2\left(\frac{\Delta h}{\lambda}\right)F_{\text{adh}}}} \, . \tag{4.7}$$

Using the literature values for $F_{\text{adh}} \approx 10^{-7}$ to $10 \times 10^{-5}\,\text{J/m}^2$ [168,169] and $\kappa \approx 10 \times 10^{-19}\,\text{J}$,[168,170] and inserting the characteristic wavelength from this study

($2.5\,\mu m < \lambda^* < 3.7\,\mu m$) results in the fraction of adhesion area in the following interval: $0.77 < \chi < 1$. Apparently, the omission of the bending energy in the case of partial adhesion could result in large values for χ. The transition of adhesion depending on λ^* shares some common features with the wetting transition depending on the healing length.[171] Further details of the calculation are added in the appendix.

Some studies have suggested a characteristic length scale for the localization of focal adhesions. Human fibroblasts and vascular endothelial cells were able to form focal adhesions on 2 µm wide ridges, but not on 2 µm wide grooves. At a width of 10 µm, focal adhesions cound be found on ridges and groves alike,[20] indicating a characteristic mean distance between focal adhesions of 4 to 20 µm. In another study, Ray *et al.* seeded breast cancer cells on substrates with ridges and grooves of equal width between $0.4 - 1.2\,\mu m$. They found focal adhesions only on ridges with a width of 0.4 µm, but not on ridges and grooves which were 0.8 µm wide.[164] Therefore, the characteristic distance between focal adhesions is $0.8 - 1.6\,\mu m$. In this thesis, a characteristic wavelength was found at $\lambda^* = 2.5 - 3.7\,\mu m$ which seems to be in good agreement with the previous reports regarding the order of magnitude. The lower characteristic repeat distance for breast cancer cells can be attributed to the higher deformability of these cells. This is reasonable, because cancer cells are generally more deformable compared to normal myoblasts, fibroblasts, and vascular endothelial cells.[172] A study by Kim *et al.* observed that cardiac cells are able to enter 400 nm wide grooves,[173] which can be explained by the elasticity of cells. Cardiac muscle cells typically exhibit a Young's modulus of 0.5 kPa,[174] which is much lower compared to C2C12 cells ($12 - 15\,kPa$).[175]

Until now, most studies focused on the morphology and alignment of cells on static substrates, namely flat compared to wrinkled substrates or ridges and grooves on which the cells have reached a steady state.[28,162,176] Formerly, the only way to observe the dynamics of cytoskeleton remodeling was by fixation and staining of actin[177] and microtubules[178] *ex situ* at different time points. In this study, live cell imaging of C2C12 cells was performed using LifeAct-GFP and the actin

dynamics were observed *in situ* (Figure 4.4a). Shortly after adhesion the cells exhibited an initially round shape and started to elongate in the wrinkle direction. The actin cytoskeleton also organized itself primarily in the same direction. In Figure 4.4b the development of cell shape (AR) and nematic order parameter of actin ($\langle S_{\text{actin}} \rangle$) were plotted over time and both quantities reached a saturated level after 3 h. A positive correlation between AR and $\langle S_{\text{actin}} \rangle$ was observed in the initial phase of spreading. After $\langle S_{\text{actin}} \rangle$ reached the saturation, AR continued to increase (Figure 4.4c), indicating that the change in cell shape is guided by the actin cytoskeleton. On a substrate with lower wavelength ($\lambda = 1.7\,\mu\text{m}$) the correlation between AR and $\langle S_{\text{actin}} \rangle$ was sustained until both quantities reached the saturation level (Appendix A.1). In contrast, the cell spreading and actin cytoskeleton of cells on flat substrates was completely isotropic during the time of observation (Appendix A.2).

The wrinkled substrate has the unique ability to reversibly change the orientation of its topography by axial compression and relaxation (Figure 4.5). Other studies have applied several strategies to achieve similar features. For example, PDMS was treated by strong plasma exposure which hardened the surface. When strain is applied from the side, this substrate forms wrinkles with a wavelength of $\lambda = 6 - 7\,\mu\text{m}$, while the flat surface is recovered upon relaxation.[21] When C2C12 cells are seeded on these substrates the alignment was switched between random and parallel within 24 h upon formation and decomposition of the wrinkled surface. Another strategy is to embed magnetic microwires into polyacrylamide hydrogels. If a magnetic field is applied, these substrates induce a random roughness on the surface which recovers to a flat surface in the absence of the magnetic field.[22] In comparison to these studies, the substrate in this thesis offers the unique ability to switch the wrinkle orientation by 90° instead of returning to a flat surface (Figure 4.5). When strain was applied to the substrate with $\lambda = 3.7\,\mu\text{m}$, the AR of cells decreased first until it reached a minimum at $AR_{\text{min}} \approx 1$ (Figure 4.6b). Afterwards the AR increased while the cell angle was changed towards the new wrinkle orientation. The transition point was defined as the minimum of the AR

where the cell becomes almost spherical and resulted in $t^*_{\mathrm{AR},3.7\,\mu\mathrm{m}} = 2.8\,\mathrm{h}$. Roughly within the same time ($\approx 3\,\mathrm{h}$) the cell angle changed from $\approx 0°$ to $\approx 75°$. In another study, the change from aligned to isotropic ordering of adipose-derived stem cells after removal of the wrinkle pattern reached an equilibrium after $\approx 20\,\mathrm{h}$.[37] Here, the substrate consisted of a gold layer coated shape memory polymer. On PDMS wrinkles the response of C2C12 cell orientation was observed within $15 - 30\,\mathrm{h}$.[38] In this thesis, the response of C2C12 alignment to a dynamic change in substrate topography was significantly faster at about $t^* = 1 - 4\,\mathrm{h}$.

The actin cytoskeleton orientation switched its orientation by almost 90°, as shown by the $\langle S_{\mathrm{antin}} \rangle$ which decreased monotonically from 0.9 to -0.7 (Figure 4.6c). By fitting an error function, the transition time was defined as the point where the function equals zero and resulted in $t^*_{\mathrm{AR},3.7\,\mu\mathrm{m}} = t^*_{\mathrm{actin}} = 2.8\,\mathrm{h}$. This indicates, that the global orientation of cells and the sub-cellular ordering of actin filaments is mutually orchestrated. The reversibility of cell alignment was confirmed by release of the strain and return to the original substrate topography (Figure 4.6d).

Up to this point, the dynamic response of cells has only been observed above the proposed critical wavelength $3.7\,\mu\mathrm{m} > \lambda^*$ (Figure 4.6). Therefore, another sample with a wavelength $1.7\,\mu\mathrm{m} < \lambda^*$ was subjected to a similar experiment (Figure 4.7). The response of the cell was similar compared to the previous experiment: the AR first decreased and reached a minimum at $t^*_{\mathrm{AR},1.7\,\mu\mathrm{m}} \approx 2.3\,\mathrm{h}$. This was in good agreement with the transition of the nematic order parameter of actin at $t^*_{\mathrm{actin},1.7\,\mu\mathrm{m}} \approx 2.2\,\mathrm{h}$. Intriguingly, the cell shape appeared more spiky compared to the cell on $\lambda > \lambda^*$ (Figure 4.7a) which seems to be related to to the location of focal adhesions on $\lambda < \lambda^*$ which were shown to be only located at the peaks of wrinkles (Figure 4.3a,b). This means that the reorganization of the actin cytoskeleton occurred predominantly in the same plane. In contrast, on the substrates with $\lambda > \lambda^*$ the focal adhesions were found on wrinkle peaks and in troughs (Figure 4.3d,e), indicating that the actin cytoskeleton is reorganized in a three-dimensional space.

Until now, this is the first study which systematically presented the dynamic cell response to a reversible switching of wrinkle direction by 90°. Additionally, the influence of a characteristic wavelength and and the kinetics of contact guidance were studied. In principle, the wrinkled substrate used in this study is able to change the wrinkle direction by an arbitrary angle, as shown by Ohzono *et al.*[39] In the future, more studies on the influence of the wrinkle wavelength, direction of wrinkle modulation, and genetic modification of mechanosensing proteins[25] would help us to understand the interaction between extrinsic topographical cues and intrinsic genetic cues. Especially the differentiation of C2C12 cells into myotubes would be a suitable model system, since the formation of functional muscle fibers depends highly on cell alignment.[23]

5 Regulating stem cell functions and fate by dynamic substrate elasticity

The elasticity of the microenvironment of cells plays a major role in cellular processes such as adhesion, migration, differentiation and apoptosis.[4,43,48,69,179] Cells are able to respond to elastic cues by contraction of the actin-myosin network which inspired many studies to analyze active force generation in cells.[13,151,180,181] However, most studies observe the cell behavior on substrates with static elasticity even though biologic tissue is never static and alters its physical properties during development, aging and diseases. To provide such a dynamic system *in vitro*, this chapter focuses on a new material with the ability to change substrate elasticity on-demand and enables the analysis of *dynamic mechanosensing* during live cell microscopy.

5.1 Morphological phenotypes and remodeling of cytoskeletons

In a first step, the new substrate was characterized regarding its dimensions, elasticity, and dynamic behavior. Figure 5.1a shows two 3D-reconstructed images of the host-guest hydrogel (βCD–Ad gel (3,3)) acquired by a confocal microscope (Section 2.4.2). The bulk is shown in purple and the fibronectin coating is shown in green. Below the 3D images, two schemes show the chemical structure of the bulk material in the stiff (25 kPa, left) and soft (8 kPa, right) state. A cross-linking point is framed in red, which consists of a β-cyclodextrin and adamantane inclusion complex. In the stiff state most cross-linking points (red square) are closed. When

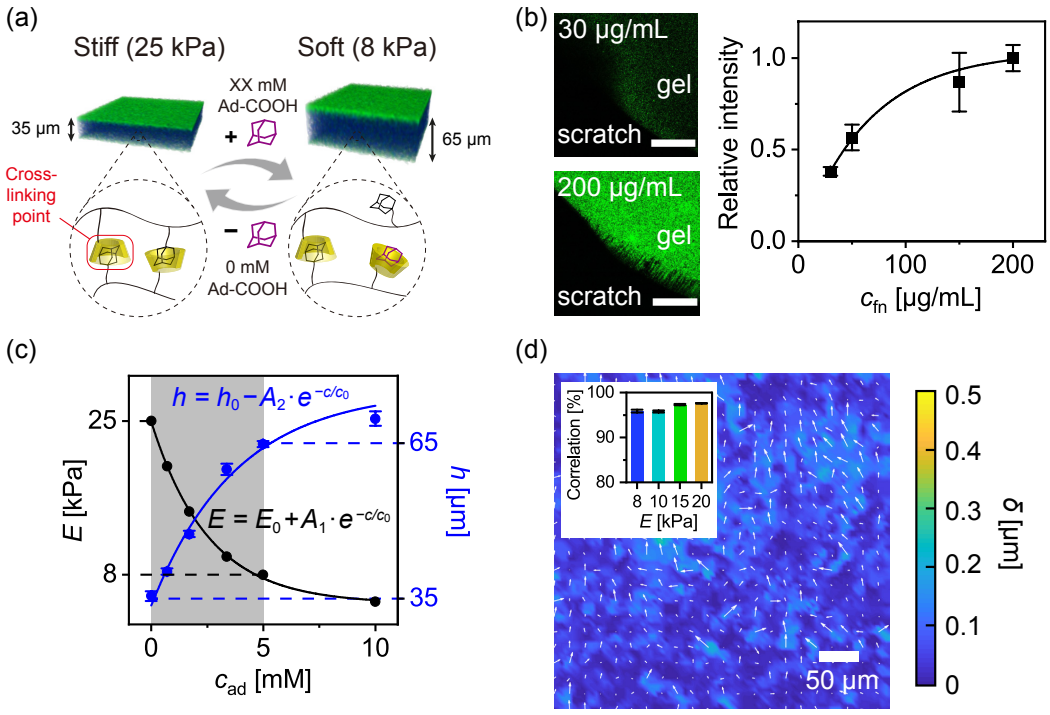

Figure 5.1: (a) Scheme of host-guest gel swelling. The image shows the bulk of the gel in purple and fibronectin coating in green. The dotted circles present a magnification of the bulk material which consists of polyacrylamide (black lines) and cross-linking points (red rectangle). These points are inclusion complexes of β-cyclodextrin (yellow cone) and adamantane (black cube). If adamantane-carboxylic acid (Ad-COOH) is added, the cross-linking points are opened partially (right dotted circle) resulting in swelling (from 35 µm to 65 µm) and softening of the gel (from $E = 25$ kPa to 8 kPa). (b) Maximum projected images show fluorescently labeled fibronectin in green close to a scratch in the gel (dark area). The concentration of fibronectin during coating was between 30 µg/mL (top image) and 200 µg/mL (bottom image). In the right panel the relative fluorescence intensity depending on coating density is plotted and fitted with an exponential function. (c) Elastic modulus E measured by AFM nano-indentation, and substrate height h measured by confocal microscopy, plotted as a function of [Ad-COOH]. Note that [Ad-COOH] $= 0 - 5$ mM (shaded in grey), corresponding corresponds to $E = 25 - 8$ kPa. (d) The lateral displacement δ of fluorescent beads embedded in the hydrogel after incubation with 5 mM Ad-COOH for 10 min. The magnitude of displacement is indicated by the color code, while the direction is indicated by the white arrows. The histogram in the inset represents the correlation of bead positions with the elasticity $E = 25$ kPa as reference. The change in bead position was negligible as the correlation remained above 95 % for all samples.

adamantane-carboxylic acid (Ad-COOH) is added, it blocks the β-cyclodextrin as shown in the right scheme. This results in swelling and softening of the hydrogel. In Figure 5.1b the fluorescence signal of the fibronectin coating on the surface of the host-guest hydrogel (left side) is shown. Fibronectin was covalently bound to the hydrogel surface by the photo-responsive crosslinker Sulfo-SANPAH. In the dark region of the images the hydrogel was removed to measure the background signal. Four different concentrations of fibronectin were tested between 30 µg/mL and 200 µg/mL. The plot on the right shows the relative fluorescence intensity of the samples which is fitted with an exponential function. To optimize cell adhesion, all following experiments were performed with 200 µg/mL fibronectin coating. Figure 5.1c shows the elastic modulus E and sample height h of the host-guest hydrogel, plotted as a function of Ad-COOH concentration [Ad-COOH]. While the elasticity was measured by atomic force microscopy (AFM, Section 2.4.1), the height was determined by the auto-fluorescence in confocal microscopy stacks, similar to Figure 5.1a. Changes in E were proportional to log[Ad-COOH] (solid line), reflecting the equilibrium between the chemical potential of Ad-COOH in solution and that in hydrogel. Prior to the experiments with hMSCs, the influence of Ad-COOH on cell viability was tested, which did not influence the viability of hMSCs up to [Ad-COOH] = 5 mM (Appendix B.1). Fluorescent beads were embedded in the substrate surface to measure the surface deformation during swelling. Figure 5.1d shows the displacement of beads after the elasticity was changed from 25 to 8 kPa. From the color code it can be seen that the average bead displacement remained below 0.2 µm. In the inset, the correlation between bead positions at different elasticities is shown with respect to $E = 25$ Pa as a reference. As the correlation is always >95 %, the deformation of the substrate surface is negligible.

Figure 5.2a and 5.2d represents two typical phase contrast microscopy images of hMSCs on stiff (25 kPa, [Ad-COOH] = 0 mM) and soft (8 kPa, [Ad-COOH] = 5 mM) hydrogels. As shown in the figure, the cell on a stiff substrate gripped the substrate by establishing clearly visible adhesions, while the cell on a soft substrate took an elongated shape. The color code in Figure 5.2b and 5.2e represents the

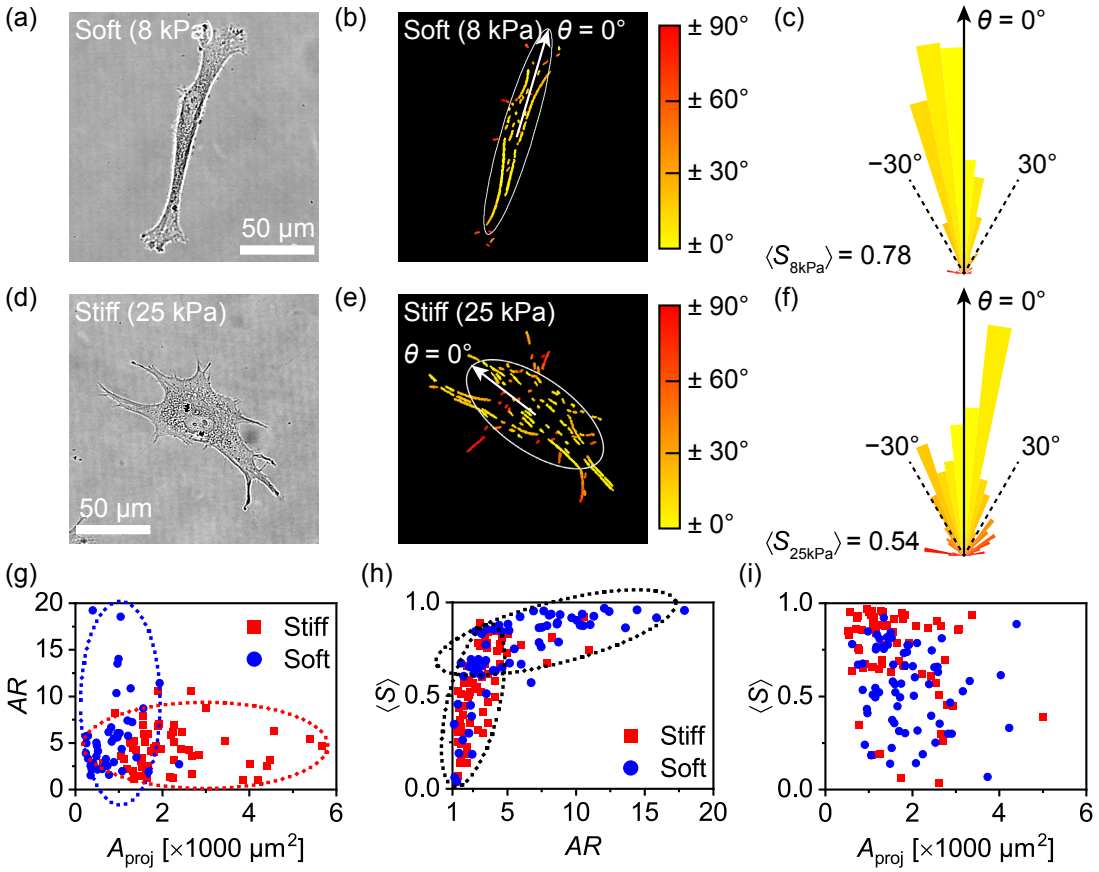

Figure 5.2: (a) Phase contrast image of a representative human mesenchymal stem cell (hMSC) on soft (8 kPa) supramolecular hydrogel. (b) Orientation of actin filaments with respect to $\theta = 0°$ corresponding to the cell's major axis defined by an ellipse fit. (c) Distribution of fluorescence intensity calculated from panel (b), yielding the weighed nematic order parameter, $\langle S_{8\,\mathrm{kPa}} \rangle = 0.78$. The corresponding data for hMSC on stiff (25 kPa) hydrogel are presented in panels (d) – (f). Physical (g) Cells on soft (blue) and stiff (red) substrates can be classified by using aspect ratio AR and projected area A. (h) Order parameter $\langle S \rangle$ vs. AR showed two different correlations independent of substrate stiffness, suggesting that the cell morphology correlates with actin ordering. (i) $\langle S \rangle$ vs. A_{proj} showed no correlation.

angles of individual actin filaments with respect to the major axis by taking the same cells as shown in Figure 5.2a and 5.2d. $\theta = 0°$ is defined by a white arrow in each panel. Figure 5.2c and 5.2f show the distribution of actin filament angles in the displayed cells. It can be seen that the distribution is broader for stiff gels. Using this data, the nematic order parameters of actin filaments[6,41] are extracted from two representative cells calculated by Equation 4.2 and suggested a clear difference in cytoskeletal arrangements. hMSCs on stiff substrates established several adhesions that are stabilized through the contractile forces generated by several stress fibers, $\langle S_{25\,\mathrm{kPa}} \rangle = 0.54$, while hMSCs on soft substrates are axially stretched and align actin filaments parallel to the major axis, $\langle S_{8\,\mathrm{kPa}} \rangle = 0.78$. Major and minor axes of each cell are defined by fitting the cell as an ellipse.

The morphological phenotype of hMSCs on stiff (red) and soft (blue) hydrogel substrates were classified by plotting the aspect ratio AR (the ratio of major and minor axes of a cell) versus the projected cell area A_{proj}, extracted from more than 40 cells (Figure 5.2g). As shown by ellipses in the figure, hMSCs on stiff substrates can be characterized by a larger cell area A_{proj} and a more isotropic shape and hence smaller AR, while hMSCs on soft substrates were smaller and more elongated. If one compares the order parameter $\langle S \rangle$ with AR (Figure 5.2h), cells show two different correlations independent of substrate stiffness. As indicated by the black ellipses, high order parameters ($\langle S \rangle > 0.7$) correlate with large aspect ratios ($AR = 2 - 18$) while cells with low order parameter ($\langle S \rangle = 0 - 0.7$) have also low aspect ratio ($AR = 1 - 5$). In addition to the morphological phenotyping, the remodeling of cytoskeletons was assessed quantitatively. In a previous study, pH responsive hydrogels were used, based on physically crosslinked blockcopolymer micelles, which showed that hMSCs take an isotropic shape on soft substrates and a spindle-like shape on stiff substrates.[6] The apparent difference in morphological phenotypes most likely depends on the mobility of extracellular matrix proteins. The surface of pH responsive hydrogels was coated with fibronectin by physisorption,[6,49] while the surface of supramolecular hydrogels is functionalized by covalent immobilization of fibronectin.[9]

5.2 Regulating cell adhesion by substrate elasticity

The significant modulation of morphology observed on substrates with different elasticity suggests that the strength of cell adhesion should also be modulated. In order to measure the adhesion strength of hMSCs quantitatively, it was determined by a laser-induced pressure-wave (Section 2.4.3).[49] This setup allows to determine the critical pressure for cell detachment in a non-invasive manner.[7,49,182] Figure 5.3a,b represents the binarized microscopy images of hMSCs on a substrate with $E = 15\,\mathrm{kPa}$ before (a) and after (b) the exposure to the pressure wave. The range at which the cavitation bubble could reach ($d \leqslant 511\,\mu\mathrm{m}$) is indicated by a red broken line, and the region ($\Delta d = 100\,\mu\mathrm{m}$) exposed to $P \approx 4\,\mathrm{MPa}$ is indicated by a yellow ring. In order to determine the accurate cavitation bubble size, a video with an ultra fast camera was acquired and the bubble radius was measured directly in the images (Appendix B.2). By counting the fraction of cells remaining on the surface χ within $\Delta d = 100\,\mu\mathrm{m}$ (Figure 5.3c), the critical pressure P^* of cell detachment is obtained by fitting the data with the adapted error function:

$$\chi(P) = 1 - \frac{1}{2}\left(\mathrm{erf}\left(\frac{P - P^*}{\sqrt{2}\,\sigma}\right) + 1\right), \tag{5.1}$$

where σ is the standard deviation, and P^* the critical pressure of cell detachment at which 50 % of the cells are detached.

The transition points, indicated by black circles connected by a broken line as presented in Figure 5.3c, coincide with the pressure at which the first derivative $\delta\chi/\delta P$ takes the minimum. Intriguingly, the transition pressure P^* exhibited a change between $E = 20$ and $25\,\mathrm{kPa}$. Moreover, the full width at half maximum (FWHM) of $\delta\chi/\delta P$ reflects the width of the transition. The monotonic decrease in FWHM with increasing E suggests that the binding/unbinding transition becomes sharper when the substrate becomes stiffer. The observed tendency is summarized in Figure 5.3e, representing P^* and FWHM plotted as a function of E.

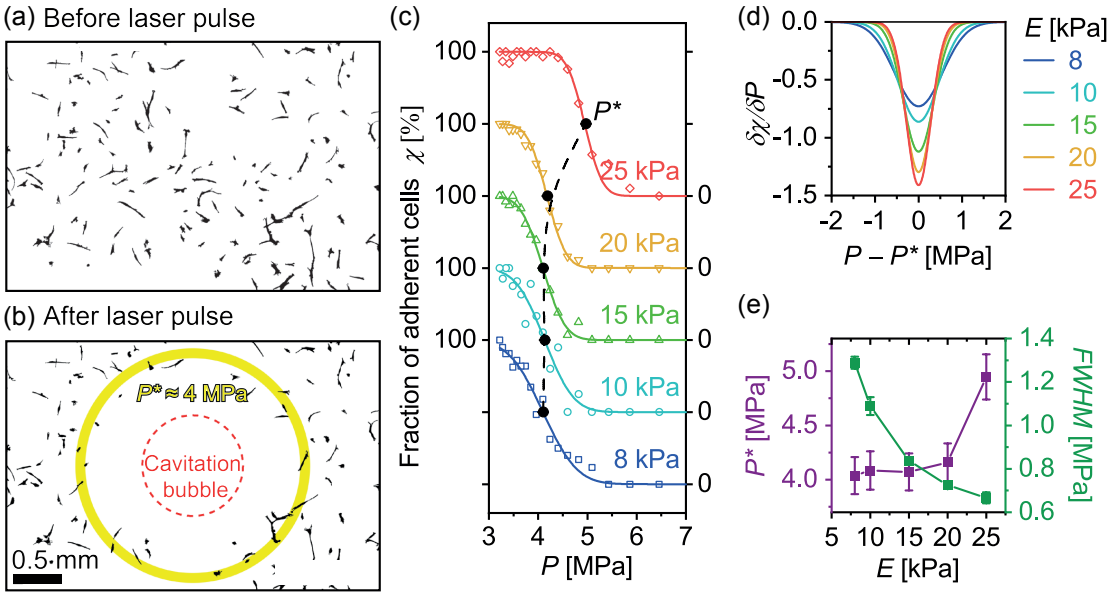

Figure 5.3: Binarized images of cells on a hydrogel substrate ($E = 15\,\mathrm{kPa}$) before (a) and after (b) the irradiation with a laser pulse. Size of the cavitation bubble is indicated by red broken line. The yellow belt corresponds to the region ($\Delta d = 100\,\mu\mathrm{m}$) exposed to $P \approx 4\,\mathrm{MPa}$. (c) Fractions of adherent cells χ on substrates with different stiffness E, plotted as a function of pressure P. The data points were fitted with the adapted error function. The critical pressures corresponding to the binding-unbinding transition P^* are indicated by black circles, connected by a black broken line. (d) Change in the width of transition evaluated from $\delta\chi/\delta P$. To compare different data sets, P was converted to $P - P^*$. (e) Effect of substrate elasticity E on the transition pressure P^* and the width ($FWHM$) of transition. The transition observed between 20 and 25 kPa suggests that the threshold elasticity for the mechanosensing of hMSCs is likely within this range.

5.3 Contractile forces exerted on elastic substrate by cells

Change in the cell adhesion strengths suggests the modulation of the contractile forces of cells exerted on substrates. To quantitatively determine the spatial pattern of forces generated by hMSCs, the traction stress of hMSCs that grip elastic substrates was measured by monitoring the displacement of fluorescent beads (diameter: 0.2 µm) embedded in the vicinity of substrate surfaces (Figure 5.4a). Figure 5.4b represents a typical traction stress field and the corresponding force dipoles M_{ij} as shown by equation 2.39. It is notable that the dipole matrix is symmetric and hence diagonalized because the net moment of inertia of the sys-

tem is negligible. This enables the calculation of major and minor eigenvectors possessing larger and smaller eigenvalues, $D_{\max}$ and $D_{\min}$, respectively. The mathematical background is explained more detailed in Section 2.4.4. In Figure 5.4b The directions of traction stress vectors are indicated by white arrows, while their magnitudes are shown by the length of arrows combined with the color scale. The inset is a zoom-up of the traction stress field near the cell periphery (red), implying that the large traction stresses pointing towards the cell center correspond to the contraction of acto-myosin stress fibers.

Using the traction stress $\vec{T}(\vec{r})$ and the particle displacement $\vec{u}(\vec{r})$, the total strain energy U is calculated (Equation 2.22).[150,151,183] This quantity coincides with the energy transferred from the cell to the substrate by elastic deformation. Here, the strain energy density was calculated within a region of interest close to the cell boundary to avoid possible artifacts at the field boundary which occur from the Fourier transform. As presented in Figure 5.4c, the total strain energy U exhibited a monotonic increase from 1 to 2 pJ with increasing substrate stiffness from $E = 8\,\text{kPa}$ to 25 kPa. The difference between soft substrates ($8 - 10\,\text{kPa}$) and stiff substrates (25 kPa) was significant ($p < 0.05$), but the transition seemed slow and progressive. Figure 5.4d represents the net contractile matrix μ, which can be obtained by the trace of diagonalized dipole matrix (Equation 2.40). Note that μ only includes the strains in direction of the principal axis of traction into consideration but excludes the rotational and translational strains. The net contractile strain μ also monotonically increased from $\mu = 1$ to 5 nJ according to the increase in substrate stiffness. Compared to the total strain energy (Figure 5.4c), the net contractile moment showed a sharper transition between $E = 20$ and 25 kPa. The distinct increase in the axial contraction μ (Figure 5.4d) and critical pressure for cell detachment P^* (Figure 5.3c) between $E = 20$ and 25 kPa suggest the presence of an elasticity threshold in the mechanosensing machinery of hMSCs (Appendix B.3). In Figure 5.4e μ is plotted against the aspect ratio AR of cells, where the aspect ratio AR and μ exhibit an anti-correlation behavior: If μ is large, the AR decreases and if μ is small, the AR increases.

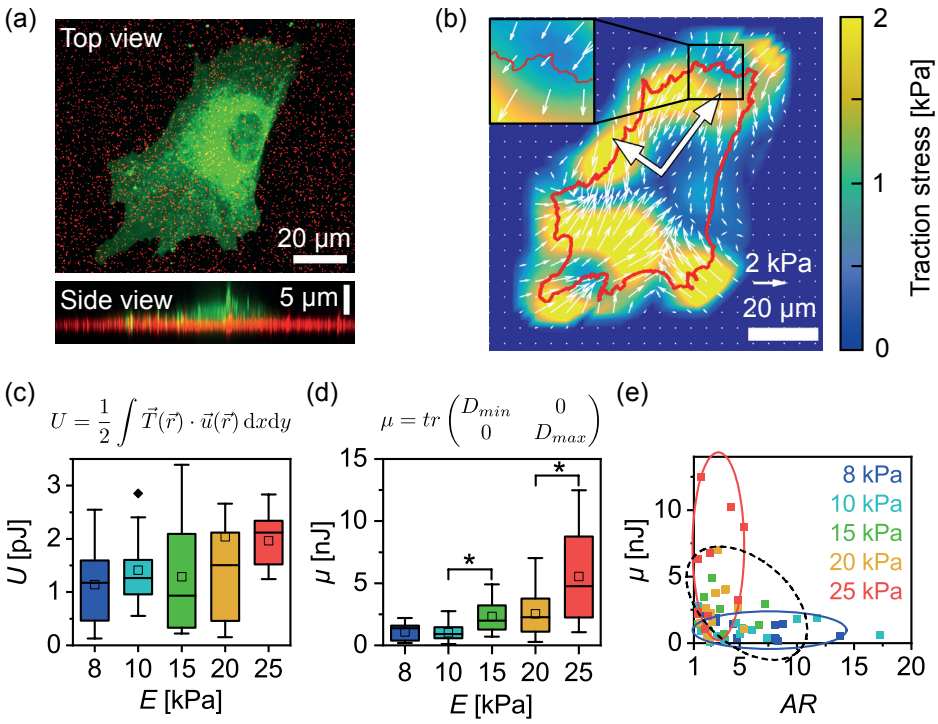

Figure 5.4: (a) Top (upper panel) and side (lower panel) views of hMSCs on a supramolecular hydrogel substrate ($E = 25\,\text{kPa}$) embedding fluorescent beads (diameter: $0.2\,\mu\text{m}$). The cell membrane was labeled with CellBrite™ (green). The side view confirmed that the beads (red) are confined in the close vicinity of the surface. (b) Traction stress field and the corresponding force dipoles extracted from hMSC on a substrate with $E = 25\,\text{kPa}$. The red line highlights the cell rim. White arrows show the direction of the traction stress, while the length of arrows and the color represent the magnitudes. The eigenvectors of force dipoles (D_{max} and D_{min}) are given as large white arrows. Inset shows the zoom-up image of stress field near the cell periphery. (c) Total strain energy U of hMSCs adherent on supramolecular hydrogels with different E. (d) Net contractile moment μ of hMSCs on substrates with different E. Each data set consists of the data from > 10 cells. The asterisk indicates a significant difference with a p-value of $p < 0.05$ by Student's t-test. (e) μ is plotted against the aspect ratio AR of cells. Groups of data are surrounded by ellipses in red for $E = 25\,\text{kPa}$, dashed black for $E = 10 - 20\,\text{kPa}$ and blue for $E = 8\,\text{kPa}$.

5.4 Cell response to dynamic mechanical stimuli

To simulate a dynamic stem cell niche, hMSCs were seeded on a stiff substrate ($E = 25\,\mathrm{kPa}$) and the elasticity was changed to soft ($E = 15\,\mathrm{kPa}$) without detaching the cells. Figure 5.5a shows fluorescence microscopy images of one representative cell before and after the change of elasticity. The green color indicates the cell membrane which was stained by CellBrite™ and the red color represents the fluorescent beads embedded in the substrate. Within the first 2 h the cell area and aspect ratio were almost constant, confirming that the cell was in a steady state. After switching the substrate elasticity from 25 kPa to 15 kPa, the adhesion area decreased notably and the cell shape became almost spherical. Using particle image velocimetry (PIV) and Fourier transform traction cytometry (FTTC) the force field exerted by the cell on the substrate surface was calculated (Section 2.4.4).

In Figure 5.5b the total strain energy U of the same cell is plotted over time t. On the substrate with 25 kPa (red squares) U maintained an almost constant level at $U \approx 2 - 2.5\,\mathrm{pJ}$ which decreased sharply to $U \approx 1 - 1.5\,\mathrm{pJ}$ when the elasticity is switched to 15 kPa. Afterwards, the strain energy remains constant for the observed time period. The average total strain energy and change in aspect ratio over time for five cells is shown in the Appendix B.4. In Figure 5.5c U is plotted against A_{proj} for four different cells. The data points of all observed time points are shown while data on $E = 25\,\mathrm{kPa}$ is plotted as open circles and $E = 15\,\mathrm{kPa}$ as filled triangles. Most cells exhibit two separate clusters of data points, indicating a distinctly different behavior depending on substrate elasticity. The linear fit (dashed line) was fitted to all data points and indicates a generally positive correlation between U and A_{proj} with a correlation coefficient of $r = 0.89$.

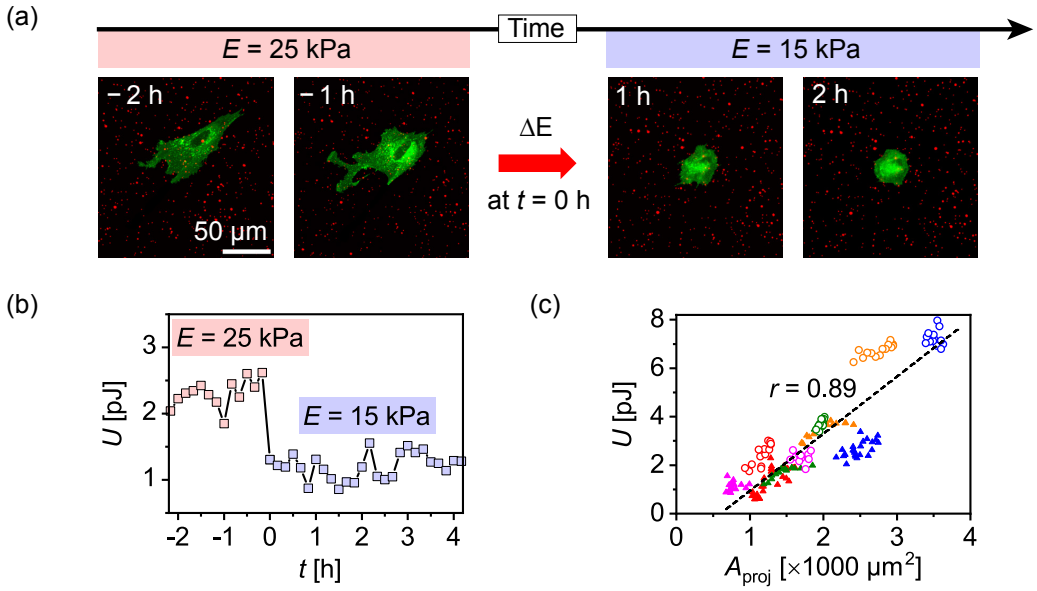

Figure 5.5: Response of a representative cell to a change in substrate elasticity from $E = 25$ to 15 kPa. (a) Fluorescence images of one representative cell at different time points. The cell membrane is stained with a non-toxic carbocyanine dye CellBrite™ 184 (green) and in the background the fluorescent beads embedded within the substrate surface are visible (red). After confirming that the cell reached a steady state, the elasticity was switched ($t = 0$ h) and the cell was further observed for 4 h while snapshots are taken every 10 min. The cell area decreases notably after the decrease in elasticity. (b) The total strain energy U of the same cell is plotted over time. At the time of switching ($t = 0$ h), U decreases promptly. (c) U is plotted against the projected cell area A_{proj} for 5 cells on 25 kPa (open circles) and 15 kPa (filled triangles). A linear function was fitted to the data (dashed line), indicating a positive correlation ($r = 0.89$).

5.5 Cell fate and proliferation regulated by mechanical stimuli

To investigate the effect of cyclic mechanical stimuli on cell proliferation and fate, the substrate elasticity was switched between 25 kPa (stiff) and 8 kPa (soft). First, the cells were pre-incubated on an elasticity of 25 kPa, then the elasticity was switched every $2, 4, 7, 10$ or 20 days. Since the cells were fixed 20 days after the pre-incubation, a period of $f^{-1} = 20$ indicates that the elasticity was constant for this sample. In Figure 5.6a snapshots of the cells are shown by phase contrast microscopy as a function of time t (x-axis) and inverse frequency f^{-1} (y-axis). It is notable that the cell number increases over time while the proliferation is inhibited at higher frequencies ($f^{-1} = 10 - 4$ days). In Figure 5.6b the cell density d after 20 days is plotted against the inverse frequency f^{-1} of mechanical stimulus. The mean and standard error were calculated from the individual cell densities in at least 20 randomly selected areas of $0.5\,\mathrm{mm}^2$. Evidently, the cell density decreased monotonically with an increase in mechanical stimuli. An error function (black line) was fitted to the data and the critical frequency $f^{*-1} = 8\,\mathrm{d}$ (dashed line) was defined as the inflection point of the error function ($\frac{d^2}{dx^2}\,\mathrm{erf}(x) = 0$).

After the exposure to mechanical stimuli for 20 days, the cells were fluorescently labeled with a STRO-1 antibody, i.e. a marker for mesenchymal stem cells. In Figure 5.6c a bar plot is shown where cells are categorized as STRO-1 positive (dark gray), intermediate (light gray), or negative (not shown). As a control, cells were incubated on glass substrates for the same time period and fixed at day 0 and day 20. The percentage p of STRO-1 positive cells in the control samples is indicated by the green bar (day 0, $p \approx 85\,\%$) and the red bar (day 20, $p \approx 7\,\%$). Compared to control samples, cells on host-guest gels maintained a much higher niveau of immunoreactivity to STRO-1, for example 25 % for $f^{-1} = 20\,\mathrm{d}$ and 75 % for $f^{-1} = 4\,\mathrm{d}$. It is notable, that a higher frequency of mechanical stimuli mostly resulted in a higher fraction of STRO-1 positive cells, indicating a positive correlation.

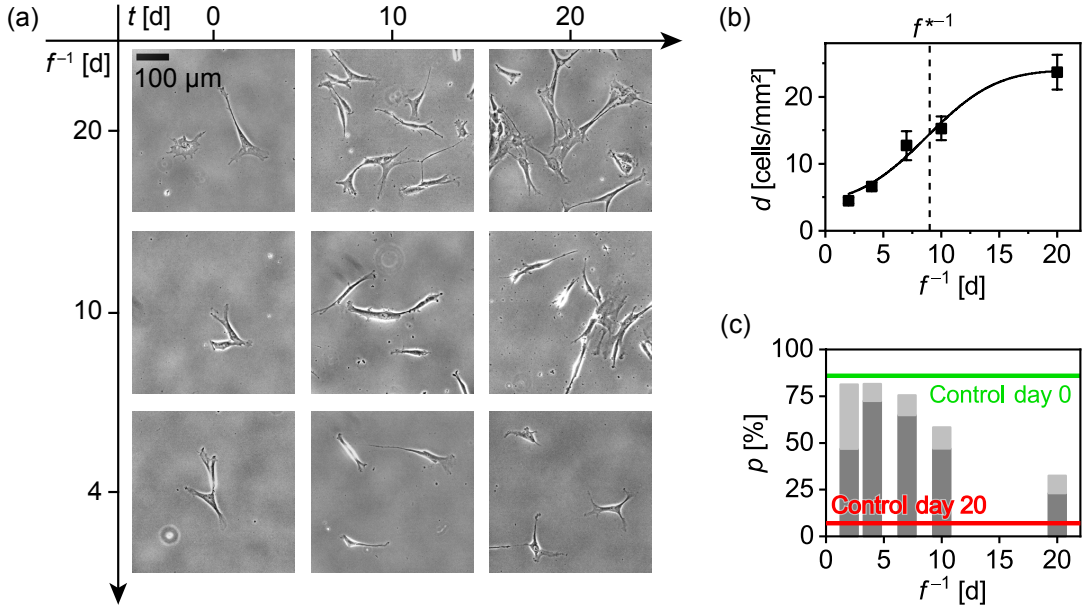

Figure 5.6: (a) Influence of periodic mechanical stress on cell density and stem cell marker expression. The substrate elasticity was switched repeatedly between 25 and 8 kPa with a frequency of $2, 4, 7, 10$ or 20 days. Representative phase contrast images are shown for 9 conditions with different time t (x-axis) and inverse frequency f^{-1} (y-axis). (b) The cell density d, measured after 20 days, is plotted against the inverse frequency of switching f^{-1}. Each data point corresponds to the mean and standard error calculated from $\geqslant 20$ randomly selected regions of interest ($0.5\,\mathrm{mm}^2$). A fit with an error function (black line) yields the critical inverse frequency $f^{*-1} = 8\,\mathrm{d}$. (c) Fraction of cells p showing positive (dark gray) and intermediate (light gray) immunoreactivity to STRO-1. Compared to the control level on plastic dishes showing a significant decrease in p from 85 % (green line) to 7 % (red line) in 20 d, hMSCs on hydrogel substrates showed higher immunoreactivity. Note that frequent switching of substrate stiffness at shorter periodicity $f^{-1} \leqslant 4\,\mathrm{d}$ resulted in the most efficient maintenance of STRO-1 level, $p \approx 80\,\%$.

5.6 Discussion

Human mesenchymal stem cells (hMSCs) were seeded on the supramolecular hydrogel where they showed significant differences in morphology and actin ordering (Figure 5.2a,d). The ordering of the actin cytoskeleton was analyzed by the nematic order parameter (Equation 4.2) which is calculated from the distribution of actin angles (Figure 5.2c,f). There have been several studies of hMSCs on polyacrylamide gels, observing the cell morphology depending on substrate elasticity. For instance, regarding the projected cell area (A_{proj}), hMSCs generally exhibit larger A_{proj} on stiffer gels.[185] Cell areas were reported between $1000\,\mu\mathrm{m}^2$ on gels with an elasticity below $1\,\mathrm{kPa}$[179,186] and up to $10\,000\,\mu\mathrm{m}^2$ at $E = 40\,\mathrm{kPa}$.[187] The results in this thesis are agree with these reports for with $A_{proj} = 500 - 2000\,\mu\mathrm{m}^2$ for $E = 8\,\mathrm{kPa}$ and $A_{proj} = 1000 - 6000\,\mu\mathrm{m}^2$ for $E = 25\,\mathrm{kPa}$ (Figure 5.2). Multiple studies have reported an increased aspect ratio (AR, sometimes called *spindle factor*) around a substrate elasticity of $E = 11\,\mathrm{kPa}$.[41,179] This is is confirmed here, since hMSCs on $E = 8\,\mathrm{kPa}$ showed a larger AR (≈ 6) compared to $E = 25\,\mathrm{kPa}$ (≈ 3).

The nematic order parameter of actin $\langle S \rangle$ in hMSCs was shown before to be positively correlated with the AR of cells.[41] Another study measured the nematic order parameter of fibroblasts on micropillars with different rigidity. They reported that even though the bending rigidity of micropillars is not directly comparable with that of a homogeneous gel, a difference in $\langle S \rangle$ was observed depending on pillar rigidity so that the ordering of the actin cytoskeleton was higher on stiff pillars ($\langle S \rangle = 0.7$) compared to soft pillars ($\langle S \rangle = 0.3$).[188] In addition to that, this study found two distinct groups of data with either low AR and a large variation in $0 < \langle S \rangle < 1$ or large $\langle S \rangle > 0.6$ and large variation in AR (Figure 5.2h). Intriguingly, these groups show only a very small area of overlap, in the high $\langle S \rangle$ and low AR regime, indicating a strongly distinct cell morphology depending on the two observed elasticities. Between $\langle S \rangle$ and A_{proj} no apparent correlation was observed. Note, that depending on the cell type, $\langle S \rangle$ can have different results, for

example C2C12 myoblasts exhibited a maximum order parameter of $\langle S \rangle = 0.4$ on $E = 40\,\mathrm{kPa}$, which reached almost 0, i.e. a perfectly isotropic state, on $E = 2\,\mathrm{kPa}$.

This study presents a unique method to determine the adhesion strength of cells by detachment with a pressure wave (Figure 5.3). In the past, several techniques have been developed to measure cell adhesion, for example pulling with an AFM cantilever,[139,189] moving and pulling of cells with an optical trap,[190] or detachment of cells by a laminar flow inside a flow chamber.[191,192] In comparison with these methods, the detachment assay in this study is able to analyze much higher numbers of cells in a short time compared to the single cell pulling with AFM or optical traps, and can induce much stronger pressures compared to the flow chamber, so that strong cell adhesions can be determined as well. Another strategy is to create the shock wave by focused ultrasonic waves using piezoceramics, which is called a *lithotripter*. Ohl *et al.* utilized this device to create pressure waves with similar pressure ($10 - 40\,\mathrm{MPa}$) compared to the setup in this thesis and detached HeLa cells from a plastic surface. They found that a shear stress of 160 Pa detaches 100 % of the HeLa cells.[193] Pressure waves induced by a focused laser beam have also been used to kill cancer cells, however, the critical pressure of detachment was not calculated.[194]

The result in this thesis show that the critical pressure of detachment $P^* = 4 - 5\,\mathrm{MPa}$ of hMSCs is in a similar range compared to other cell types, such as hematopoietic stem cells (HSC, $P^* = 3.2 - 7.0\,\mathrm{MPa}$)[7] and Osteosarcoma cells (U2OS, $P^* = 7.4 - 8.8\,\mathrm{MPa}$).[195] Surprisingly, the change in P^* was maximal between 20 and 25 kPa, indicating the existence of a critical elasticity separating between weak and strong adhesion states around $E = 25\,\mathrm{kPa}$. It should be noted, that cell detachment by flow chambers is not directly comparable with the laser pulse detachment, because the exposure time to the pressure is orders of magnitude different. In flow chambers the detachment of cells occurs gradually over time (for example, exposure to a shear stress of 8 Pa for 30 min)[10] while detachment by pressure waves is immediate (cavitation bubble life time is $\approx 100\,\mathrm{s}$, Appendix B.2).

Intriguingly, the distribution width of the fraction of adherent cells (FWHM) after applying laser pulse increased with decreasing elastic modulus E. The reason for this behavior is probably the different morphology of cells which depends on substrate stiffness. As cells get more elongated on softer substrates (Figure 5.2g and 5.4e), the force they experience during a pressure wave becomes more dependent on the orientation of the cell, thus creating a larger FWHM of the distribution of adherent cells after applying the laser pulse.

Traction force microscopy has been widely used to reveal the forces exerted by cells on their environment. These forces are generated by the cytoskeleton which regulates various cellular functions from proliferation to differentiation.[13,180] Even though traction forces have been measured extensively, many studies lack a quantitative analysis. In this study, the total strain energy U was calculated from the traction field by Equation 2.22 and showed a moderate increase with elastic modulus of the substrate (Figure 5.4c). On average, the total strain energy fluctuates around a value of $U \approx 1.5\,\mathrm{pJ}$. Other studies have calculated the strain energy for various cell types whose strain energy is usually in the same order of magnitude, for example aortic smooth muscle cells ($U = 0.21\,\mathrm{pJ}$),[150] human fibroblasts ($U = 3 - 2.3\,\mathrm{pJ}$)[196] or human liver cells ($U = 3\,\mathrm{pJ}$).[197] It is known that cells exert stronger forces on stiff substrates,[198,199] and also higher total strain energy,[196] which supports the positive trend between U and E that was found in this study. Alternatively, many studies focus on the net contractile moment μ which is more specific, considering the contractile forces along the major and minor axis of the cell. Other studies reported values of 3.3 pJ for aortic smooth muscle cells,[150] 10 pJ for fibroblasts[151] and $30 - 80\,\mathrm{pJ}$ for rat mesenchymal stem cells.[200] hMSCs in this study generated a much higher net contractile moment at $\mu = 1 - 5\,\mathrm{nJ}$ (Figure 5.4d) which can be explained by the larger cell area. While μ increased monotonically with the elastic modulus E, the largest increase occurred between 20 and 25 kPa. This indicates that the contractile response of hMSCs is especially sensitive around an elastic modulus of $E^* \approx 25\,\mathrm{kPa}$ and apparently correlates with the critical elasticity observed in the cell adhesion measurement.

Plotting μ against the cell aspect ratio AR (Figure 5.4a) reveals an anti-correlation: $E = 25\,\mathrm{kPa}$ results in large μ and small AR in contrast to $E = 8\,\mathrm{kPa}$ with small μ and large AR. This is in contrast to studies which suggested stronger traction forces in cells with elongated cell shape compared to the spherical morphology.[201] However, in the previous study the cell shape was regulated by microcontact printing at fixed elasticity, while in this study the cell is regulated by substrate elasticity. As a conclusion, the substrate elasticity seems to have a greater effect on cellular traction force compared to the cell shape.

Most *in vitro* studies are performed on static substrates, i.e. with fixed mechanical and biochemical properties. However, the stem cell niche and biological tissue in general are never static.[202,203] In this thesis, the cell response to a single change in substrate elasticity, from $E = 25\,\mathrm{kPa}$ to $15\,\mathrm{kPa}$ was investigated (Figure 5.5). An abrupt change in morphology (Figure 5.5a) and total strain energy (Figure 5.5b) was observed for four different cells (Appendix B.4). The values obtained for U are in good agreement with the static experiment (Figure 5.4c). A different study by Guvendiren *et al.* observed the projected cell area A_{proj} of hMSCs on hyaluronic acid gels while increasing the elasticity by delayed UV-crosslinking. They found, that hMSCs increase in A_{proj} over the course of 4 h when the elasticity is increased from 3 to 30 kPa.[61] Before and after the change in elasticity, A_{proj} was comparable to the average cell area on a substrate with the respective static elasticity. This indicates, that the response to an increase in E is much slower compared to the decrease in elasticity. A similar correlation was found by Hörning *et al.*, who measured the response of myoblasts to a dynamic change in elasticity. Here, the response to a decrease in E was delayed by $10 - 20\,\mathrm{min}$ and the response to an increase was delayed by 3 h. They suggested that the ability of cells to respond quickly to a decrease in elasticity, is probably due to the discrete clustering of focal adhesions. Applying a shear stress on cells leads to a step-wise detachment of such clusters, which results in a fast decrease in cell area.[189] In contrast, the spreading of cells depends on actin polymerization, diffusion of adhesion receptors, and myosin contractility[204], which results in a relatively slow process.

A positive correlation was found for the total strain energy and projected cell area (Figure 5.4c). Since the data points before and after switching of E are shown, a gap between both states is visible for all cells, indicating the immediate response by decreased cell area and strain energy. Previously, a linear correlation between the average traction force and the cell area was shown,[61] suggesting that the cell shape plays a major role in the active force generation.

hMSCs are exposed to a large range of elastic moduli *in vivo*.[46,205] When cultured on fixed elasticity *in vitro*, hMSCs specify to various lineages like adipogenic or osteogenic,[205] but little is known how hMSCs behave in a dynamic environment, similar to the *in vivo* niche. To simulate this behavior, the elasticity of the host-guest gel was switched every $2, 4, 7, 10$ or 20 days, inducing a periodic mechanical stimulus on the cells. After 20 days, the long term effects of this dynamic niche model are investigated. The cell density after 20 days was significantly lower in samples which were exposed to more frequent mechanical stimuli (Figure 5.6b). A similar behavior was observed in a previous study where hMSCs were seeded on pH-sensitive substrates and exposed to a frequent change in elasticity with the same frequency as in this thesis. The proliferation was measured by BrdU activity and decreased with the frequency of mechanical stimulus and agrees well with the cell density in the current study. Previously, Winer *et al.* reported that hMSCs enter a quiescent mode, i.e. stop proliferation, when cultured on very soft substrates ($E = 0.25\,\mathrm{kPa}$), while on stiffer substrates the fraction of proliferating cells was higher ($\approx 50\,\%$ at $E = 7.5\,\mathrm{kPa}$).[206] Yang *et al.* studied the expression of the mechanosensitive marker YAP (yes-associated protein) to a reversible switching of substrate elasticity and found that the nuclear fraction of YAP was irreversibly changed after 7 or more days of incubation on the stiff substrate.[24] This shows that the temporal information of mechanical stimuli is indispensable in order to characterize the cell response.

After 20 days of repeated mechanical stimuli, the hMSCs were fluorescently labeled for STRO-1, a well-known mesenchymal stem cell marker, that has been shown to deplete during lineage specification.[68,107,207] Compared to control ($p \approx$

7 %), the STRO-1 expression increased on the static gel ($f^{-1} = 20\,\mathrm{d},\ p \approx 25\,\%$) and was even enhanced for periodic stimuli ($f^{-1} = 2 - 10\,\mathrm{d},\ p \approx 60 - 85\,\%$, Figure 5.6c), indicating a sustained activity of STRO-1 on stimuli-responsive hydrogels. A previous study reported the sustainability of STRO-1 levels on hydrogel substrates independent of substrate stiffness.[6] Other studies also reported the increased immunofluorescence of STRO-1 on static soft compared to stiff or rigid substrates.[208,209] Therefore, this is the first study to reveal a stimuli- and frequency-dependent STRO-1 expression. Additionally, a clear threshold in elasticity was discovered around $E = 20 - 25\,\mathrm{kPa}$ which triggers the cellular mechanomachinery and significantly increases adhesion strength and active force generation beyond this threshold.

6 Conclusions

Increasing number of studies have demonstrated that physical microenvironments of cells are highly dynamic during the development, aging, and diseases. The aim of this study is to develop quantitative systems for understanding how cells control their functions and fate in response to dynamic changes in the physical microenvironments. Two new stimuli-responsive substrates that reversibly change the surface topography and elasticity were designed, and the dynamic response of cells, driven by contact guidance and mechanosensing, was measured using the combination of unique experimental and analytical tools.

In Chapter 4 a substrate with periodic wrinkles of adjustable wavelength is presented which was designed under collaboration with Dr. T. Ohzono of the National Institute of Advanced Industrial Science and Technology (AIST, Japan) to control the adhesion, morphology, and orientational order of C2C12 mouse myoblasts. The substrate is made from polydimethylsiloxane with a thin coating of polyamic acid which forms periodic wrinkles with fine-adjustable wavelengths ($1.7-6.3\,\mu m$) on the surface. In the first step, the experiments were performed under static conditions, where cells followed the undulation of wrinkles by arranging the focal adhesions, morphology and cytoskeletons (*static contact guidance*). In addition to standard measures for morphology, such as projected cell area and aspect ratio, the directional order of cells was assessed by calculating nematic order parameter by approximating cells as ellipses. Furthermore, the order parameter was calculated for actin cytoskeletons to see how intracellular macromolecules follow the substrate anisotropy. Remarkably, both order parameters strongly suggested the existence of a critical wavelength for the contact guidance $\lambda^* = 3-4\,\mu m$. The localization of focal adhesions by immunofluorescence staining demonstrated focal

adhesions were located only at the peaks of wrinkles at $\lambda < \lambda^*$, indicating that cell membrane in contact with the surface remained flat and span across the troughs. On the other hand, focal adhesions were present at both, the peaks and troughs for $\lambda > \lambda^*$, implying the cell membrane was able to follow the wrinkle undulation. Since this duality shares common features with the transition between partial wetting and complete wetting, the physical mechanism was discussed in terms of balance between tension-induced gain in free energy and the energy penalty of membrane bending. In the second step, these wrinkled substrates were integrated into a custom-designed, motorized pusher to precisely control the applied strain. Upon application of axial strain, the wrinkle orientation is switched by 90° within 60 s, and the dynamic response of cells, such as shape adaptation and change in directional order out of equilibrium, was monitored by live cell imaging. In contrast to the contact guidance under static conditions, such experiments can be considered as dynamic contact guidance. Transfection with LifeAct-GFP allows to monitor dynamic changes in the nematic order parameter of actin $\langle S_{actin} \rangle$ over time which smoothly changed from the parallel to the perpendicular alignment of actin filaments after switching of the wrinkle direction. Intriguingly, the transition of order parameter can be characterized quantitatively by the minimum aspect ratio and the isotropic actin order, $\langle S_{actin} \rangle = 0$, indicating the orchestration of shape change and cytoskeletal remodeling. Notably, the dynamic contact guidance observed here is fully reversible, as confirmed by the observation after the release of strain. The combination of substrates with tunable and switchable wrinkles with quantitative analytical tools unraveled (i) the presence of critical wavelength for partial to full adhesion (wetting) and (ii) the kinetics of dynamic adaptation of cell shape and orientational order of cells and actin cytoskeletons.

Chapter 5 presents the design of a new class of supramolecular hydrogel substrate crosslinked via reversible host-guest interactions. The substrates were prepared by the radical polymerization of acrylamide monomers with host (β-cyclodextrin) and guest (adamantane) moieties, synthesized by the group of Prof. A. Harada of Osaka University (Japan). The crosslinks mediated via host-guest in-

teractions can be canceled by incubating the substrates with the medium containing solubilized host/guest molecules, while the host-guest interactions can be recovered by incubating the blank medium with no host/guest molecules. The substrate elasticity can be adjusted flexibly and reversibly by the concentration and hence the chemical potential of host/guest molecules. Thus, by using non-toxic host or guest molecules, the micromechanical environment of cells can be switched reversibly without interfering with cell viability, which was not possible with commonly used stimulus responsive gels utilizing toxic UV irradiation or irreversible enzymatic degradation. In this thesis, supramolecular hydrogels that can possess the elastic modulus of $8 - 25\,\mathrm{kPa}$ were used to dynamically regulate the morphology, adhesion strength, active traction force, and fate of human mesenchymal stem cells (hMSC) derived from bone marrow under collaboration with the Department of Hematology, University Hospital Heidelberg. In the first step, the morphology and cytoskeleton arrangement of hMSC on soft ($8\,\mathrm{kPa}$) and stiff ($25\,\mathrm{kPa}$) hydrogels were analyzed under static conditions, exhibiting a clear pattern by plotting aspect ratio vs. projected cell area. It is notable that aspect ratio and actin order parameter $\langle S_{actin} \rangle$ represent well the difference between hMSC exposed to two different mechanical environments. Distinctly different morphology and actin ordering should cause a clear difference in adhesion strength. Thus, in the next step, the strength of cell adhesion was quantified by measuring the critical pressure required for cell detachment with a self-developed setup utilizing a laser-induced pressure wave. Remarkably, the critical detachment pressure P^* showed a monotonic increase with increasing substrate elasticity, suggesting the existence of a critical elastic modulus at $E^* \approx 20 - 25\,\mathrm{kPa}$, turning on the mechanosensitive machinery. Moreover, the analysis of traction forces generated by hMSC with the aid of traction force microscopy, the net contractile moment calculated from the displacement of nanoparticle probes showed a distinct increase across $E^* \approx 20 - 25\,\mathrm{kPa}$, too. Extending the results obtained under static conditions, the dynamic response of hMSC to changes in the elastic modulus of substrate was investigated in the next step. The traction force microscopy data collected from

the live cell imaging implied that the total strain energy decreased immediately after the shift of the elastic modulus from 25 to 15 kPa. A clearly positive correlation between total strain energy and projected cell area was observed, suggesting that the area of cell-substrate contact determines the energy dissipated by the deformation of the substrate. Finally, the influence on cell fate was examined by periodically switching the substrate elasticity between 25 and 8 kPa every 2, 4, 7, 10 and 20 days. Intriguingly, the cell density monotonically decreased with increasing frequency of elasticity switching, indicating that frequent mechanical stress suppresses the proliferation of hMSC without interfering with the multipotency. It is notable that the multipotency marker (STRO-1) exhibited a higher level of expression when cells were stressed at higher frequencies, indicating that frequent mechanical stresses enhance the multiple lineage capacity and suppress the self-renewal.

The reversibly tunable, stimuli-responsive substrates established in this study open new possibilities to investigate non-equilibrium cellular responses to external mechanical cues. New insights into the mechanism behind dynamic contact guidance as well as dynamic mechanosensing of the cellular microenvironment obtained here will be helpful not only as well-defined platforms for the investigation on the interplays of biochemical and physical cues, but also as new materials for the optimization of functions and fate of stem and progenitor cells by time-dependent cues.

A Supporting information to Chapter 4

A.1 Dynamic spreading of cell on substrate below critical wavelength

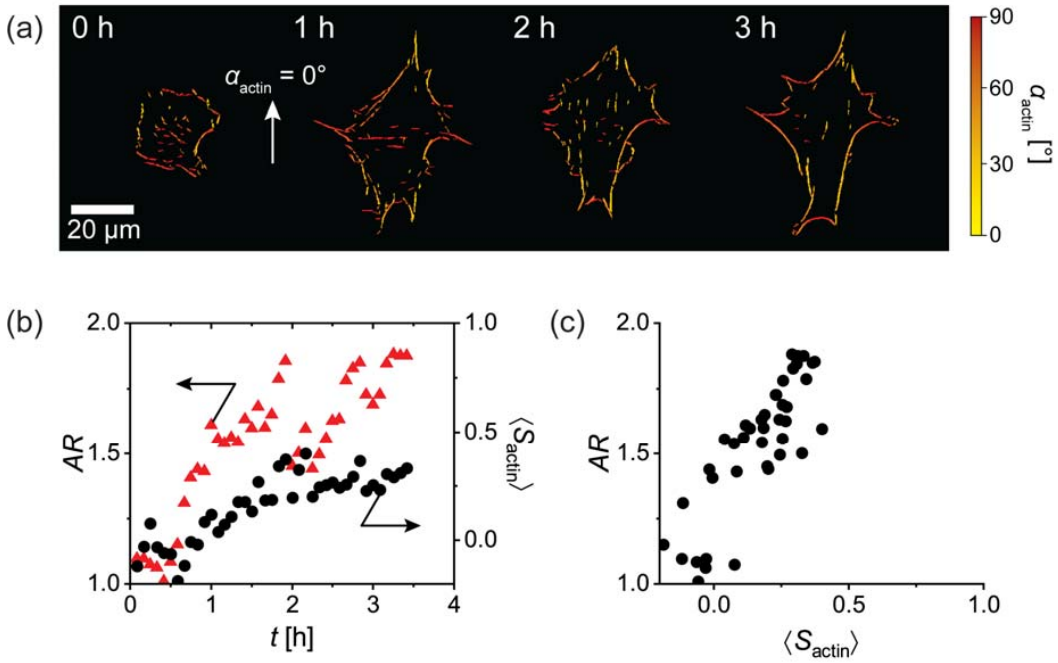

Figure A.1: Dynamic spreading of one example C2C12 cell on wrinkled substrate with $\lambda = 1.7\,\mu m$. (a) Actin filaments were stained by transfection and the detected actin filaments are shown with a color code indicating the orientation with respect to the wrinkle direction (white arrow). (b) The aspect ratio AR and order parameter of actin $\langle S_{actin} \rangle$ are plotted over time. (c) A positive correlation was observed between AR and $\langle S_{actin} \rangle$ during the observed time period.

A.2 Dynamic spreading of cell on flat substrate

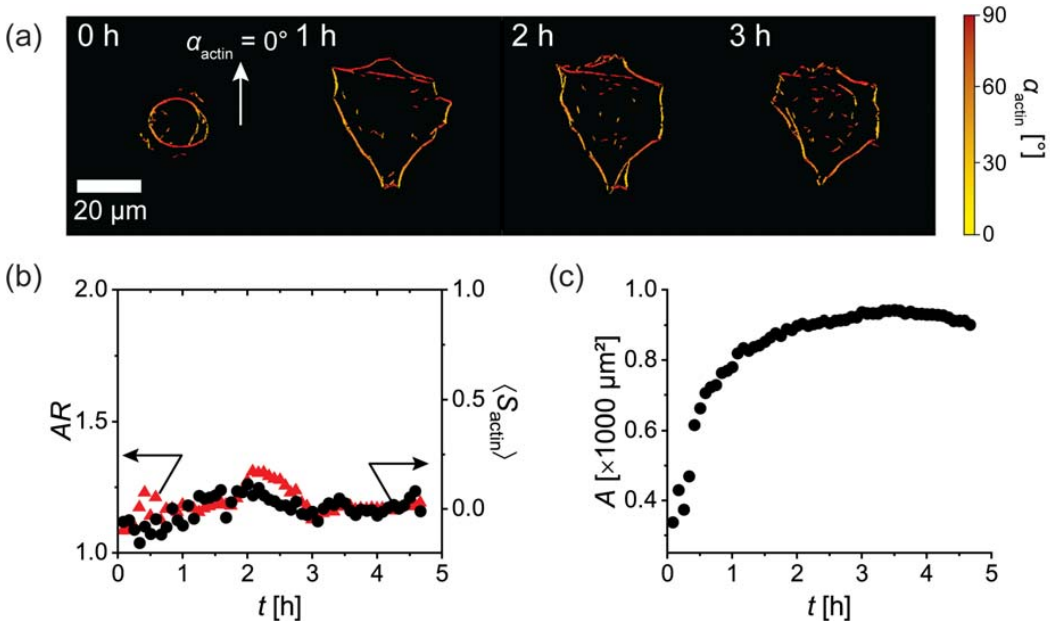

Figure A.2: Dynamic spreading of one example C2C12 cell on a flat substrate. (a) Orientation of detected actin filaments with respect to the vertical axis. The glass substrate was coated with a polyimide layer. (b) The aspect ratio AR and order parameter of actin $\langle S_{actin} \rangle$ are plotted over time. Both parameters remained almost constant during the observed time period ($AR \approx 1$, $\langle S_{actin} \rangle \approx 0$). (c) Change of cell area over time. The cell area increased over time despite the isotropic actin ordering.

A.3 Response of C2C12 cells to a dynamic change in wrinkle orientation with a wavelength of $\lambda = 3.7\,\mu m$

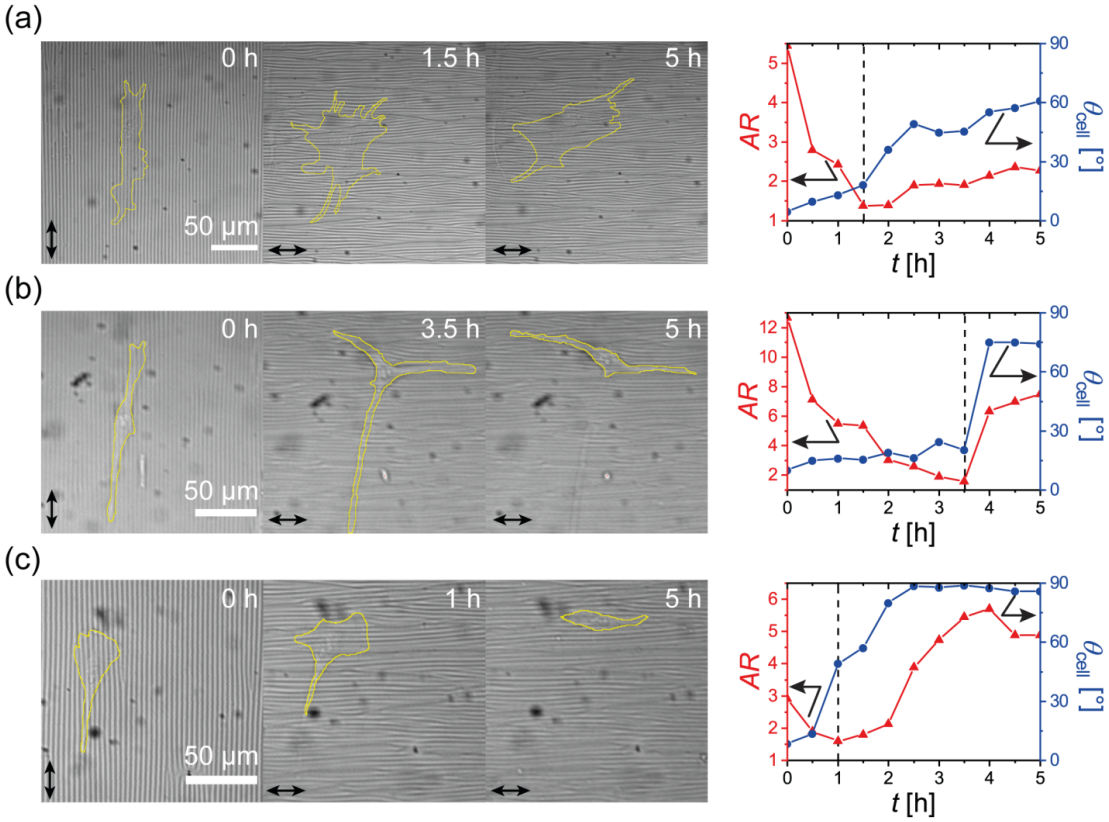

Figure A.3: Response of C2C12 cells to a dynamic topography. The wrinkle wavelength was $\lambda = 3.7\,\mu m$ and the orientation was switched by 90° at $t = 0\,h$ within 60 s. Images on the left are acquired by DIC imaging and for better visibility, the cell edge was marked in yellow. On the right, aspect ratio AR (red triangles) and cell angle θ_{cell} (blue circles) are plotted against time. The dashed line indicates the minimum of AR which is defined as the critical transition time and usually correlates with the increase of the cell angle ($t^*_{AR} \approx t^*_{\theta}$).

A.4 Response of C2C12 cells to a dynamic change in wrinkle orientation with a wavelength of $\lambda = 1.7\,\mu m$

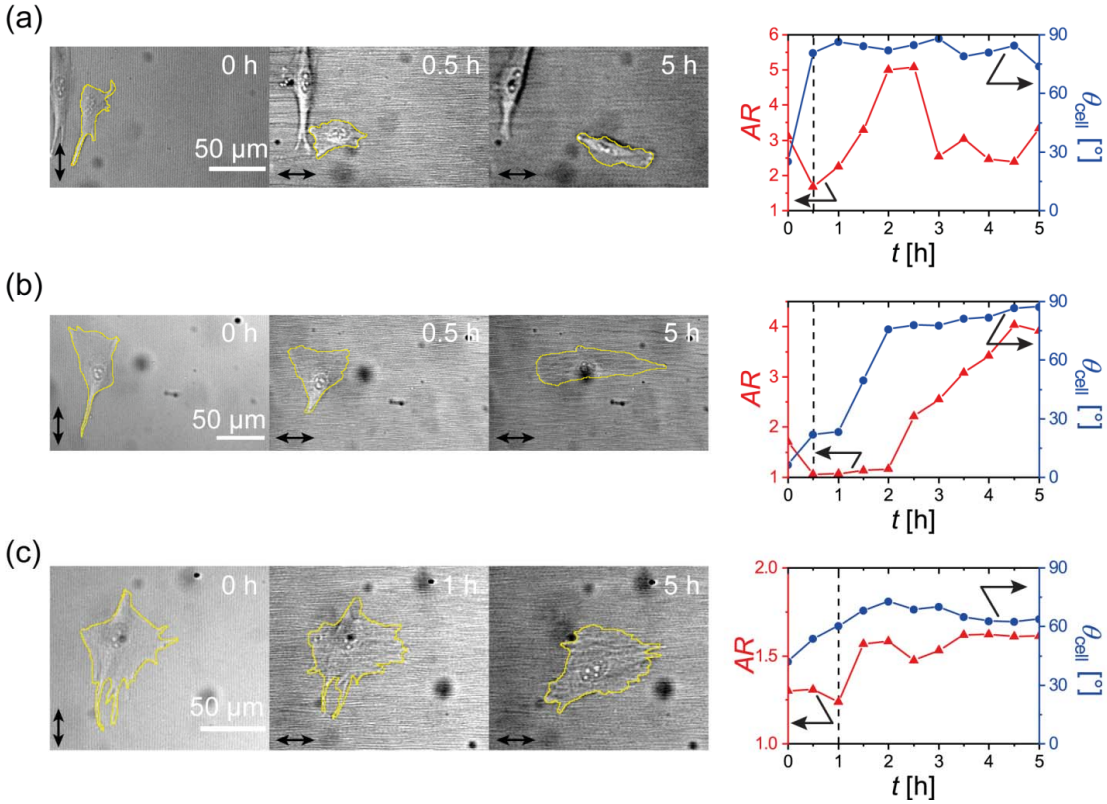

Figure A.4: Response of C2C12 cells to a dynamic topography. The wrinkle wavelength was $\lambda = 1.7\,\mu m$ and the orientation was switched by 90° at $t = 0\,h$ within 60 s. Images on the left are acquired by DIC imaging and for better visibility, the cell edge was marked in yellow. On the right, aspect ratio AR (red triangles) and cell angle θ_{cell} (blue circles) are plotted against time. The dashed line indicates the minimum of AR which is defined as the critical transition time and usually correlates with the increase of the cell angle ($t^*_{AR} \approx t^*_{\theta}$).

A.5 Rough estimation of adhesion free energy

The behavior of cell membranes can be modeled to some extend by treating it as a simple Newtonian fluid.[210] Therefore, it establishes a finite contact angle φ at the three phase contact (solid/liquid/vapor = S/L/V). According to Young's equation, the free energy of adhesion is calculated as follows:

$$F_{\text{adh}} = \gamma_{\text{SV}} + \gamma_{\text{LV}} - \gamma_{\text{SL}} = \gamma_{\text{LV}}(1 + \cos\varphi) \, . \tag{A.1}$$

The three parameters $\gamma_{\text{SV}}, \gamma_{\text{LV}}$ and γ_{SL} represent the tension at the solid-vapor, liquid-vapor and solid-liquid interface respectively. Additionally, the effect of membrane elasticity has to be considered.[74] The length scale within which the membrane deformation is driven by the elasticity is defined as the capillary length:[211]

$$l = \sqrt{\frac{\kappa}{\gamma}} \, . \tag{A.2}$$

The determination of the capillary length requires an accurate measurement of the membrane distance near the contact line which can be achieved by microinterferrometry.[74] However, in the case of wrinkled substrates, this technique is not available, therefore an estimation of the contact angle was made by recontructing the cell shape from vertical slices of a confocal stack (Figure A.5). Microscopy images were obtained from the fluorescence signal of LifeACT-GFP which stains actin in living cells. The vertical slice was taken perpendicular to the wrinkle direction and the contact angle was measured by approximating the cell membrane with a circular arc (curved yellow line). To mitigate the influence of the cell nucleus which heavily influences the cell shape, three vertical slices are taken of each image, indicated by the straight yellow lines. With the average contact angle $\langle\varphi\rangle \approx 23°$ and the membrane tension of cell membranes $\gamma \approx 10^{-6}\,\text{J/m}^2$ [168] the order of magnitude of the adhesion free energy results in $\approx 10^{-6}\,\text{J/m}^2$.

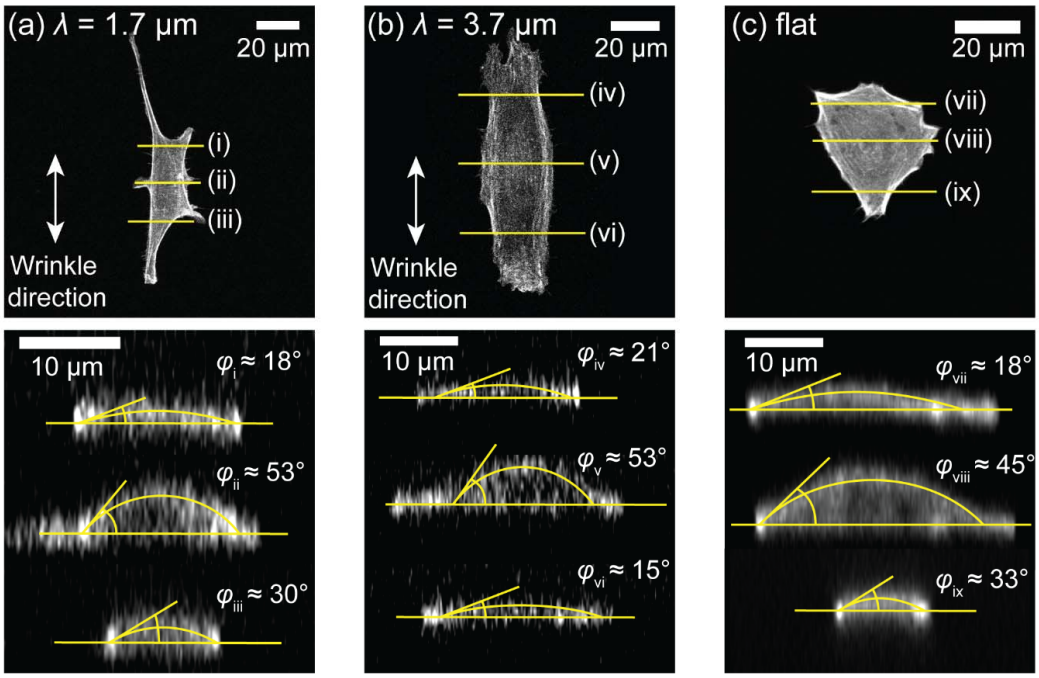

Figure A.5: Top view (maximum projection of slices) and side view (vertical sections) of three C2C12 cells are shown after 4 h on substrates with (a) $\lambda = 1.7\,\mu\text{m}$, (b) $\lambda = 3.7\,\mu\text{m}$, and (c) the flat substrate. The upper images show the top view with the wrinkle direction along the white arrow. Below are the vertical slices where the cell shape is approximated by circular arcs (curved yellow line) and the contact angle φ is measured at the contact point with the substrate. Since the height profiles ii, v and viii were heavily influenced by the nucleus, two additional slices in the cell periphery were analyzed for each cell which resulted in the average contact angle of $\langle\varphi\rangle \approx 23°$

A.6 Free energy of cell membranes on wrinkled substrates

Assuming, the cell membrane perfectly follows the undulation of the wrinkled substrate (full adhesion, Figure 4.3f), then the height profile of the membrane can be written as:

$$h(x,y) = \frac{\Delta h}{2} \sin\left(\frac{2\pi}{\lambda} x\right). \tag{A.3}$$

The bending energy exerted on the area $A = L \cdot 1$ is calculated according to Equation 4.4:

$$F_{\text{bend}} = \frac{1}{L} \int_0^1 dy \int_0^\lambda dx \, \frac{1}{2} \kappa \, C_x^2 \sqrt{g}, \tag{A.4}$$

where $g = 1 + \left(\frac{\delta h}{\delta x}\right)^2$ is the surface metric. The substitution of $C_x = \frac{\frac{\delta^2 h}{\delta x^2}}{g^{3/2}}$ yields:

$$F_{\text{bend}} = \frac{\kappa}{2L} \int_0^\lambda \frac{\left(\frac{\Delta h}{2}\right)^2 \left(\frac{2\pi}{\lambda}\right)^3 \sin^2\left(\frac{2\pi}{\lambda} x\right)}{\left(1 + \left(\frac{\Delta h}{2}\right)^2 \left(\frac{2\pi}{\lambda}\right)^2 \cos^2\left(\frac{2\pi}{\lambda} x\right)\right)^{5/2}} \, dx. \tag{A.5}$$

Since the integrand is periodic with the period $\pi/2$, one can write:

$$F_{\text{bend}} = \frac{2\kappa}{L} \int_0^{\pi/2} \frac{\left(\frac{\Delta h}{2}\right)^2 \left(\frac{2\pi}{\lambda}\right)^3 \sin^2\left(\frac{2\pi}{\lambda} x\right)}{\left(1 + \left(\frac{\Delta h}{2}\right)^2 \left(\frac{2\pi}{\lambda}\right)^2 \cos^2\left(\frac{2\pi}{\lambda} x\right)\right)^{5/2}} \, dx \tag{A.6}$$

$$= \frac{4\pi}{3} \frac{\left(2\pi^2 \left(\frac{\Delta h}{\lambda}\right)^2 + 1\right) \cdot E\left(\frac{\pi^2 \left(\frac{\Delta h}{\lambda}\right)^2}{\pi^2 \left(\frac{\Delta h}{\lambda}\right)^2 + 1}\right) - K\left(\frac{\pi^2 \left(\frac{\Delta h}{\lambda}\right)^2}{\pi^2 \left(\frac{\Delta h}{\lambda}\right)^2 + 1}\right)}{\sqrt{\pi^2 \left(\frac{\Delta h}{\lambda}\right)^2 + 1}} \frac{\kappa}{\lambda L} \tag{A.7}$$

$$= f_1\left(\tfrac{\Delta h}{\lambda}\right) \frac{\kappa}{\lambda L}. \tag{A.8}$$

The two parameters $K(k) = \int_0^{\pi/2} \frac{1}{\sqrt{1 - k^2 \sin^2\theta}} \, d\theta$ and $E(k) = \int_0^{\pi/2} \sqrt{1 - k^2 \sin^2\theta} \, d\theta$ are the complete elliptic integrals of the first kind and the second kind, respectively.

Applying the same strategy, the length L cas be represented as follows:

$$L = \int_0^{\lambda} \sqrt{1 + \left(\frac{\delta h}{\delta x}\right)^2}\, dx \tag{A.9}$$

$$L = \frac{2}{\pi}\sqrt{1 + \pi^2 \left(\frac{\Delta h}{\lambda}\right)^2} E\left(\frac{\pi^2 \left(\frac{\Delta h}{\lambda}\right)^2}{\pi^2 \left(\frac{\Delta h}{\lambda}\right)^2 + 1}\right) \lambda \tag{A.10}$$

$$L = f_2(\tfrac{\Delta h}{\lambda})\lambda. \tag{A.11}$$

Combining these two results, the bending energy per unit area can be written as:

$$F_{\text{bend}} = \frac{f_1(\frac{\Delta h}{\lambda})}{f_2(\frac{\Delta h}{\lambda})} \frac{\kappa}{\lambda^2}. \tag{A.12}$$

From the experiments in this thesis the fraction of height and wavelength resulted in $\frac{\Delta h}{\lambda} \approx 0.13$ so that the two functions in Equation A.6 are represented by constant values: $f_1(0.13) \approx 1.50$ and $f_2(0.13) \approx 1.04$. Thus, the bending energy per unit area scales with $F_{\text{bend}} \propto \frac{\kappa}{\lambda^2}$.

Assuming, the cell membrane remains flat and only adheres to the peaks of wrinkles (partial adhesion, Figure 4.3c), the adhesion area is reduced due to the fraction of cell-substrate contact ($0 < \chi < 1$), as described in the main text. Naturally, the adhesion energy per unit area is smaller in the case of partial adhesion, compared to full adhesion. Geometrically, a perfectly flat area has infinitesimally small contacts at the peaks of wrinkles ($\chi = 0$), therefore the bending energy is neglected in the case of partial adhesion, leading to an underestimation of the total free energy per unit area.

B Supporting information to Chapter 5

B.1 Viability of mesenchymal stem cells

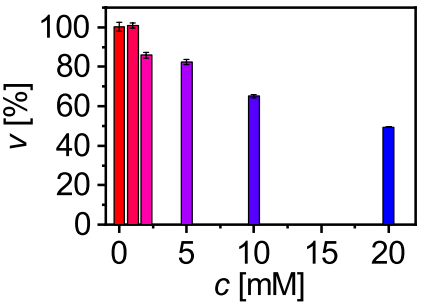

Figure B.1: Viability of mesenchymal stem cells is plotted against concentration of adamantane-carboxylic acid (Ad-COOH). The WST-a assay was used, which evaluates the cell viability based on mitochondrial activity. At concentrations up to 5 mM the viability was sustained at >80 %.

B.2 Size of cavitation bubble

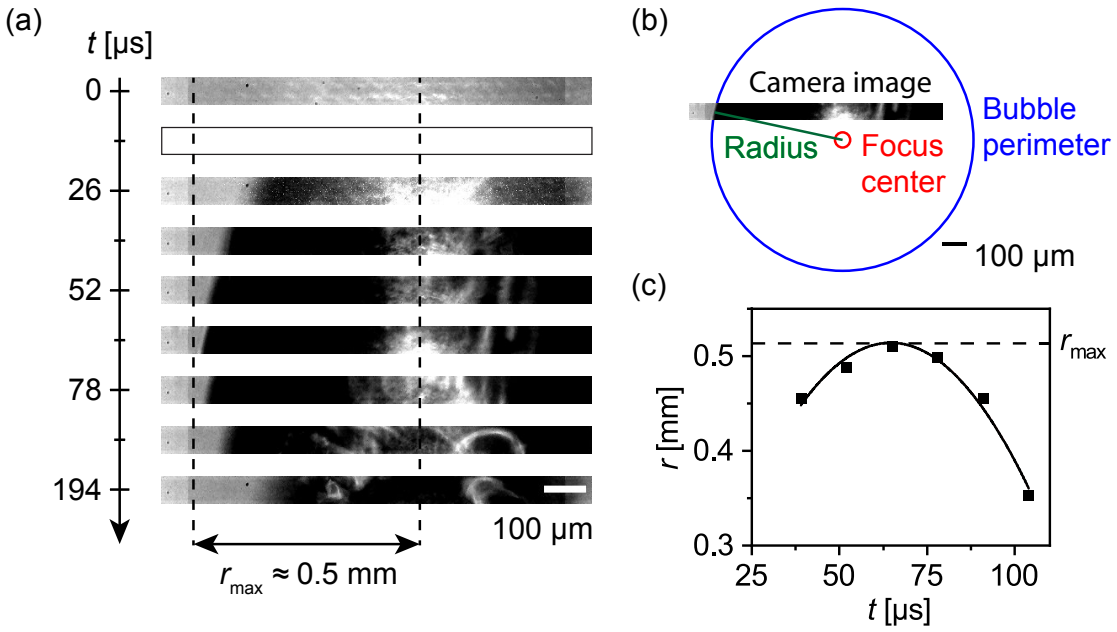

Figure B.2: Cavitation bubble size is estimated by high frame rate video. (a) Brightfield images with rectangular region of interest are shown depending on acquisition time t. The black area is the cavitation bubble with the center at the right dashed line and the maximum radius ($r_{max} \approx 0.5\,\mathrm{mm}$) at the left dashed line. Due to overexposure of the camera during the laser pulse, the second image is white. (b) Scheme of the region of interest in comparison to the full bubble size. The bubble radius is shown in green, the bubble perimeter in blue, and the focus point in red. Larger images would slow down the camera speed (frame rate) and are therefore not possible. (c) The radius of the bubble is plotted against time. A second order polynomial was fitted to the data to determine the maximum radius.

B.3 Net contractile moment depending on adhesion strength

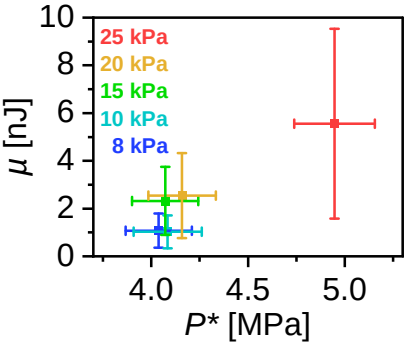

Figure B.3: The net contractile moment μ is plotted against the critical pressure of cell detachment. Each data point was acquired at a different substrate elasticity E which is indicated by the color code. A positive correlation was observed with significantly higher values for both parameters at $E = 25\,\mathrm{kPa}$ compared to softer samples.

B.4 Total strain energy and aspect ratio respond to elasticity change

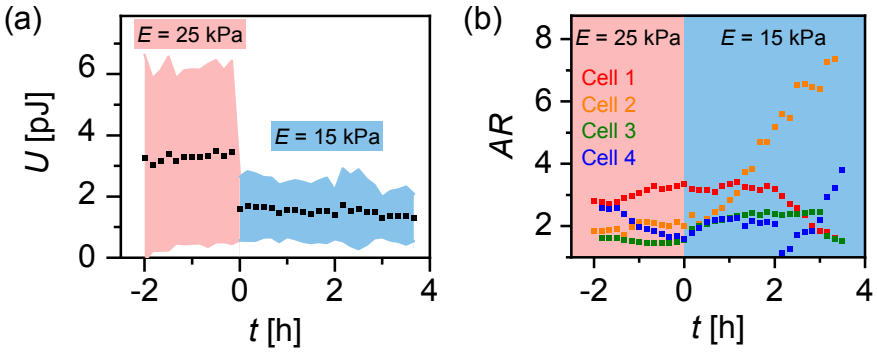

Figure B.4: (a) Total strain energy U is plotted against time. The data of four cells is averaged and plotted as black squares with the standard deviation indicated by the red and blue areas. Substrate elasticity is switched at $t = 0\,\mathrm{h}$ from 25 to 15 kPa. (b) Aspect ratio AR of four cells is plotted over time. Substrate elasticity is switched at $t = 0\,\mathrm{h}$.

C Abbreviations

Ad	Adamantane
AFM	Atomic force microscopy
AIST	National Institute of Advanced Industrial Science and Technology
AML	Acute myeloid leukemia
APS	Ammonium persulfate
AR	Aspect ratio
βCD	Beta-cyclodextrin
BrdU	DescriptionBromodeoxyuridine
BSA	Bovine serum albumin
COI	Cell orientation index
DIC	Differential interference contrast
DNA	Deoxyribonucleic acid
ECM	Extra-cellular matrix
FDA	Food and Drug Administration
FTTC	Fourier transform traction cytometry
FWHM	Full width at half maximum
GFP	Green fluorescent protein
HEPES	4-(2-hydroxyethyl)-1-piperazineethanesulfonic acid
hMSC	human mesenchymal stem cells
KIT	Karlsruhe Institute of Technology
Laser	Light amplification by stimulated emission of radiation
PBS	Phosphate buffered saline
PDMS	Polydimethylsiloxane
PFA	Paraformaldehyde
pH	Power of hydrogen
PIV	Particle image velocimetry
PSF	Point spread function
TEMED	Tetramethylethylenediamine
YAP	Yes-assosiated protein

D Publications

1. M. Tanaka, M. Nakahata, P. Linke, and S. Kaufmann. Stimuli-responsive hydrogels as a model of the dynamic cellular microenvironment. *Polymer Journal* 52(8):861–870, 2020.

2. T. Bentele, F. Amadei, E. Kimmle, M. Veschgini, P. Linke, M. Sonntag-González, J. Tennigkeit, A. D. Ho, S. Özbek, and M. Tanaka. New Class of Crosslinker-Free Nanofiber Biomaterials from Hydra Nematocyst Proteins. *Scientific Reports* 9(1):19116, 2019.

3. P. Linke, R. Suzuki, A. Yamamoto, M. Nakahata, M. Kengaku, T. Fujiwara, T. Ohzono, and M. Tanaka. Dynamic Contact Guidance of Myoblasts by Feature Size and Reversible Switching of Substrate Topography: Orchestration of Cell Shape, Orientation, and Nematic Ordering of Actin Cytoskeletons. *Langmuir* 35(23):7538–7551, 2019.

4. M. Hörning, M. Nakahata, P. Linke, A. Yamamoto, M. Veschgini, S. Kaufmann, Y. Takashima, A. Harada, and M. Tanaka. Dynamic Mechano-Regulation of Myoblast Cells on Supramolecular Hydrogels Cross-Linked by Reversible Host-Guest Interactions. *Scientific Reports* 7(1):7660, 2017.

E Bibliography

[1] E. Sackmann and R. Merkel. *Lehrbuch der Biophysik*. Wiley-VCH Verlag, 2010.

[2] G. Huang, F. Li, X. Zhao, Y. Ma, Y. Li, M. Lin, G. Jin, T. J. Lu, G. M. Genin, and F. Xu. Functional and Biomimetic Materials for Engineering of the Three-Dimensional Cell Microenvironment. *Chemical Reviews*, 117(20):12764–12850, 2017.

[3] H. Tanimoto and M. Sano. A simple force-motion relation for migrating cells revealed by multipole analysis of traction stress. *Biophysical Journal*, 106(1):16–25, 2014.

[4] R. J. Pelham and Y. l. Wang. Cell locomotion and focal adhesions are regulated by the mechanical properties of the substrate. In *Biological Bulletin*, volume 194, pages 348–350. National Acad Sciences, 1998.

[5] K. Matsuzaka, F. Walboomers, A. Ruijter, and J. A. Jansen. Effect of microgrooved poly-l-lactic (PLA) surfaces on proliferation, cytoskeletal organization, and mineralized matrix formation of rat bone marrow cells. *Clinical Oral Implants Research*, 11(4):325–333, 2000.

[6] V. Frank, S. Kaufmann, R. Wright, P. Horn, H. Y. Yoshikawa, P. Wuchter, J. Madsen, A. L. Lewis, S. P. Armes, A. D. Ho, and M. Tanaka. Frequent mechanical stress suppresses proliferation of mesenchymal stem cells from human bone marrow without loss of multipotency. *Scientific Reports*, 6(April):1–12, 2016.

[7] A. S. Burk, C. Monzel, H. Y. Yoshikawa, P. Wuchter, R. Saffrich, V. Eckstein, M. Tanaka, and A. D. Ho. Quantifying Adhesion Mechanisms and Dynamics of Human Hematopoietic Stem and Progenitor Cells. *Scientific Reports*, 5:1–11, 2015.

[8] E. T. Den Braber, J. E. De Ruijter, L. A. Ginsel, A. F. Von Recum, and J. A. Jansen. Orientation of ECM protein deposition, fibroblast cytoskeleton, and attachment complex components on silicone microgrooved surfaces. *Journal of Biomedical Materials Research*, 40(2):291–300, 1998.

[9] M. Hörning, M. Nakahata, P. Linke, A. Yamamoto, M. Veschgini, S. Kaufmann, Y. Takashima, A. Harada, and M. Tanaka. Dynamic Mechano-Regulation of Myoblast Cells on Supramolecular Hydrogels Cross-Linked by Reversible Host-Guest Interactions. *Scientific Reports*, 7(1):7660, 2017.

[10] J. S. Park, J. S. Chu, A. D. Tsou, R. Diop, Z. Tang, A. Wang, and S. Li. The effect of matrix stiffness on the differentiation of mesenchymal stem cells in response to TGF-β. *Biomaterials*, 32(16):3921–3930, 2011.

[11] F. Re, A. Zanetti, M. Sironi, N. Polentarutti, L. Lanfrancone, E. Dejana, and F. Colotta. Inhibition of anchorage-dependent cell spreading triggers apoptosis in cultured human endothelial cells. *Journal of Cell Biology*, 127(2):537–546, 1994.

[12] C. S. Chen, M. Mrksich, S. Huang, G. M. Whitesides, and D. E. Ingber. Geometric control of cell life and death. *Science*, 276(5317):1425–1428, 1997.

[13] D. E. Ingber. Tensegrity: The architectural basis of cellular mechanotransduction, 1997.

[14] D. E. Discher, P. Janmey, and Y. L. Wang. Tissue cells feel and respond to the

stiffness of their substrate. *Science*, 310(5751):1139–1143, 2005.
[15] D. Riveline, E. Zamir, N. Q. Balaban, U. S. Schwarz, T. Ishizaki, S. Narumiya, Z. Kam, B. Geiger, and A. D. Bershadsky. Focal contacts as mechanosensors: Externally applied local mechanical force induces growth of focal contacts by an mDia1-dependent and ROCK-independent mechanism. *Journal of Cell Biology*, 153(6):1175–1185, 2001.
[16] C. B. Zanetti, M. B. Lopes, A. M. Lyrio, P. R. de Campos, R. Bonfiglioli, and M. A. B. Teixeira. Case 3 - Congestive heart failure in male with systemic sclerosis. *Arquivos Brasileiros de Cardiologia*, 101(1), 2013.
[17] P. Weiss. Experiments on cell and axon orientation in vitro: The role of colloidal exudates in tissue organization. *Journal of Experimental Zoology*, 100(3):353–386, 1945.
[18] P. S. Swain and D. Andelman. Influence of substrate structure on membrane adhesion. *Langmuir*, 15(26):8902–8914, 1999.
[19] S. C. Cowin. Structural change in living tissues. *Meccanica*, 34(5):379–398, 1999.
[20] T. G. Van Kooten and A. F. Von Recum. Cell adhesion to textured silicone surfaces: The influence of time of adhesion and texture on focal contact and fibronectin fibril formation. *Tissue Engineering*, 5(3):223–240, 1999.
[21] C. Rianna, L. Rossano, R. H. Kollarigowda, F. Formiggini, S. Cavalli, M. Ventre, and P. A. Netti. Spatio-Temporal Control of Dynamic Topographic Patterns on Azopolymers for Cell Culture Applications. *Advanced Functional Materials*, 26 (42):7572–7580, 2016.
[22] J. D. Kiang, J. H. Wen, J. C. Del Álamo, and A. J. Engler. Dynamic and reversible surface topography influences cell morphology. *Journal of Biomedical Materials Research - Part A*, 101 A(8):2313–2321, 2013.
[23] Y. Zhao, H. Zeng, J. Nam, and S. Agarwal. Fabrication of skeletal muscle constructs by topographic activation of cell alignment. *Biotechnology and Bioengineering*, 102(2):624–631, 2009.
[24] C. Yang, M. W. Tibbitt, L. Basta, K. S. Anseth, B. Engineering, and C. Avenue. Mechanical memory and dosing influence stem cell fate. *Nature materials*, 13(6): 645–652, 2014.
[25] M. Tsuchiya, Y. Hara, M. Okuda, K. Itoh, R. Nishioka, A. Shiomi, K. Nagao, M. Mori, Y. Mori, J. Ikenouchi, R. Suzuki, M. Tanaka, T. Ohwada, J. Aoki, M. Kanagawa, T. Toda, Y. Nagata, R. Matsuda, Y. Takayama, M. Tominaga, and M. Umeda. Cell surface flip-flop of phosphatidylserine is critical for PIEZO1-mediated myotube formation. *Nature Communications*, 9(1), 2018.
[26] E. Sackmann and R. F. Bruinsma. Cell adhesion as wetting transition?, 2002.
[27] C. W. Harland, M. J. Bradley, and R. Parthasarathy. Phospholipid bilayers are viscoelastic. *Proceedings of the National Academy of Sciences of the United States of America*, 107(45):19146–19150, 2010.
[28] A. I. Teixeira, G. A. Abrams, P. J. Bertics, C. J. Murphy, and P. F. Nealey. Epithelial contact guidance on well-defined micro- and nanostructured substrates. *Journal of Cell Science*, 116(10):1881–1892, 2003.
[29] N. Bowden, S. Brittain, A. G. Evans, J. W. Hutchinson, and G. M. Whitesides. Spontaneous formation of ordered structures in thin films of metals supported on an elastomeric polymer. *Nature*, 393(6681):146–149, 1998.
[30] T. Ohzono and M. Shimomura. Ordering of microwrinkle patterns by compressive

strain. *Physical Review B - Condensed Matter and Materials Physics*, 69(13): 132202, 2004.

[31] T. Ohzono, H. Monobe, K. Shiokawa, M. Fujiwara, and Y. Shimizu. Shaping liquid on a micrometre scale using microwrinkles as deformable open channel capillaries. *Soft Matter*, 5(23):4658–4664, 2009.

[32] Z. Wang, D. Tonderys, S. E. Leggett, E. K. Williams, M. T. Kiani, R. Spitz Steinberg, Y. Qiu, I. Y. Wong, and R. H. Hurt. Wrinkled, wavelength-tunable graphene-based surface topographies for directing cell alignment and morphology. *Carbon*, 97:14–24, 2016.

[33] D. Cheng, R. K. Jayne, A. Tamborini, J. Eyckmans, A. E. White, and C. S. Chen. Studies of 3D directed cell migration enabled by direct laser writing of curved wave topography, 2019.

[34] C. Tamiello, A. B. Buskermolen, F. P. Baaijens, J. L. Broers, and C. V. Bouten. Heading in the Right Direction: Understanding Cellular Orientation Responses to Complex Biophysical Environments, 2016.

[35] X. Zhao, L. Jin, H. Shi, W. Tong, D. Gorin, Y. Kotelevtsev, and Z. Mao. Recent advances of designing dynamic surfaces to regulate cell adhesion, 2020.

[36] S. Sun, H. Shi, S. Moore, C. Wang, A. Ash-Shakoor, P. T. Mather, J. H. Henderson, and Z. Ma. Progressive Myofibril Reorganization of Human Cardiomyocytes on a Dynamic Nanotopographic Substrate. *ACS Applied Materials and Interfaces*, 12 (19):21450–21462, 2020.

[37] P. Yang, R. M. Baker, J. H. Henderson, and P. T. Mather. In vitro wrinkle formation via shape memory dynamically aligns adherent cells. *Soft Matter*, 9(18): 4705–4714, 2013.

[38] M. T. Lam, W. C. Clem, and S. Takayama. Reversible on-demand cell alignment using reconfigurable microtopography. *Biomaterials*, 29(11):1705–1712, 2008.

[39] T. Ohzono and M. Shimomura. Geometry-dependent stripe rearrangement processes induced by strain on preordered microwrinkle patterns. *Langmuir*, 21(16): 7230–7237, 2005.

[40] H. Y. Yoshikawa, T. Kawano, T. Matsuda, S. Kidoaki, and M. Tanaka. Morphology and adhesion strength of myoblast cells on photocurable gelatin under native and non-native micromechanical environments. *Journal of Physical Chemistry B*, 117 (15):4081–4088, 2013.

[41] A. Zemel, F. Rehfeldt, A. E. Brown, D. E. Discher, and S. A. Safran. Optimal matrix rigidity for stress-fibre polarization in stem cells. *Nature Physics*, 6(6): 468–473, 2010.

[42] S. Inoue, V. Frank, M. Hörning, S. Kaufmann, H. Y. Yoshikawa, J. P. Madsen, A. L. Lewis, S. P. Armes, and M. Tanaka. Live cell tracking of symmetry break in actin cytoskeleton triggered by abrupt changes in micromechanical environments. *Biomaterials Science*, 3(12):1539–1544, 2015.

[43] A. K. Harris, P. Wild, and D. Stopak. Silicone rubber substrata: A new wrinkle in the study of cell locomotion. *Science*, 208(4440):177–179, 1980.

[44] N. Q. Balaban, U. S. Schwarz, D. Riveline, P. Goichberg, G. Tzur, I. Sabanay, D. Mahalu, S. Safran, A. Bershadsky, L. Addadi, and B. Geiger. Force and focal adhesion assembly: a close relationship studied using elastic micropatterned substrates. *Nature cell biology*, 3(5):466–472, 2001.

[45] K. E. Kasza and J. A. Zallen. Dynamics and regulation of contractile actin-myosin

networks in morphogenesis, 2011.
[46] J. S. Choi, B. P. Mahadik, and B. A. C. Harley. Engineering the hematopoietic stem cell niche: Frontiers in biomaterial science. *Biotechnology Journal*, 10(10): 1529–1545, 2015.
[47] A. J. Engler, M. A. Griffin, S. Sen, C. G. Bönnemann, H. L. Sweeney, and D. E. Discher. Myotubes differentiate optimally on substrates with tissue-like stiffness: Pathological implications for soft or stiff microenvironments. *Journal of Cell Biology*, 166(6):877–887, 2004.
[48] T. Yeung, P. C. Georges, L. A. Flanagan, B. Marg, M. Ortiz, M. Funaki, N. Zahir, W. Ming, V. Weaver, and P. A. Janmey. Effects of substrate stiffness on cell morphology, cytoskeletal structure, and adhesion. *Cell Motility and the Cytoskeleton*, 60(1):24–34, 2005.
[49] H. Y. Yoshikawa, F. F. Rossetti, S. Kaufmann, T. Kaindl, J. Madsen, U. Engel, A. L. Lewis, S. P. Armes, and M. Tanaka. Quantitative evaluation of mechanosensing of cells on dynamically tunable hydrogels. *Journal of the American Chemical Society*, 133(5):1367–1374, 2011.
[50] Y. Luo, K. R. Kirker, and G. D. Prestwich. Cross-linked hyaluronic acid hydrogel films: New biomaterials for drug delivery. *Journal of Controlled Release*, 69(1): 169–184, 2000.
[51] T. G. van Kooten, J. F. Whitesides, and A. F. von Recum. Influence of silicone (PDMS) surface texture on human skin fibroblast proliferation as determined by cell cycle analysis. *Journal of Biomedical Materials Research*, 43(1):1–14, 1998.
[52] P. Toselli, P. J. Mogayzel, and B. Faris. Mammalian cell growth on collagen-hydrogels, 1984.
[53] H. M. Kvasnicka, C. Beham-Schmid, R. Bob, S. Dirnhofer, K. Hussein, H. Kreipe, M. Kremer, A. Schmitt-Graeff, S. Schwarz, J. Thiele, M. Werner, and H. Stein. Problems and pitfalls in grading of bone marrow fibrosis, collagen deposition and osteosclerosis - a consensus-based study. *Histopathology*, 68(6):905–915, 2016.
[54] R. G. Wells. Tissue mechanics and fibrosis, 2013.
[55] J. S. Choi and B. A. Harley. Marrow-inspired matrix cues rapidly affect early fate decisions of hematopoietic stem and progenitor cells. *Science Advances*, 3(1), 2017.
[56] S. Méndez-Ferrer, T. V. Michurina, F. Ferraro, A. R. Mazloom, B. D. MacArthur, S. A. Lira, D. T. Scadden, A. Ma'ayan, G. N. Enikolopov, and P. S. Frenette. Mesenchymal and haematopoietic stem cells form a unique bone marrow niche. *Nature*, 466(7308):829–834, 2010.
[57] T. A. Wynn. Fibrotic disease and the TH1/TH2 paradigm, 2004.
[58] A. A. Zahr, M. E. Salama, N. Carreau, D. Tremblay, S. Verstovsek, R. Mesa, R. Hoffman, and J. Mascarenhas. Bone marrow fibrosis in myelofibrosis: Pathogenesis, prognosis and targeted strategies, 2016.
[59] W. Wagner, C. Roderburg, F. Wein, A. Diehlmann, M. Frankhauser, R. Schubert, V. Eckstein, and A. D. Ho. Molecular and Secretory Profiles of Human Mesenchymal Stromal Cells and Their Abilities to Maintain Primitive Hematopoietic Progenitors. *Stem Cells*, 25(10):2638–2647, 2007.
[60] W. Wagner, F. Wein, C. Roderburg, R. Saffrich, A. Faber, U. Krause, M. Schubert, V. Benes, V. Eckstein, H. Maul, and A. D. Ho. Adhesion of hematopoietic progenitor cells to human mesenchymal stem cells as a model for cell-cell interaction. *Experimental Hematology*, 35(2):314–325, 2007.

[61] M. Guvendiren and J. A. Burdick. Stiffening hydrogels to probe short- and long-term cellular responses to dynamic mechanics. *Nature Communications*, 3(1):1–9, 2012.

[62] S. Khetan, M. Guvendiren, W. R. Legant, D. M. Cohen, C. S. Chen, and J. A. Burdick. Degradation-mediated cellular traction directs stem cell fate in covalently crosslinked three-dimensional hydrogels. *Nature Materials*, 12(5):458–465, 2013.

[63] A. M. Kloxin, J. A. Benton, and K. S. Anseth. In situ elasticity modulation with dynamic substrates to direct cell phenotype. *Biomaterials*, 31(1):1–8, 2010.

[64] A. M. Rosales, S. L. Vega, F. W. DelRio, J. A. Burdick, and K. S. Anseth. Hydrogels with Reversible Mechanics to Probe Dynamic Cell Microenvironments. *Angewandte Chemie - International Edition*, 56(40):12132–12136, 2017.

[65] E. A. Corbin, A. Vite, E. G. Peyster, M. Bhoopalam, J. Brandimarto, X. Wang, A. I. Bennett, A. T. Clark, X. Cheng, K. T. Turner, K. Musunuru, and K. B. Margulies. Tunable and Reversible Substrate Stiffness Reveals a Dynamic Mechanosensitivity of Cardiomyocytes. *ACS Applied Materials and Interfaces*, 11(23):20603–20614, 2019.

[66] L. Fu, A. Haage, N. Kong, G. Tanentzapf, and H. Li. Dynamic protein hydrogels with reversibly tunable stiffness regulate human lung fibroblast spreading reversibly. *Chemical Communications*, 55(36):5235–5238, 2019.

[67] M. L. Previtera, K. L. Trout, D. Verma, U. Chippada, R. S. Schloss, and N. A. Langrana. Fibroblast morphology on dynamic softening of hydrogels. *Annals of Biomedical Engineering*, 40(5):1061–1072, 2012.

[68] P. J. Simmons and B. Torok-Storb. Identification of stromal cell precursors in human bone marrow by a novel monoclonal antibody, STRO-1. *Blood*, 78(1):55–62, 1991.

[69] J. E. Dennis, J. P. Carbillet, A. I. Caplan, and P. Charbord. The STRO-1+ marrow cell population is multipotential. *Cells Tissues Organs*, 170(2-3):73–82, 2001.

[70] R. Langer and J. P. Vacanti. Tissue engineering. *Science*, 260(5110):920–926, 1993.

[71] J. Lu, A. D. Doyle, Y. Shinsato, S. Wang, M. A. Bodendorfer, M. Zheng, and K. M. Yamada. Basement Membrane Regulates Fibronectin Organization Using Sliding Focal Adhesions Driven by a Contractile Winch. *Developmental Cell*, 52 (5):631–646.e4, 2020.

[72] M. Hoffmann and U. S. Schwarz. A kinetic model for RNA-interference of focal adhesions. *BMC Systems Biology*, 7(1):2, 2013.

[73] R. Bruinsma, A. Behrisch, and E. Sackmann. Adhesive switching of membranes: Experiment and theory. *Physical Review E - Statistical Physics, Plasmas, Fluids, and Related Interdisciplinary Topics*, 61(4):4253–4267, 2000.

[74] A. Albersdorfer, T. Feder, and E. Sackmann. Adhesion-induced Domain Formation by Interplay of Long-Range Repulsion and Short-Range Attraction Force: A Model Membrane Study. Technical report, 1997.

[75] G. I. Bell. Models for the specific adhesion of cells to cells, 1978.

[76] J. O. Rädler, T. J. Feder, H. H. Strey, and E. Sackmann. Fluctuation analysis of tension-controlled undulation forces between giant vesicles and solid substrates. *Physical Review E*, 51(5):4526–4536, 1995.

[77] W. Helfrich. Steric Interaction of Fluid Membranes in Multilayer Systems. *Zeitschrift fur Naturforschung - Section A Journal of Physical Sciences*, 33(3): 305–315, 1978.

[78] T. R. Weikl, D. Andelman, S. Komura, and R. Lipowsky. Adhesion of membranes with competing specific and generic interactions. *European Physical Journal E*, 8 (1):59–66, 2002.

[79] B. Alberts, A. Johnson, J. Lewis, M. Raff, K. Roberts, and P. Walter. *Molecular Biology of the Cell*, volume 43. Garland Science, 5 edition, 2008.

[80] T. L. Hill and J. Gillis. *An Introduction to Statistical Thermodynamics*, volume 14. Dover Publications, 1961.

[81] C. Monzel and K. Sengupta. Measuring shape fluctuations in biological membranes. *Journal of Physics D: Applied Physics*, 49(24), 2016.

[82] R. Phillips, J. Kondev, J. Theriot, and H. Garcia. *Physical Biology of the Cell*. CRC Press, 2012.

[83] C. A. Rutkowski, L. M. Williams, T. H. Haines, and H. Z. Cummins. The Elasticity of Synthetic Phospholipid Vesicles Obtained by Photon Correlation Spectroscopy. *Biochemistry*, 30(23):5688–5696, 1991.

[84] W. Helfrich. Elastic Properties of Lipid Bilayers: Theory and Possible Experiments. Technical report, 1973.

[85] P. B. Canham. The minimum energy of bending as a possible explanation of the biconcave shape of the human red blood cell. *Journal of Theoretical Biology*, 26 (1), 1970.

[86] E. Evans. Bending Resistance and Chemically Induced Moments in Membrane Bilayers. *Biophysical Journal*, 14(12):923–931, 1974.

[87] W. Rawicz, K. C. Olbrich, T. McIntosh, D. Needham, and E. A. Evans. Effect of chain length and unsaturation on elasticity of lipid bilayers. *Biophysical Journal*, 79(1):328–339, 2000.

[88] B. Pontes, Y. Ayala, A. Fonseca, L. F. Romão, and R. F. Amaral. Membrane Elastic Properties and Cell Function. *PLOS One*, 8(7):67708, 2013.

[89] E. A. Evans, R. Waugh, and L. Melnik. Elastic area compressibility modulus of red cell membrane. *Biophysical Journal*, 16(6):585–595, 1976.

[90] Q. Waheed and O. Edholm. Undulation contributions to the area compressibility in lipid bilayer simulations. *Biophysical Journal*, 97(10):2754–2760, 2009.

[91] A. I. Caplan. Mesenchymal stem cells. *Journal of Orthopaedic Research*, 9(5): 641–650, 1991.

[92] H. S. Yang, N. Ieronimakis, J. H. Tsui, H. N. Kim, K. Y. Suh, M. Reyes, and D. H. Kim. Nanopatterned muscle cell patches for enhanced myogenesis and dystrophin expression in a mouse model of muscular dystrophy. *Biomaterials*, 35(5):1478–1486, 2014.

[93] D. Yaffe and O. Saxel. Serial passaging and differentiation of myogenic cells isolated from dystrophic mouse muscle. *Nature*, 270(5639):725–727, 1977.

[94] D. K. McMahon, P. A. Anderson, R. Nassar, J. B. Bunting, Z. Saba, A. E. Oakeley, and N. N. Malouf. C2C12 cells: Biophysical, biochemical, and immunocytochemical properties. *American Journal of Physiology - Cell Physiology*, 266(6 35-6), 1994.

[95] Martini, Nath, and Bartholomew. *Fundamentals of Anatomy & Physiology*. Pearson, 10 edition, 2015.

[96] S. M. Abmayr and G. K. Pavlath. Myoblast fusion: Lessons from flies and mice, 2012.

[97] J. B. Miller, M. T. Crow, and F. E. Stockdale. Slow and fast myosin heavy chain

content defines three types of myotubes in early muscle cell cultures. *Journal of Cell Biology*, 101(5):1643–1650, 1985.

[98] R. Duan and P. J. Gallagher. Dependence of myoblast fusion on a cortical actin wall and nonmuscle myosin IIA. *Developmental Biology*, 325(2):374–385, 2009.

[99] M. M, F. A, and T. Y. Mesenchymal Stem Cells as Muscle Reservoir. *Journal of Stem Cell Research & Therapy*, 01(02), 2011.

[100] R. Gaetani, E. A. Zizzi, M. A. Deriu, U. Morbiducci, M. Pesce, and E. Messina. When Stiffness Matters: Mechanosensing in Heart Development and Disease. *Frontiers in Cell and Developmental Biology*, 8:334, 2020.

[101] J. J. H. Chong, X. Yang, C. W. Don, E. Minami, Y.-W. Liu, J. J. Weyers, W. M. Mahoney, B. Van Biber, S. M. Cook, N. J. Palpant, J. A. Gantz, J. A. Fugate, V. Muskheli, G. M. Gough, K. W. Vogel, C. A. Astley, C. E. Hotchkiss, A. Baldessari, L. Pabon, H. Reinecke, E. A. Gill, V. Nelson, H.-P. Kiem, M. A. Laflamme, and C. E. Murry. Human embryonic-stem-cell-derived cardiomyocytes regenerate non-human primate hearts. *Nature*, 510(7504):273–277, 2014.

[102] A. Uccelli, L. Moretta, and V. Pistoia. Mesenchymal stem cells in health and disease, 2008.

[103] A. J. Friedenstein, R. K. Chailakhyan, and U. V. Gerasimov. Bone marrow osteogenic stem cells: in vitro cultivation and transplantation in diffusion chambers. *Cell Proliferation*, 20(3):263–272, 1987.

[104] R. Hass, C. Kasper, S. Böhm, and R. Jacobs. Different populations and sources of human mesenchymal stem cells (MSC): A comparison of adult and neonatal tissue-derived MSC, 2011.

[105] R. M. Samsonraj, M. Raghunath, V. Nurcombe, J. H. Hui, A. J. van Wijnen, and S. M. Cool. Concise Review: Multifaceted Characterization of Human Mesenchymal Stem Cells for Use in Regenerative Medicine, 2017.

[106] M. Mendicino, A. M. Bailey, K. Wonnacott, R. K. Puri, and S. R. Bauer. MSC-based product characterization for clinical trials: An FDA perspective, 2014.

[107] S. Ranga Rao and R. Subbarayan. Passage-dependent expression of STRO-1 in human gingival mesenchymal stem cells. *Journal of Cellular Biochemistry*, 120(3): 2810–2815, 2019.

[108] M. Nakahata, Y. Takashima, H. Yamaguchi, and A. Harada. Redox-responsive self-healing materials formed from host-guest polymers. *Nature Communications*, 2(1):511, 2011.

[109] W. K. Vonach and F. G. Rammerstorfer. A general approach to the wrinkling instability of sandwich plates. *Structural Engineering and Mechanics*, 12(4):363–376, 2001.

[110] Y. Mei, S. Kiravittaya, S. Harazim, and O. G. Schmidt. Principles and applications of micro and nanoscale wrinkles. In *Materials Science and Engineering R: Reports*, volume 70, pages 209–224. Elsevier, 2010.

[111] Z. Y. Huang, W. Hong, and Z. Suo. Nonlinear analyses of wrinkles in a film bonded to a compliant substrate. *Journal of the Mechanics and Physics of Solids*, 53(9): 2101–2118, 2005.

[112] D. Chatterji. *Basics of molecular recognition*. CRC Press, 2016.

[113] B. X. Colasson, C. Dietrich-Buchecker, M. C. Jimenez-Molero, and J. P. Sauvage. Towards molecular machines and motors based on transition metal complexes. *Journal of Physical Organic Chemistry*, 15(8):476–483, 2002.

[114] M. Nakahata, Y. Takashima, and A. Harada. Highly Flexible, Tough, and Self-Healing Supramolecular Polymeric Materials Using Host-Guest Interaction. *Macromolecular Rapid Communications*, 37(1):86–92, 2016.

[115] H. Schenderlein, A. Voss, R. W. Stark, and M. Biesalski. Preparation and characterization of light-switchable polymer networks attached to solid substrates. *Langmuir*, 29(14):4525–4534, 2013.

[116] T. K. Tam, M. Ornatska, M. Pita, S. Minko, and E. Katz. Polymer brush-modified electrode with switchable and tunable redox activity for bioelectronic applications. *Journal of Physical Chemistry C*, 112(22):8438–8445, 2008.

[117] F. Zhou, W. Shu, M. E. Welland, and W. T. Huck. Highly reversible and multistage cantilever actuation driven by polyelectrolyte brushes. *Journal of the American Chemical Society*, 128(16):5326–5327, 2006.

[118] N. Morimoto, X. P. Qiu, F. M. Winnik, and K. Akiyoshi. Dual stimuli-responsive nanogels by self-assembly of polysaccharides lightly grafted with thiol-terminated poly(N-isopropylacrylamide) chains. *Macromolecules*, 41(16):5985–5987, 2008.

[119] F. Zhou, P. M. Biesheuvel, E. Y. Choi, W. Shu, R. Poetes, U. Steiner, and W. T. Huck. Polyelectrolyte brush amplified electroactuation of microcantilevers. *Nano Letters*, 8(2):725–730, 2008.

[120] F. Hua, T. Cui, and Y. M. Lvov. Ultrathin cantilevers based on polymer-ceramic nanocomposite assembled through layer-by-layer adsorption. *Nano Letters*, 4(5): 823–825, 2004.

[121] A. Harada, Y. Takashima, and M. Nakahata. Supramolecular polymeric materials via cyclodextrin-guest interactions. *Accounts of Chemical Research*, 47(7):2128–2140, 2014.

[122] H. Hertz. Ueber die Berührung fester elastischer Körper. *Journal fur die Reine und Angewandte Mathematik*, 1882(92):156–171, 1882.

[123] K. L. Johnson. *Contact Mechanics*. Cambridge University Press, 1989.

[124] D. C. Lin, E. K. Dimitriadis, and F. Horkay. Robust strategies for automated AFM force curve analysis - I. Non-adhesive indentation of soft, inhomogeneous materials. *Journal of Biomechanical Engineering*, 129(3):430–440, 2007.

[125] G. Cox and C. J. Sheppard. Practical Limits of Resolution in Confocal and Non-Linear Microscopy. *Microscopy Research and Technique*, 63(1):18–22, 2004.

[126] Y. Kim, E. J. Lee, S. Roy, A. S. Sharbirin, L. G. Ranz, T. Dieing, and J. Kim. Measurement of lateral and axial resolution of confocal Raman microscope using dispersed carbon nanotubes and suspended graphene. *Current Applied Physics*, 20 (1):71–77, 2020.

[127] D. S. Biggs. A Practical Guide to Deconvolution of Fluorescence Microscope Imagery. *Microscopy Today*, 18(1):10–14, 2010.

[128] E. Sekko, G. Thomas, and A. Boukrouche. A deconvolution technique using optimal Wiener filtering and regularization. *Signal Processing*, 72(1):23–32, 1999.

[129] G. M. Van Kempen, L. J. Van Vliet, P. J. Verveer, and H. T. Van Der Voort. A quantitative comparison of image restoration methods for confocal microscopy. *Journal of Microscopy*, 185(3):354–365, 1997.

[130] W. H. Richardson. Bayesian-Based Iterative Method of Image Restoration*. Technical Report 1, 1972.

[131] L. B. Lucy. An iterative technique for the rectification of observed distributions. *The Astronomical Journal*, 79:745, 1974.

[132] C. Zimmer, Z. Kam, N. Dey, L. Blanc-Féraud, C. Zimmer, Z. Kam, J.-c. C. Olivo-Marin, and J. Zerubia. A deconvolution method for confocal microscopy with total variation regularization. *2004 2nd IEEE International Symposium on Biomedical Imaging: Nano to Macro*, 2:1223–1226, 2004.

[133] S. Geman and D. Geman. Stochastic Relaxation, Gibbs Distributions, and the Bayesian Restoration of Images. *IEEE Transactions on Pattern Analysis and Machine Intelligence*, PAMI-6(6):721–741, 1984.

[134] S. E. Chesla, P. Selvaraj, and C. Zhu. Measuring two-dimensional receptor-ligand binding kinetics by micropipette. *Biophysical Journal*, 75(3):1553–1572, 1998.

[135] A. A. Khalili and M. R. Ahmad. A Review of cell adhesion studies for biomedical and biological applications. *International Journal of Molecular Sciences*, 16(8): 18149–18184, 2015.

[136] E. Evans, K. Ritchie, and R. Merkel. Sensitive Force Technique to Probe Molecular Adhesion and Structural Linkages at Biological Interfaces. Technical report, 1995.

[137] G. Sagvolden, I. Giaever, E. O. Pettersen, and J. Feder. Cell adhesion force microscopy. *Proceedings of the National Academy of Sciences of the United States of America*, 96(2):471–476, 1999.

[138] M. Benoit, D. Gabriel, G. Gerisch, and H. E. Gaub. Discrete interactions in cell adhesion measured by single-molecule force spectroscopy. *Nature Cell Biology*, 2 (6):313–317, 2000.

[139] J. Friedrichs, K. R. Legate, R. Schubert, M. Bharadwaj, C. Werner, D. J. Müller, and M. Benoit. A practical guide to quantify cell adhesion using single-cell force spectroscopy. *Methods*, 60(2):169–178, 2013.

[140] E. Martines, K. McGhee, C. Wilkinson, and A. Curtis. A Parallel-plate flow chamber to study initial cell adhesion on a nanofeatured surface. *IEEE Transactions on Nanobioscience*, 3(2):90–95, 2004.

[141] T. G. van Kooten, J. M. Schakenraad, H. C. van der Mei, and H. J. Busscher. Influence of substratum wettability on the strength of adhesion of human fibroblasts. *Biomaterials*, 13(13):897–904, 1992.

[142] A. Vogel, S. Busch, and U. Parlitz. Shock wave emission and cavitation bubble generation by picosecond and nanosecond optical breakdown in water. *The Journal of the Acoustical Society of America*, 100(1):148–165, 1996.

[143] E. A. Brujan, K. Nahen, P. Schmidt, and A. Vogel. Dynamics of laser-induced cavitation bubbles near an elastic boundary. *Journal of Fluid Mechanics*, 433: 251–281, 2001.

[144] M. H. Rice and J. M. Walsh. Equation of state of water to 250 kilobars. *The Journal of Chemical Physics*, 26(4):824–830, 1957.

[145] W. Lauterborn. Kavitation Durch Laserlicht. *Acustica*, 31(2):51–78, 1974.

[146] L. Rayleigh. VIII. On the pressure developed in a liquid during the collapse of a spherical cavity. *The London, Edinburgh, and Dublin Philosophical Magazine and Journal of Science*, 34(200):94–98, 1917.

[147] S. Munevar, Y.-l. Wang, and M. Dembo. Traction Force Microscopy of Migrating Normal and H-ras Transformed 3T3 Fibroblasts. *Biophysical Journal*, 80(4):1744–1757, 2001.

[148] B. Sabass, M. L. Gardel, C. M. Waterman, and U. S. Schwarz. High resolution traction force microscopy based on experimental and computational advances. *Biophysical Journal*, 94(1):207–220, 2008.

[149] L. D. Landau and J. M. Lifshitz. *Theory of Elasticity*. Pergamon Press, 1970.
[150] J. P. Butler, I. M. Tolić-Nørrelykke, B. Fabry, and J. J. Fredberg. Traction fields, moments, and strain energy that cells exert on their surroundings. *American Journal of Physiology-Cell Physiology*, 282(3):C595–C605, 2002.
[151] N. Schierbaum, J. Rheinlaender, and T. E. Schäffer. Combined atomic force microscopy (AFM) and traction force microscopy (TFM) reveals a correlation between viscoelastic material properties and contractile prestress of living cells. *Soft Matter*, 15(8):1721–1729, 2019.
[152] S. S. An, J. Kim, K. Ahn, X. Trepat, K. J. Drake, S. Kumar, G. Ling, C. Purington, T. Rangasamy, T. W. Kensler, W. Mitzner, J. J. Fredberg, and S. Biswal. Cell stiffness, contractile stress and the role of extracellular matrix. *Biochemical and Biophysical Research Communications*, 382(4):697–703, 2009.
[153] J. E. Avron, O. Gat, and O. Kenneth. Optimal swimming at low reynolds numbers. *Physical Review Letters*, 93(18), 2004.
[154] T. Qiu, T. C. Lee, A. G. Mark, K. I. Morozov, R. Münster, O. Mierka, S. Turek, A. M. Leshansky, and P. Fischer. Swimming by reciprocal motion at low Reynolds number. *Nature Communications*, 5(1):1–8, 2014.
[155] J. Schindelin, I. Arganda-Carreras, E. Frise, V. Kaynig, M. Longair, T. Pietzsch, S. Preibisch, C. Rueden, S. Saalfeld, B. Schmid, J.-Y. Tinevez, D. J. White, V. Hartenstein, K. Eliceiri, P. Tomancak, and A. Cardona. Fiji: an open-source platform for biological-image analysis. *Nature Methods*, 9(7):676–682, 2012.
[156] F. Cramer, W. Saenger, H.-C. Spatz, and . R. Gelb. Cyclodextrin-Adamantanecarboxylate Inclusion Complexes: Studies of the Variation in Cavity Size CDs are torrus shaped molecules with an apolar cavity and show a certain degree of selectivity in binding ligand hosts. Thus they are a very good model for stu. *The Journal of Physical Chemistry*, 89(3):47, 1985.
[157] W. Kern. The Evolution of Silicon Wafer Cleaning Technology. *Journal of the Electrochemical Society*, 137(6):1887–1892, 1990.
[158] J. R. Tse and A. J. Engler. Preparation of Hydrogel Substrates with Tunable Mechanical Properties. *Current Protocols in Cell Biology*, 47(1):10.16.1–10.16.16, 2010.
[159] Y. Aratyn-Schaus, P. W. Oakes, J. Stricker, S. P. Winter, and M. L. Gardel. Preparation of complaint matrices for quantifying cellular contraction. *Journal of Visualized Experiments*, (46):1–6, 2010.
[160] W. Wagner, R. E. Feldmann, A. Seckinger, M. H. Maurer, F. Wein, J. Blake, U. Krause, A. Kalenka, H. F. Bürgers, R. Saffrich, P. Wuchter, W. Kuschinsky, and A. D. Ho. The heterogeneity of human mesenchymal stem cell preparations—Evidence from simultaneous analysis of proteomes and transcriptomes. *Experimental Hematology*, 34(4):536–548, 2006.
[161] H. Tanimoto and M. Sano. Dynamics of traction stress field during cell division. *Physical Review Letters*, 109(24):1–5, 2012.
[162] X. Jiang, S. Takayama, X. Qian, E. Ostuni, H. Wu, N. Bowden, P. LeDuc, D. E. Ingber, and G. M. Whitesides. Controlling mammalian cell spreading and cytoskeletal arrangement with conveniently fabricated continuous wavy features on poly(dimethylsiloxane). *Langmuir*, 18(8):3273–3280, 2002.
[163] R. L. Steward, C. M. Cheng, D. L. Wang, and P. R. LeDuc. Probing cell structure responses through a shear and stretching mechanical stimulation technique. *Cell*

Biochemistry and Biophysics, 56(2):115–124, 2010.

[164] A. Ray, O. Lee, Z. Win, R. M. Edwards, P. W. Alford, D.-H. Kim, and P. P. Provenzano. Anisotropic forces from spatially constrained focal adhesions mediate contact guidance directed cell migration. *Nature Communications*, 8:14923, 2017.

[165] J. Meyle, K. Gültig, M. Brich, H. Hämmerle, and W. Nisch. Contact guidance of fibroblasts on biomaterial surfaces. *Journal of Materials Science: Materials in Medicine*, 5(6-7):463–466, 1994.

[166] S. T. Wong, S. K. Teo, S. Park, K. H. Chiam, and E. K. Yim. Anisotropic rigidity sensing on grating topography directs human mesenchymal stem cell elongation. *Biomechanics and Modeling in Mechanobiology*, 13(1):27–39, 2014.

[167] U. Seifert. Configurations of fluid membranes and vesicles. *Advances in Physics*, 46(1):13–137, 1997.

[168] R. Simson, E. Wallraft, J. Faix, J. Niewohner, G. Gerisch, and E. Sackmann. Membrane bending modulus and adhesion energy of wild-type and mutant cells of Dictyostelium lacking talin or cortexillins. *Biophysical Journal*, 74(1):514–522, 1998.

[169] O. Purrucker, S. Gönnenwein, A. Förtig, R. Jordan, M. Rusp, M. Bärmann, L. Moroder, E. Sackmann, and M. Tanaka. Polymer-tethered membranes as quantitative models for the study of integrin-mediated cell adhesion. *Soft Matter*, 3(3):333–336, 2007.

[170] H. Ito, N. Kuss, B. E. Rapp, M. Ichikawa, T. Gutsmann, K. Brandenburg, J. M. Pöschl, and M. Tanaka. Quantification of the influence of endotoxins on the mechanics of adult and neonatal red blood cells. *Journal of Physical Chemistry B*, 119(25):7837–7845, 2015.

[171] D. Andelman, J. F. Joanny, and M. O. Robbins. Complete wetting on rough surfaces: Statics. Technical Report 8, 1988.

[172] Q. S. Li, G. Y. Lee, C. N. Ong, and C. T. Lim. AFM indentation study of breast cancer cells. *Biochemical and Biophysical Research Communications*, 374(4):609–613, 2008.

[173] D. H. Kim, E. A. Lipke, P. Kim, R. Cheong, S. Thompson, M. Delannoy, K. Y. Suh, L. Tung, and A. Levchenko. Nanoscale cues regulate the structure and function of macroscopic cardiac tissue constructs. *Proceedings of the National Academy of Sciences of the United States of America*, 107(2):565–570, 2010.

[174] A. B. Mathur, A. M. Collinsworth, W. M. Reichert, W. E. Kraus, and G. A. Truskey. Endothelial, cardiac muscle and skeletal muscle exhibit different viscous and elastic properties as determined by atomic force microscopy. *Journal of Biomechanics*, 34(12):1545–1553, 2001.

[175] A. M. Collinsworth, S. Zhang, W. E. Kraus, and G. A. Truskey. Apparent elastic modulus and hysteresis of skeletal muscle cells throughout differentiation. *American Journal of Physiology - Cell Physiology*, 283(4 52-4):1219–1227, 2002.

[176] D. H. Kim, Kshitiz, R. R. Smith, P. Kim, E. H. Ahn, H. N. Kim, E. Marbán, K. Y. Suh, and A. Levchenko. Nanopatterned cardiac cell patches promote stem cell niche formation and myocardial regeneration. *Integrative Biology (United Kingdom)*, 4 (9):1019–1033, 2012.

[177] B. Wójciak-Stothard, A. S. Curtis, M. McGrath, I. Sommer, C. D. Wilkinson, and W. Monaghan. Role of the cytoskeleton in the reaction of fibroblasts to multiple grooved substrata. *Cell Motility and the Cytoskeleton*, 31(2):147–158, 1995.

[178] C. Oakley and D. M. Brunette. The sequence of alignment of microtubules, focal contacts and actin filaments in fibroblasts spreading on smooth and grooved titanium substrata. Technical Report 1, 1993.

[179] A. J. Engler, S. Sen, H. L. Sweeney, and D. E. Discher. Matrix Elasticity Directs Stem Cell Lineage Specification. *Cell*, 126(4):677–689, 2006.

[180] S. Huang, C. S. Chen, and D. E. Ingber. Control of cyclin D1, p27(Kip1), and cell cycle progression in human capillary endothelial cells by cell shape and cytoskeletal tension. *Molecular Biology of the Cell*, 9(11):3179–3193, 1998.

[181] U. S. Schwarz and J. R. Soiné. Traction force microscopy on soft elastic substrates: A guide to recent computational advances, 2015.

[182] H. Rieger, H. Y. Yoshikawa, K. Quadt, M. A. Nielsen, C. P. Sanchez, A. Salanti, M. Tanaka, and M. Lanzer. Cytoadhesion of Plasmodium falciparum - Infected erythrocytes to chondroitin-4-sulfate is cooperative and shear enhanced. *Blood*, 125(2):383–391, 2015.

[183] T. M. Koch, S. Münster, N. Bonakdar, J. P. Butler, and B. Fabry. 3D traction forces in cancer cell invasion. *PLOS One*, 7(3), 2012.

[184] M. G. Honig and R. I. Hume. Fluorescent carbocyanine dyes allow living neurons of identified origin to be studied in long-term cultures. Technical Report 1, 1986.

[185] L. MacQueen, Y. Sun, and C. A. Simmons. Mesenchymal stem cell mechanobiology and emerging experimental platforms. *Journal of the Royal Society Interface*, 10 (84), 2013.

[186] B. Trappmann, J. E. Gautrot, J. T. Connelly, D. G. Strange, Y. Li, M. L. Oyen, M. A. Cohen Stuart, H. Boehm, B. Li, V. Vogel, J. P. Spatz, F. M. Watt, and W. T. Huck. Extracellular-matrix tethering regulates stem-cell fate. *Nature Materials*, 11(7):642–649, 2012.

[187] R. Xue, J. Y.-S. Li, Y. Yeh, L. Yang, and S. Chien. Effects of matrix elasticity and cell density on human mesenchymal stem cells differentiation. *Journal of Orthopaedic Research*, 31(9):1360–1365, 2013.

[188] B. L. Doss, M. Pan, M. Gupta, G. Grenci, R. M. Mège, C. T. Lim, M. P. Sheetz, R. Voituriez, and B. Ladoux. Cell response to substrate rigidity is regulated by active and passive cytoskeletal stress. *Proceedings of the National Academy of Sciences of the United States of America*, 117(23):12817–12825, 2020.

[189] C. Selhuber-Unkel, T. Erdmann, M. López-García, H. Kessler, U. S. Schwarz, and J. P. Spatz. Cell adhesion strength is controlled by intermolecular spacing of adhesion receptors. *Biophysical Journal*, 98(4):543–551, 2010.

[190] M. Castelain, F. Pignon, J. M. Piau, and A. Magnin. The initial single yeast cell adhesion on glass via optical trapping and Derjaguin-Landau-Verwey-Overbeek predictions. *Journal of Chemical Physics*, 128(13):135101, 2008.

[191] J. Vogel, G. Bendas, U. Bakowsky, G. Hummel, R. R. Schmidt, U. Kettmann, and U. Rothe. The role of glycolipids in mediating cell adhesion: A flow chamber study. *Biochimica et Biophysica Acta - Biomembranes*, 1372(2):205–215, 1998.

[192] G. A. Truskey and J. S. Pirone. The effect of fluid shear stress upon cell adhesion to fibronectin-treated surfaces. *Journal of Biomedical Materials Research*, 24(10): 1333–1353, 1990.

[193] C. D. Ohl and B. Wolfrum. Detachment and sonoporation of adherent HeLa-cells by shock wave-induced cavitation. *Biochimica et Biophysica Acta - General Subjects*, 1624(1-3):131–138, 2003.

[194] M. Schmidt, U. Kahlert, J. Wessolleck, D. Maciaczyk, B. Merkt, J. Maciaczyk, J. Osterholz, G. Nikkhah, and M. O. Steinhauser. Characterization of a setup to test the impact of high-amplitude pressure waves on living cells. *Scientific Reports*, 4, 2014.

[195] H. Y. Yoshikawa, J. Cui, K. Kratz, T. Matsuzaki, S. Nakabayashi, A. Marx, U. Engel, A. Lendlein, and M. Tanaka. Quantitative evaluation of adhesion of osteosarcoma cells to hydrophobic polymer substrate with tunable elasticity. *Journal of Physical Chemistry B*, 116(28):8024–8030, 2012.

[196] K. Ghosh, Z. Pan, E. Guan, S. Ge, Y. Liu, T. Nakamura, X. D. Ren, M. Rafailovich, and R. A. Clark. Cell adaptation to a physiologically relevant ECM mimic with different viscoelastic properties. *Biomaterials*, 28(4):671–679, 2007.

[197] K. Mandal, D. Raz-Ben Aroush, Z. T. Graber, B. Wu, C. Y. Park, J. J. Fredberg, W. Guo, T. Baumgart, and P. A. Janmey. Soft Hyaluronic Gels Promote Cell Spreading, Stress Fibers, Focal Adhesion, and Membrane Tension by Phosphoinositide Signaling, Not Traction Force. *ACS Nano*, 13(1):203–214, 2019.

[198] J. P. Califano and C. A. Reinhart-King. Substrate stiffness and cell area predict cellular traction stresses in single cells and cells in contact. *Cellular and Molecular Bioengineering*, 3(1):68–75, 2010.

[199] F. Chowdhury, Y. Li, Y.-C. Poh, T. Yokohama-Tamaki, N. Wang, and T. S. Tanaka. Soft Substrates Promote Homogeneous Self-Renewal of Embryonic Stem Cells via Downregulating Cell-Matrix Tractions. *PLOS One*, 5(12):e15655, 2010.

[200] J. Wu, K. Wu, F. Lin, Q. Luo, L. Yang, Y. Shi, G. Song, and K. L. P. Sung. Mechano-growth factor induces migration of rat mesenchymal stem cells by altering its mechanical properties and activating ERK pathway. *Biochemical and Biophysical Research Communications*, 441(1):202–207, 2013.

[201] A. D. Rape, W. H. Guo, and Y. L. Wang. The regulation of traction force in relation to cell shape and focal adhesions. *Biomaterials*, 32(8):2043–2051, 2011.

[202] J. Voog and D. L. Jones. Stem Cells and the Niche: A Dynamic Duo, 2010.

[203] A. Batsivari, M. L. R. Haltalli, D. Passaro, C. Pospori, C. Lo Celso, and D. Bonnet. Dynamic responses of the haematopoietic stem cell niche to diverse stresses, 2020.

[204] D. Cuvelier, M. Théry, Y. S. Chu, S. Dufour, J. P. Thiéry, M. Bornens, P. Nassoy, and L. Mahadevan. The Universal Dynamics of Cell Spreading. *Current Biology*, 17(8):694–699, 2007.

[205] I. L. Ivanovska, J. W. Shin, J. Swift, and D. E. Discher. Stem cell mechanobiology: Diverse lessons from bone marrow, 2015.

[206] J. P. Winer, S. Oake, and P. A. Janmey. Non-Linear Elasticity of Extracellular Matrices Enables Contractile Cells to Communicate Local Position and Orientation. *PLOS One*, 4(7):e6382, 2009.

[207] P. J. Psaltis, S. Paton, F. See, A. Arthur, S. Martin, S. Itescu, S. G. Worthley, S. Gronthos, and A. C. Zannettino. Enrichment for STRO-1 expression enhances the cardiovascular paracrine activity of human bone marrow-derived mesenchymal cell populations. *Journal of Cellular Physiology*, 223(2):530–540, 2010.

[208] J. Lee, A. A. Abdeen, A. S. Kim, and K. A. Kilian. Influence of Biophysical Parameters on Maintaining the Mesenchymal Stem Cell Phenotype. *ACS Biomaterials Science and Engineering*, 1(4):218–226, 2015.

[209] Y. Ji, J. Li, Y. Wei, W. Gao, X. Fu, and Y. Wang. Substrate stiffness affects the immunosuppressive and trophic function of hMSCs: Via modulating cytoskeletal

polymerization and tension. *Biomaterials Science*, 7(12):5292–5300, 2019.

[210] M. Gupta, B. R. Sarangi, J. Deschamps, Y. Nematbakhsh, A. Callan-Jones, F. Margadant, R. M. Mège, C. T. Lim, R. Voituriez, and B. Ladoux. Adaptive rheology and ordering of cell cytoskeleton govern matrix rigidity sensing. *Nature Communications*, 6(1):1–9, 2015.

[211] R. Bruinsma. Adhesion and rolling of leukocytes: A physical model. *Proceedings of the NATO Advanced Study Institute on Physics and Biomaterials. NATO ASI Series*, 332, 1995.